ELUCIDATING NUCLEATION AND GROWTH BEHAVIOR OF SINGLE-WALLED CARBON NANOTUBES OBTAINED VIA CATALYZED SYNTHESIS

A Dissertation

by

JUAN CARLOS BURGOS BELTRAN

Submitted to the Office of Graduate and Professional Studies of
Texas A&M University
in partial fulfillment of the requirements for the degree of

DOCTOR OF PHILOSOPHY

Chair of Committee,	Perla B. Balbuena
Committee Members,	Raymundo Arroyave
	Tahir Cagin
	Yue Kuo
Head of Department,	Ibrahim Karaman

December 2014

Major Subject: Materials Science and Engineering

ABSTRACT

The catalytic growth of single-walled carbon nanotubes (SWCNTs) is studied using reactive molecular dynamics (RMD) simulations and density functional theory (DFT) calculations. Computational calculations are performed in order to achieve a better understanding of the catalytic reaction mechanism at the initial stages of synthesis, where most of the structural characteristics are defined. Different process variables such as catalyst chemical composition and size, temperature, pressure, and the nature of catalyst support, can be optimized with the purpose of tuning the structure and physical properties of SWCNTs. Controlling the structure of SWCNTs during synthesis and avoiding additional purification and/or separation processes are critical for the direct use of SWCNTs in electronic devices.

RMD simulations demonstrate that small catalyst particles favor the growth of lengthy nanotubes over catalyst encapsulation as a result of an increase of the curvature energies of the carbon capsule. Furthermore, simulations performed over deposited catalyst particles demonstrate that the catalyst-support adhesion must be controlled in order to grow nanotubes with high structural quality and avoid catalyst poisoning. Results herein reported suggest that growth conditions must be optimum to minimize the nucleation of topological defects in nanotubes. RMD trajectories prove the vital role played by the catalyst surface in healing defects via adsorption and diffusion. These results significantly impact the field of chirality control since the presence of defects introduce misorientation of hexagons, shifts the overall chiral angle, and therefore, modifies the physical properties of the nanotube.

DFT calculations are employed to evaluate the interaction between SWCNTs and the ST-cut quartz substrate. The outstanding performance of CNT-based FET relies on the alignment of the horizontally grown nanotubes on silica substrates, as well as on the selective growth of semiconducting nanotubes. It is demonstrated that finite-length zigzag nanotubes are adsorbed stronger than armchair tubes on the quartz support. This suggests that the nanotube electronic band structure is a key factor on the preferential adsorption of zigzag tubes. DFT calculations suggest that patterns of unsaturated silicon atoms of silica surfaces define the crystallographic directions of preferential alignment. These patterns might be chemically altered in order to favor other directions of alignment.

DEDICATION

To my father, mother, and sisters, for their constant and unconditional support

ACKNOWLEDGEMENTS

I would like to thank my supervisor and committee chair, Dr. Perla Balbuena, for her support and guidance throughout the course of this research. I would also like to thank my committee members, Dr. Raymundo Arroyave, Dr. Tahir Cagin, and Dr.Yue Kuo, for their advices and recommendations during the completion of this work.

I want to extend my gratitude to the US Department of Energy, Basic Energy Sciences, grant DE- FG02-06ER15836, for providing financial support for my graduate studies at Texas A&M University. Furthermore, I want to thank to computational resources from TAMU Supercomputer Facility, Brazos Cluster at Texas A&M University, Texas Advanced Computing Center (TACC), and the National Energy Research Scientific Computing Center, which is supported by the Office of Science of the U.S. Department of Energy under Contract No. DE-AC03-76SF00098.

Finally, especial thanks to my coworkers at Dr. Balbuena's group at Texas A&M University, for their collaboration, useful opinions, and feedbacks provided along the realization of this project, and to my family for their encouragement and support.

NOMENCLATURE

SWCNT	Single-walled carbon nanotube
MD	Molecular dynamics
RMD	Reactive molecular dynamics
AIMD	Ab initio molecular dynamics
BOMD	Born-Oppenheimer molecular dynamics
DFT	Density functional theory
CVD	Chemical vapor deposition

TABLE OF CONTENTS

Page

LIST OF FIGURES

FIGURE Page

FIGURE Page

1. INTRODUCTION

The discovery of carbon nanotubes in 1991 by IIjima[1] unleashed innumerous research works aiming to characterize their structure, properties, and structure/property relationships [2-4]. As a consequence of these efforts, carbon nanotubes were found to have excellent mechanical, electronic, and optical properties that lead this novel material to meet performance standards required for various technological applications[5-7]. However, the controlled synthesis of carbon nanotubes, and single-walled carbon nanotubes (SWCNTs) specifically, is still a challenge. Electronic, optical, and magnetic properties of this nanomaterial are intrinsically related to their structural features, and despite the evolution and innovation achieved in growth methods, synthesis of bundles of 100% pure SWCNTs free of defects and with a specific structure is still an impossible task. As a result of the incapability to control the structure of nascent nanotubes during the growth process, different approaches have arisen to purify and fractionate as-grown SWCNTs from other carbon materials and SWCNTs with undesirable structures[8]. However, application of techniques such as electrophoresis, density gradient centrifugation, or size exclusion chromatography, can become complicated and expensive making the high volume manufacture of carbon nanotubes nonviable. Thus, the potential utilization of SWCNTs in technological applications, such as electronic devices, will depend on the ability to control structural variables of SWCNTs during growth, principally diameter, length and chirality.

Among the different techniques employed to produce SWCNTs, we can distinguish arc discharge[9], laser ablation[10], and chemical vapor deposition (CVD)[11] as the three most common methods. In this study, we will focus on the analyses of the catalytic CVD process variables with the goal of controlling the structure of the nanotubes during growth, which would intrinsically tailor their physical properties. Temperature, nature and concentration of the precursor species, catalyst particles nature, size, and composition, chemical composition of the catalyst support and its surface topology, type of inert species and their partial pressures, are some of the variables that can be tuned during a CVD growth to control SWCNTs structure. Extraordinary results have been achieved regarding chirality and electronic type selectivity form different researchers using specific combinations of the variables aforementioned[12-14]. However, the wide range of catalyst systems and adjustable reaction conditions, along with the lack of detailed information about the reaction mechanisms, reveal the high level of complexity in controlling the structure of SWCNTs during growth.

Thus, this theoretical study has two main objectives. First, to determine the conditions at which exclusive growth of SWCNTs may be prevalent over any other kind of carbon material. Second, to identify the role of various process variables on the diameter and chiral/electronic selectivity. Therefore, the response of catalytic systems will be evaluated from the atomistic point of view through density functional theory (DFT) and classical and ab initio molecular dynamics simulations. In the first part of this study, the preferential formation of carbon nanotubes is studied dynamically as a function of the catalyst morphology: size and shape. This topic will be studied in detail in the sections 4 and 5, and will be complemented by the analysis of defects formation during SWCNTs growth in the section 6. In the second part, DFT calculations are used to elucidate the influence of the catalyst support on growth and selectivity. The effect of the topology of clean and functionalized silica surfaces on alignment and selectivity will be discussed on sections 7 and 8.

2. BACKGROUND

Single-walled carbon nanotubes are allotropes of carbon that are frequently classified within the family of the fullerenes. Unlike the buckyball,[15] SWCNTs are characterized by having a cylindrical structure with diameters typically in the range of 0.5-3 nm. Nanotubes can be described as a single graphene rolled to form a symmetrical cylindrical structure. Despite the fact that the synthesis processes that produce SWCNTs are more complicated than rolling graphene, this assumption is very useful to understand the different helical types that nanotubes may have. Thus, the term chirality is introduced to describe the helicity of SWCNTs and is defined by the orientation of the hexagonal graphitic lattice respect to the principal axis of the enfolded graphene.

Hence, single walled carbon nanotubes can be classified according to their helicity within two main groups, achiral and chiral nanotubes. Achiral nanotubes present perfect symmetry respect to the tube axis, which is achieved when both chiral indices (n, m) are equal or when one of them is equal to zero. When both chiral indices are equal (n = m), the chiral vector (segment AC in Figure 2.1) forms an angle of 30° with both the primitive vectors (a_1 or a_2), which is known as chiral angle. In this case, the nanotube is called armchair, and its axis is perpendicular to a C-C bond. On the other hand, if one of the chiral indices is equal to zero, the nanotube is called zigzag. The chiral angle between the zigzag chiral vector (segment AB) and one of the primitive vectors is conventionally set to zero. On the contrary, chiral SWCNTs are formed when the n and m chiral indices are different and none of them is equal to zero. Chiral SWCNTs have chiral angles that range between zero and thirty degrees, and are characterized by having right or left handed helicity with corresponding mirror image on the opposite hand[16]. Through the study of the band structure of different carbon nanotubes, it has been proven that all armchair nanotubes present a metallic electronic behavior.[3] On the other hand, the electronic properties of zigzag and chiral tubes will mainly depend on their chiral indices. If the result of $|n - m|/3$ is an integer, the nanotube will behave similarly as armchair tubes with a set of wave vectors within the Brillouin zone occupying degenerated states at the Fermi level.[2,3] If otherwise, $|n - m|/3$ is not an integer, a wave vector will not touch the degenerated state and a band gap will be present in the electronic density of states of the nanotube. These tubes will consequently behave as semiconducting materials.[2,3] Unfortunately, SWCNTs are not produced by folding graphene sheets at desired angles and their chirality is not easily controlled during synthesis. On the contrary, SWCNTs are produced through complex reaction mechanisms that take place during CVD processes, in which structural control of SWCNTs is hardly achieved.

The most accepted CVD reaction mechanism states that precursor carbon species such as carbon monoxide or ethanol are fed into a reactor chamber at ~700°C. The precursor species in gas phase are put in contact with metallic catalyst nanoparticles, which are generally deposited on catalyst supports such as silica or magnesia. Catalyst nanoparticles are commonly made of iron, nickel, cobalt, or some of their alloys. At the catalyst surface, carbon compounds dissociate leading to diffusion of individual carbon atoms over the surface and into the bulk, and the process is accompanied by the generation of other side products such as carbon dioxide, water, or molecular hydrogen. At the saturation point, carbon atoms in the bulk precipitate onto the surface and start forming carbon chains, rings and, finally, a nanotube cap on the catalyst surface. This is followed by the cap lift off and subsequent growth by addition of more carbon to the cap edge in contact with the catalyst. Scientists have some agreement with respect to the above described catalytic growth mechanism of SWCNTs, which is known as the vapor liquid solid method (VLS),[17,18] although there is still debate on some details regarding the thermodynamic phase of the nanoparticle and carbon solubility.[17,19] Multiple process variables might be tuned independently or simultaneously in order to produce exclusively SWCNTs with high degree of structural selectivity, and this is what makes this task extremely complex.

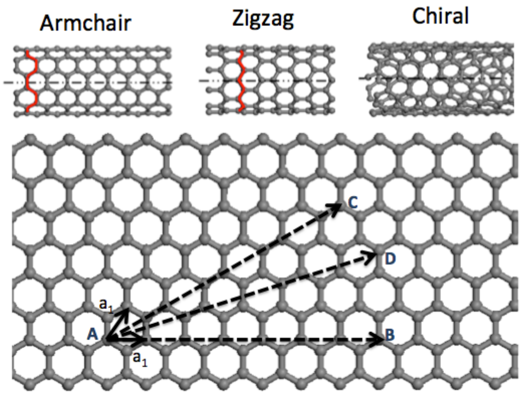

Figure 2.1. Chiral vectors in the graphene lattice and formation of zigzag, armchair and chiral tubes.

Different experimental works have achieved high degree of chiral and electronic type selectivities through optimization of the CVD process. Resasco and coworkers[12] reached a significant improvement over the HiPCO[20] and other processes producing a mixture of SWCNTs with high concentration of (7,5) and (6,5) chiralities in the sample. The process is known as CoMoCAT and uses silica supported catalysts made of cobalt and molybdenum. The catalyst system is placed in a fluidized bed reactor fed with CO at 5 atm of total pressure and 750˚C.[21] The ratio Co:Mo was optimized to stabilize small Co nanoparticles against aggregation allowing the formation of catalyst particles with narrow size distribution with an average diameter around 0.81Å. Theoretically, is has been claimed by different authors that the growth rate of carbon nanotubes is directly proportional to the sine of the chiral angle,[22,23] which is in agreement with the preferential growth of near armchair SWCNTs observed experimentally. Chiang et al[13] suggested a method to enhance the concentration of semiconducting tubes with the (8,4) as the predominant structure. In their approach, the authors proposed to tune the composition of Ni_xFe_{1-x} bimetallic catalysts to improve selectivity. Increasing the fraction of iron in the bimetallic particle enlarge the interatomic spacing in the (111) metallic surface favoring the lattice match between the catalyst surface and the cap of certain chiralities. Harutyunyan and coworkers[14] in turn, found out that an appropriate noble gas environment in the reactor shifts the population of nanotubes with metallic type of conductivity up to 91%. They found that a water-helium mixture in the precursor gas phase favors the formation of iron catalyst particles with large facets and sharp edges, unlike the rounded particles formed in Ar environments. H_2O/He environment was observed to induce shape reversible changes and surface reconstruction in the catalyst particle. Water hindered Ostwald ripening of catalyst nanoparticles favoring narrow diameter distributions and enhancing the nanotube density. On the other hand, water products have been also found to assist selective synthesis of 99% semiconducting tubes via selective etching of metallic tubes.[24-26] The lower ionization potential of the metallic nanotubes makes them vulnerable in oxidative environments. Specific surfaces of quartz used as catalyst support contributed to horizontal alignment and semiconducting selectivity,[27] although the role of the surface on the selective growth remains unclear. In conclusion, different procedures have been proposed regarding chiral and conductive selectivity with extraordinary results; nevertheless, the lack of understanding of reaction mechanisms at atomistic level impedes the systematic formulation of guidelines for high quality and chiral specific growth of single-walled carbon nanotubes.

3. COMPUTATIONAL METHODS

The full mathematical description of atomic or molecular systems is a challenging task due to the complexity of relativistic and quantum phenomena taking place at such nanoscale level. A molecular system can be successfully described through to exact solution of the nonrelativistic Schrödinger equation in its time-independent form:[28]

$$H\Psi(R,r) = E\Psi(R,r) \tag{3.1}$$

Where H is the Hamiltonian, E is the energy of the system, and Ψ is the wave function, which depends on the position of nuclei and electrons, R and r. The analytic solution of the equation (3.1) has only been obtained for single particle cases, and the more complex two-particle case of the hydrogen atom.[29] Therefore, alternative approaches have been proposed to characterize systems with more than two atoms where the Schrödinger equation becomes not exactly solvable. These approximations necessarily involve the use of potentials and functions empirically fit to describe the behavior of nuclei and electrons. For instance, the wave function in the equation (3.1) suggests a wave behavior of the particles in the system. Most of the pioneer experiments in quantum mechanics were able to demonstrate the wave character of electrons through the observation of interference and diffraction, proper of waves.[29] However, nuclei are much heavier and slower objects, with smaller momentums, which results in a very large wavelength according to the Broglie's hypothesis relation,[29] and a consequent absence of wave characteristics in nuclei. The two different behaviors of the main atomic particles make possible to deal with the Schrödinger equation separately for electrons and nuclei through two different mathematical equations; this is known as the Born-Oppenheimer approximation.[28,30] The first equation describes the motion of electrons as function of position of the nuclei:

$$H\psi(r;R) = E\psi(r;R) \tag{3.2}$$

The term $E(R)$ refers to the potential energy surface that is function of the nuclei positions. The solution of the equation (3.2) is the objective of the *ab initio* methods such as *density functional theory* (DFT)[31], which often demand the use of robust computational packages capable of solving complex sets of equations and integrals. These computational tools use empirical fits of the potential energy surface to find a set of solutions ($\psi(r)$) of the Hamiltonian. On the other hand, the second equation describes the nuclei motion in the potential energy surface:

$$H\Phi(R) = E\Phi(R) \tag{3.3}$$

As mentioned above, nuclei are heavy particles with very large wavelengths, which makes the quantum mechanical effects negligible. Therefore, in order to describe the nuclei motion completely trough classical mechanics, the equation (3.3) can be replaced by the Newton's equation of motion:

$$F = ma \tag{3.4}$$

Where m is the mass of the nucleus and a is the particle acceleration, expressed as the second derivative of the nucleus position with respect to time. The force (F) can be derived from the potential energy surface, as it will be discussed in the next section. The solution of the equation (3.4) is known as *molecular dynamics*.[32]

3.1 Classical molecular dynamics

Molecular dynamics (MD) is a useful tool that allows tracking trajectories of particles in time and predicting several thermodynamics and kinetic properties of materials and fluids. The solution of equation (3.4) requires the inclusion of an empirical fit to the potential energy surface, also called forcefield or interatomic potential. Thus, the equation (3.4) can be rewritten as:

$$-\frac{dV}{dR} = m\frac{d^2R}{dt^2} \tag{3.5}$$

Using accurate representation of the molecular system through the empirical forcefields (V), it is possible to track the positional evolution of all atoms through a predetermined timeframe. Once the forcefield is known, a numerical integration of the Newton's equation of motion is performed to update atomic velocities and positions after a preset time step (Δt) has elapsed. The initial atomic positions of the system are known from molecular or crystal databases or *ab initio* calculations with higher level of theory, whereas the initial velocities are often assigned following a Maxell-Boltzmann distribution[28] to match the average atomic velocities to the kinetic energy established by the temperature set point. The total energy (U) of the system is the sum of the potential and kinetic energies ($U = V + K$); the potential is given by the interatomic potential, whereas the kinetic energy is given by:

$$K = \frac{1}{2}\sum_{j=1}^{N} m_j v_j \bullet v_j \tag{3.6}$$

Where N is the total number of particles in the system and v_j is the velocity vector for the particle j, corresponding to the first derivative of the atomic positions with respect to time. Statistical mechanics treatment of the thermodynamic quantities leads to a temperature-dependent expression of the kinetic energy:

$$K = \frac{3}{2}Nk_BT \tag{3.7}$$

By computing an arithmetic average of the right hand term of the equation (3.6), and then combining with equation (3.7), we can obtain a temperature expression as a function of particle velocities, and the Boltzmann constant (k_B).

$$T = \frac{1}{3Nk_B}\left\langle \sum_{j=1}^{N} m_j v_j \bullet v_j \right\rangle \qquad (3.8)$$

The equation (3.8) is used by thermostat algorithms to adjust the average particle velocities to the target temperature. All thermodynamic and mechanical variables can be calculated in a similar fashion as the temperature, by knowing atomic positions and velocities at any instant of the simulation.[32] The thermodynamic and mechanical behavior of the systems can be tracked by following the dynamic response of the main variables. The pressure can be also set at the beginning of an MD simulation and controlled through barostat algorithms that adjust the atomic velocities to the stress tensor components of the hydrostatic pressure, assuming that the mass and volume of the system is known. The combined action of thermostat and barostat defines the thermodynamic ensemble[32] that is governing the MD simulations. The simplest case of the absence of control over the temperature and pressure correspond to microcanonical ensemble in which the total number of particles, the volume of the system and the total energy are held constant through the simulation (NVE). If a thermostat is introduced to control the temperature of the system, the statistical state of the system will be represented by the canonical ensemble (NVT). The addition of barostat along with the thermostat will restrict the system to an NPT behavior where the total energy and volume of the system are allow to change to control pressure and temperature simultaneously. Several thermostats[33] have been used in molecular dynamics simulations to describe system in thermodynamic equilibrium, including the Nosé and its Hoover correction, and the generalized Langevin equation. The Nosé thermostat represents the equilibrium energy of the system according to the canonical distribution in coordinate and momentum space. The Langevin thermostat,[34,35] on the other hand, is recommended for non-equilibrium systems. With this thermostat, the classical Newton's equation of motions is replaced by stochastic differential equations representing friction forces and random other forces. Detailed procedures and mathematical treatment of these thermostats can be found in the references.[32,33]

The total initial energy will then be given by the sum of potential and kinetic energies at an initial time t_0. An atomic position x_j at a given time, $t_k = t_0 + k\Delta t$, will be calculated by integrating the Newton's equation of motion using the total force acting over a particle j at a time t_{k-1}. A molecular dynamics trajectory is generated after an L number of predefined steps have been completed, and the time, $t_L = t_0 + L\Delta t$, has been reached. Typical time steps in classical molecular dynamics are in the order of femtoseconds (10^{-15} s). Depending on the objective of the MD simulation, the total simulation time ($L\Delta t$) range between 1 and 15 ns.

Generation of MD trajectories implies the numerical solution of the equation (3.5), trough an integration that is broken down in small stages (Δt). Algorithms proposed to solve this differential equation use Taylor series expansions[36] to approximate positions, velocities, and accelerations at a time $t + \Delta t$:

$$r_j(t+\Delta t) = r_j(t) + \Delta t \cdot v_j(t) + \frac{1}{2}\Delta t^2 a_j(t) + \frac{1}{6}\Delta t^3 b_j(t) + \frac{1}{24}\Delta t^4 c_j(t) + \ldots \tag{3.9}$$

$$v_j(t+\Delta t) = v_j(t) + \Delta t \cdot a_j(t) + \frac{1}{2}\Delta t^2 b_j(t) + \frac{1}{6}\Delta t^3 c_j(t) + \ldots \tag{3.10}$$

$$a_j(t+\Delta t) = a_j(t) + \Delta t \cdot b_j(t) + \frac{1}{2}\Delta t^2 c_j(t) + \ldots \tag{3.11}$$

Where a is the acceleration, defined as $a = F_j/m = (dV/dr)/m$. One of the simplest and most used methods based on Taylor series expansions is the Verlet algorithm.[36] This method uses a series of equations to updated atomic positions taking the accelerations and atomic positions at t and $t - \Delta t$ as a reference. Although the method implicitly considers the velocities of each particle in the system, a velocity term does not explicitly appear in the finite difference equation for the integration of the equation of motion:

$$r_j(t+\Delta t) = 2r_j(t) - r_j(t-\Delta t) + \Delta t^2 a_j(t) \tag{3.12}$$

Velocities for all particles can, however, be obtained through mathematical manipulations of the Verlet model, though this represents a significant drawback since the velocities for each particle j (v_j) cannot be calculated until the positions at $t + \Delta t$ have been computed. Furthermore, the negligibility of the term $\Delta t^2 a_j(t)$ compared to the bigger terms $2r(t)$ and $r(t - \Delta t)$, affects the precision of the simulation and restrict it to work with small time steps.

Predictor-corrector algorithm[36] is perhaps the pioneer of stable numerical algorithms capable of integrating ordinary differential equations with large time steps. The method requires the completion of three steps, a preliminary prediction of the variables and evaluation of the functions, followed by a correction of the initial prediction (PEC). In molecular dynamics simulations, positions, velocities, and accelerations are predicted for $t + \Delta t$ using the Taylor series expansions (equations 3.9 to 3.11). The position calculated by the equation (3.9) ($r_j^c(t + \Delta t)$) is used to evaluate new forces and new accelerations thorough the equation (3.5). The difference between the predicted and evaluated acceleration, $\Delta a(t + \Delta t) = a_j^c(t + \Delta t) - a_j(t + \Delta t)$, is then used to calculate the corrected motion variables:

$$r_j^c(t+\Delta t) = r_j(t+\Delta t) + c_0 \Delta a(t+\Delta t) \tag{3.13}$$

$$v_j^c(t+\Delta t) = v_j(t+\Delta t) + c_1 \Delta a(t+\Delta t) \tag{3.14}$$

$$a_j^c(t+\Delta t) = a_j(t+\Delta t) + 2c_2 \Delta a(t+\Delta t) \tag{3.15}$$

The coefficients c_0, c_1, and c_2, are a set parameters that are based on the order of the derivative of the position. The set of equations shown above correspond to the Taylor series expansion truncated to the second derivative term ($a(t)$). Thus, the coefficients that better represent the expansion series for the motion variables are $c_0 = 1/6$, $c_1 = 5/6$, and $c_2 = 1$.[36] A typical MD algorithm for integration of the Newton's equation of motion following the predictor-corrector procedure is illustrated in the flowchart of the figure 3.1.

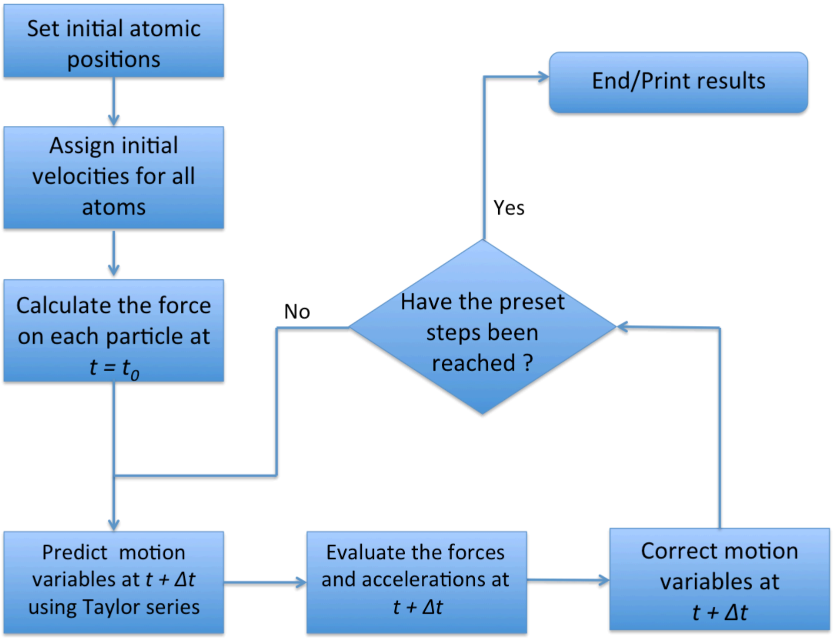

Figure 3.1. Molecular dynamics flow chart following the predictor corrector integration method.

The reliability of any molecular dynamics simulations depends on the appropriate selection of a semi empirical potential. All possible interactions between a given pair of atoms must be well described by the chosen set equations. The wide variety of electronic behavior of atoms, chemical and hybridization states of atoms, and chemical bond types, makes the representation of interatomic interactions much more complex. General equations have been developed aiming to include all elements of the periodic table and all possible types of interaction between atoms of these elements. Universal equations generally include terms accounting for valence, cross and nonbond terms.[28,37] The valence, or bond term, is mainly defined by the chemical bond stretching, angles between three atoms, and dihedral torsion angle. The cross terms are included in most advance second generation force fields to represent the energy distortions caused by the presence of nearby atoms. Finally, Van der Walls, Coulomb and hydrogen bond interactions constitute the nonbonding term. Depending on the simplicity of the interatomic interactions, terms of the general force field equation can be cancelled until a less complex equation is found, capable of an accurate description of the system. However, non-directional and non-polar bonds, such as the metallic bond, have been better represented by very specialized pair and many body potentials. The Sutton-Chen[38] many-body potential has been proved to accurately describe properties of most of transition metals. The equation includes a pairwise component and a density expression to correct the interatomic energy due the nonlocal effects caused other neighbor atoms in the system. Similarly, the basic general form of the force field does not represent chemical reactions. The bond states as described by the universal force field do not allow bond formation and breaking. Consequently, bond order parameter must be included in the valence term to regulate the bonding interactions according to the chemical state and hybridization of atoms involved. The reactive empirical bond order potential (REBO)[39] developed by Brenner or the Reax force field (ReaxFF)[40] developed by Van Duin, are good examples of bond order potentials suitable for the description of reactive systems. The complete details about the mathematical treatment and assumptions of reactive and metallic potentials can be found in the references.

Molecular dynamics simulations allow following the dynamic evolution of a system trough the track of different physical variables. Furthermore, the trajectories of all atoms in the three dimensional space can be monitored using visualization tools, which is useful to evaluate the behavior of bond lengths, adsorption sites, reactivity of molecular species, or degree of order or disorder in the system. Mathematical models have been developed to further process the information stored in the atomic trajectories to quantitatively measure the disorder, and/or phase behavior of the system. Along with the radial distribution function (RDF) and mean square displacement (MSD) the z-density profile[41,42] is one the models proposed to mathematically represent the relative spatial distribution of atoms in the system. Z-density profiles measure the average concentration of atoms in a thin slice of cross sectional area L_x x L_y and a thickness Δz, where L_x and L_y are the dimensions of the simulation box in the x and y axis, respectively. The Z-density profile, also known as local density profile, can be generated through this equation:

$$\rho(z) = \left\langle \frac{1}{\sqrt{2\pi\Delta z}} \sum_j \exp\left(-\frac{(z - z_j)^2}{2\Delta z} \right) \right\rangle \tag{3.16}$$

Where z_j is the z coordinate of the atom j, $z = 0$ is defined for the bottom of the system box.

3.2 Density functional theory

The solution of the equation (3.2) yields a complete description of electron motion for fixed nuclei potions. Despite analytical solutions to this equation have been found for simple cases such as particle in a box, more complex scenarios involving several atoms require numerical approximations. The objective of solving the equation 3.2 is finding the electron ground state energy, *E*, or minimum energy, as a function of nuclei positions. The potential energy surface in the equation (3.2) is an eigenvalue associated to electron an eigenstate (ψ). The wave function ψ corresponds to a set of solutions of the Hamiltonian *H*. The difficulty of solving the Schrödinger equation is related to the complexity of the Hamiltonian operator. The simplicity of known basic quantum mechanics problems, such as the harmonic oscillator[29] or the aforementioned particle in a box, lies on the absence of particle interactions. In these study cases, the Hamiltonian is limited to the description of the kinetic energy of electrons, and sometimes, simple external potential exerted on particles. Conversely, for most materials related problems, interactions between electrons and electrons with nuclei must be taken into account, and therefore included in the Hamiltonian operator for a comprehensive description of the system. Thus, the Schrödinger equation for a system of multiple nuclei and electrons will given by:

$$\left[\frac{h^2}{2m}\sum_{i=1}^{N}\nabla_i^2+\sum_{i=1}^{N}V(r_i)+\sum_{i=1}^{N}\sum_{j<i}U(r_i,r_j)\right]\psi=E\psi \tag{3.17}$$

The expression between brackets corresponds to the Hamiltonian. The first term of this expression represents the kinetic energy of electrons, whereas the second corresponds to the potential energy due the interaction between electrons and nuclei. The third term is the most essential since it defines the potential governing the electron-electron interactions. The electron wave function ψ is actually the collection as a product of individual wave functions as a ψ_i known as the Hartree product. All individual wave functions are function of the spatial coordinates of each electron. The form of the electron-electron potential terms make necessary the evaluation of all individual wave functions $\psi_i(r)$ simultaneously, turning the solution of the Schrödinger equation into a many-body problem. However, no individual wave function can be measured for a given set of coordinates (r), which makes necessary introducing the probability distribution of the particle. This variable is expressed as the product of individual wave functions and their complex conjugates ($|\psi_i(r)|^2$). The sum over the products associated to each electron in the system is known as the electron density and represents the probability of finding N electrons at a particular set of coordinates r. It can be written as:

$$n(r)=2\sum_i\psi_i^*(r)\psi_i(r) \tag{3.18}$$

The term inside the summation is interpreted as the individual probability of an electron with a wave function ψ_i occupying a set of special coordinates *r*. The coefficient 2 outside the summation term comes from the Pauli exclusion principle that states that only two electrons with opposite spin states can occupy an eigenstate, or electron wave function ψ_i. A density functional theory (DFT) algorithm[31] aims to find an electron density that minimizes the energy of the system and solves the time independent Schrödinger equation. Hohenberg and Kohn[43] demonstrated that the ground state energy of the Schrödinger equation is unique functional of the electron density ($E[n(r)]$). This postulate is known as the first Hohenberg-Kohn theorem, which also leads to state that the electron density corresponding to the ground state uniquely determines the Hamiltonian operator, and therefore, all ground-state properties of the system such as energy and wave function. Hohenberg-Kohn postulated a second theorem[43] stating that the Schrödinger equation is fully solved if and only if the electron density that minimizes the energy of the functional is the ground-state electron density. One of the biggest challenges of DFT is to find the correct form of the energy functional so that the true electron density can be searched. The usefulness of both Hohenberg-Kohn lies in the reduction of the degrees of freedom of the time independent Schrödinger equation from 3N to 3, where N is total number of electrons in the system. Thus, the Schrödinger equation and the energy functional are now function of single electron wave functions ψ_i, considering that they constitute the electron density function according to the equation (3.18). The formal way to represent the energy functional is dividing it in 5 different energy contributions that includes all possible classical and quantum interactions between electrons and nuclei:

$$\begin{aligned} E[\{\psi_i\}] = \frac{h^2}{m}\sum_i \psi_i^* \nabla^2 \psi_i d^3r + \int V(r)n(r)d^3r + \frac{e^2}{2}\iint \frac{n(r)n(r')}{|r \bullet r'|} d^3r d^3r' \\ + E_{ion} + E_{XC}[\{\psi_i\}] \end{aligned} \tag{3.19}$$

Similarly to the terms in the Hamiltonian of the equation (3.17), the first three terms of the functional (equation 3.19) represent the kinetic energy of the electrons, electron-nuclei potential, and the electron-electron interaction, respectively. The fourth term corresponds to the energy due to the interactions between a pair of nuclei (E_{ion}). All these energies correspond to pure coulomb interactions between pair of particles, and do not include quantum mechanical effects. The first fourth terms are also known as the "known" part of the functional. The fifth and last term of the total energy functional is the exchange correlation function, which does include all quantum effects not considered in the "known" part of the energy. The specification of the exchange-correlation function is the critical step in defining the form of the energy functional. Nevertheless, Kohn and Sham[44] later developed a set of equations necessary to find the true electron density that minimizes the energy functional, assuming that the exchange correlation functional has been defined through a proper approximation method. The Kohn-Sham equations are functions of single electron wave functions and have the form:

$$\left[\frac{h^2}{2m}\nabla^2 + V(r) + V_H(r) + V_{XC}(r)\right]\psi_i(r) = \varepsilon_i\psi_i(r) \tag{3.20}$$

The Kohn-Sham equations are comparable with the equation (3.17). The absence of summations is related to the simplification of the wave function to a single electron case. The three potentials accompanying the kinetic energy term are potential terms describing the main particles interactions and the quantum mechanical effects. The first potential *V(r)* regulates the interaction between electrons and nuclei, and corresponds to the same potential present in the second term of the equation (3.19). The term V_H is known as the Hartree potential defining the Coulomb repulsion between electrons. The Hartree potential is defined by the following equation:

$$V_H(r) = e^2 \int \frac{n(r')}{|r - r'|} dr' \tag{3.21}$$

The third potential within the bracket is the exchange correlation term, which not includes the quantum mechanical effects, but also corrects the self-interaction excess energy generated from the Hartree potential. The self-interaction is unphysical and comes from the consideration of single electron interaction with a density of electrons in which the single-electron in consideration is also included. The exchange correlation potential, is defined as the functional derivative of the exchange correlation energy respect the overall electron density:

$$V_{XC}(r) = \frac{\delta E_{XC}(r)}{\delta n(r)} \tag{3.22}$$

Solving the Kohn-Sham equations involve an iterative process that allows breaking the loop resulting from the calculation of the electron wave function and the electron density trough two different equations. Thus, an initial electron density must be guessed, and then updated according to the iterative procedure. Once a good initial guess for the electron density is defined, the Hartree potential and the exchange correlation potential are calculated, assuming that the form exchange-correlation functional is known. This will allow the solution of the Kohn-Sham equation (equation 3.20) and the consequent evaluation of the single-electron wave function. The wave function obtained from the Kohn-Sham equation is then used to calculate a new electron density through the equation (3.18), which is compared with the electron density initially estimated. The algorithm stops when both electron densities, the predicted and the calculated, are equal or have reached a convergence criterion. When this happens, one can conclude that the electron wave function and the electron density have been found, and the time independent Schrödinger equation has been solved. The electron density can be used to evaluate the energy of the system using the equation of the functional (equation 3.19), as well as any physical property of interest. The algorithm just described is summarized in flowchart shown in the figure 3.2

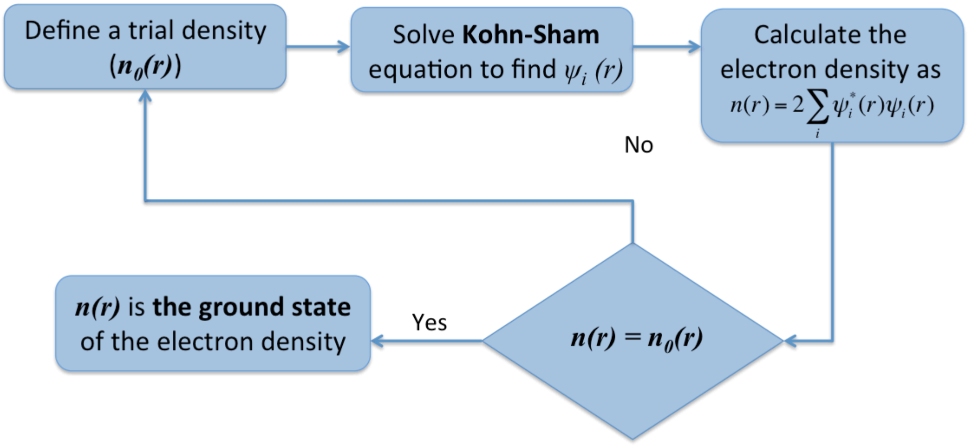

Figure 3.2. Density functional theory algorithm. Procedure to solve the Kohn-Sham equation and find the ground state electron density and wave function.

In order to start solving the algorithm in the figure 3.2, any positive trial density $n_t(r)$ is chosen such that $\int n_t(r) = N$ then $E[n_t] \geq E_0$, where E_0 is the lowest energy eigenvalue. If the convergence criterion is not reached in an electronic density step, a new trial density is estimated through a combination of the old trial density and the density calculated through the set of Kohn-Sham equations.

The accuracy of DFT methods lies on how good the approximation to the exchange correlation functional is. Different functional have been proposed, some of them more elaborated than others, though their reliability is measured by the degree of approximation of their results to data obtained from experimental or higher level of theory methods. The initial development of density functional theory methods led to implementation of the homogenous electron gas to estimate the electron density. This approach considers a constant external potential acting on the electrons, which holds the electron density also constant along the space. This method seems to be physically unrealistic due to the irregular electron density in materials due chemical bonds. However, assuming a uniform electron gas at specific locations facilitates the setting of an exchange correlation functional of the constant electron density at a specific atomic position. This approximation is known as the local density approximation (LDA).[44] Adding the local electron gradient to the local electron density represented a significant upgrade to the LDA method. This approach is the so-called generalized gradient approximation (GGA)[45] type of functional, which is actually a family of exchange correlation functional describing the electron density gradient in different ways. GGA functional are generally more accurate than LDA, but as mentioned above, this not necessarily true and depends on how well the experimental data is matched. Nevertheless, GGA functional are known for correctly representing binding energies between molecules, predicting transition state barriers, and having among the lowest mean relative errors in the calculation of crystal structures, cell volumes, bond lengths, atomization energies, elastic constants and vibrational energies.[46] The typical form of a GGA functional is:

$$E_{XC} = \int n(r)\varepsilon_{XC}(n,\nabla n)\,dr \tag{3.23}$$

Among the most common GGA functional, the Perdew-Burke-Erzenhorf (PBE)[47] is one of the most used. The functional takes general features from the predecessor functional developed by Perdew-Wang in 1991 (PW91),[48] and simplifies it through the inclusion of new derivation in which all parameters are fundamental constants. The new and simpler derivation improves representation of the linear response of the uniform electron gas, and makes the analytical function of the density and its gradient, less complicated, transparent and less parameterized. The general form of the PBE functional is:

$$E_{XC}^{GGA}[n_\uparrow,n_\downarrow] = \int d^3r \cdot n\varepsilon_X(n)F_{XC}(r_s,\zeta,s) \tag{3.24}$$

Note the exchange-correlation energy is now a function electron spin densities. The equation (3.24) presents an exchange-correlation enhancement factor (F_{xc}) introduced to account for the linear response of the uniform electron gas and satisfy the Lieb-Oxford lower bound defined by the exchange correlation energy. The enhance factor is function of the local Seitz radius, the relative spin polarization ζ, and the dimensionless electron density gradient s. ε_X corresponds to the exchange energy per particle of the uniform electron density.

Most of the supercell problems solved by DFT calculations are represented by a set of solutions that satisfy the Bloch theorem, which states that total solution is the sum of plane wave functions. These plane wave functions are more conveniently defined in the reciprocal rather than the real space. Thus, integrals in periodic DFT calculations are numerically solved over the reciprocal (k) space limited by the Brillouin zone (BZ).[31] The Brillouin zone is in turn defined as the primitive Wigner-Seitz cell in the reciprocal space, whose lattice vector dimensions are inversely proportional to the dimensions in the real space. The numerical procedure to solve the integrals in the reciprocal space requires the selection of a discrete set of k points. One of the most recognized methods to select the number of points in the BZ was developed in 1976 by Monkhorst and Pack.[49] The Monkhorst-Pack procedure requires the total number of k points in each direction of the reciprocal space to be set in such a way that the accuracy and the computational cost are balanced. Furthermore, the total of number of discrete points in each direction must be chosen following an inverse proportionality respect to the size of the real space vectors. The inherent symmetry of periodic crystals reduces the evaluation of the integral to a fraction of the BZ known as the irreducible Brillouin zone (IBZ); this consequently allows the minimization of the numerical effort by reducing the total number of k points lying within the IBZ.

As mentioned above, the set of solutions of the Schrödinger for a periodic system equation is governed by the Bloch theorem.[31] This solution is represented by a sum of terms that include the plane wave function and a periodic function in space. The combined term that includes both, the plane wave and the periodic function already expanded in set of special plane waves, present the following form:

$$\phi_k(r) = \sum_G c_{k+G} \exp[i(k+G)r] \tag{3.25}$$

Where *k* and r are the reciprocal and real space vectors, respectively. The *ik* component of the exponential corresponds to the plane wave function, whereas the *iG* portion corresponds to the periodic function in space. *G* is defined as the sum of all vectors in reciprocal space. The equation (3.25) implies that the solution of the Schrödinger equation comes from a summation of infinite number of vectors, corresponding to the plane waves lying with a wide range of kinetic energies. Since plane waves with lower kinetic energies are the ones with a real physical significance, the equation (3.25) can be truncated to the plane waves with kinetic energies lower than an energy cutoff:

$$\phi_k(r) = \sum_{|G+k|<G_{cut}} c_{k+G} \exp[i(k+G)r] \tag{3.26}$$

Where G_{cut} is the truncated set of reciprocal space vectors associated to the energy cutoff as:

$$E_{cut} = \frac{h^2}{2m} G_{cut}^2 \tag{3.27}$$

So far, a complete description of a single point energy calculation for a periodic system has been described. However, calculation of physical properties, such as adsorption energies, reaction energy barriers, or crystal structural calculation, require optimizations of the atomic positions in the system, and sometimes, the simultaneous optimizations of positions and the cell geometry and dimensions. In a DFT geometry optimization the atoms update their positions to instantaneous ground states following numerical methods. The quasi-Newton and the conjugate-gradient are among the most used algorithms to relax the ionic potions.[31] The former uses the forces and the stress tensor to calculate the new atomic positions without taking the total energy into account. The latter, on the other hand, follow an iterative procedure similar to the predictor-corrector described in the classical molecular dynamics section. In this method, a first trial is guessed in the direction of the energy gradient, and the energy and force are reevaluated. The minimum energy is then calculated by a cubic interpolation that takes into account alterations to the energy and forces. The algorithm proceeds with a corrector step in which the minimum energy is updated, followed by a recalculation of the energy and forces. If the components of the force are orthogonal to the previous search direction, the new positions will correspond the minimum; if not, a variant of the Brent's algorithm is used to perform further corrector steps.

DFT calculations allow the accurate calculation of the electronic density of states (DOS) in materials. The DOS (*ρ(E)dE*) is defined as the number of electron states with energies in interval *E, E + dE*. As stated above, the solution of the Schrödinger equations expresses the electron density in the form of plane wave functions, *exp(ik.r)*. The electronic density of states can be obtained from a DFT calculation by integrating the electron density in k space for the energy interval, where the energy associated to these wave functions is given by the following expression:

$$E = \frac{(hk)^2}{2m} \tag{3.28}$$

The full description of the density of states including the spin-polarized DOS, and the electron population relative the Fermi energy level, conductivity, energies associated to highest occupied molecular orbitals (HOMO) and lowest unoccupied molecular orbitals, and band gaps van be estimated through this integration of the electron density.

3.3 Ab initio molecular dynamics (AIMD)

It was shown in the previous sections how to approach the Schrödinger equation separately for electrons and ions taking advantage of the Born-Oppenheimer approximation. The calculation of the electron states require the exact solution of Schrödinger equation, either trough the full description of the electron wave function using *ab initio* methods, or otherwise using electron density approximations such as the density functional theory developed by Kohn and Sham. On the other hand, the independent description of ions reduces the Schrödinger equation to the classical Newton's equation of motion due to the weight of the nuclei and the negligibility of the quantum effects. The numerical solution of the time dependent Newton's motion equation requires the definition of an empirical interatomic potential parameterized to represent physical properties observed experimentally. While the forces acting on each ion are calculated at each instant, the ionic positions are sequentially updated according to the time step used for the numerical integration.

The *ab initio* molecular dynamics method unifies classical and quantum concepts to predict dynamic trajectories of ions. In this case, an interatomic potential is not empirically developed to find the force; instead, the potential energy and the total force acting on each nuclei are calculated from the energy functional of the electron density as obtained from DFT calculations. Using ab initio MD simulations, the ground state energy is calculated solving the Kohn-Sham equations for each step; once this is done, the ground-state potential energy is used to predict new atomic positions and velocities integrating the Newton's equation of motion through numerical methods such as the predictor-corrector. Thus, the interaction potential energy calculated in each time step corresponds to the Born-Oppenheimer potential energy, which is function of the instantaneous quantum state of the electrons and the nuclei positions obtained *via* classical dynamics; because of this, this method is called Born-Oppenheimer molecular dynamics (BOMD).[31,50] In a BOMD simulation, the potential energy is calculated directly from the solution of the time-independent Schrödinger equation, which is not necessarily made through density functional theory methods; wave-function-based methods, such as the Hartree-Fock method, can also determine the energy associated to the electron states with satisfactory results. However, methods based on electron density functional and the solution the Kohn-Sham set of equations offer a reliable, fast, and accurate alternative for the minimization of the energy at each step of a molecular dynamics trajectory. Therefore, if the Kohn-Sham density functional theory is performed at each dynamic step, the general Born-Oppenheimer molecular dynamics trajectory can be as expressed as:

$$m_i \frac{d^2 R_i}{dt^2} = -\nabla_i \min_{\{\phi_i\}} \left\{ \left\langle \psi_0 \middle| H^{KS} \middle| \psi_0 \right\rangle \right\} \tag{3.29}$$

The left hand term of the equation (3.29) corresponds to the well-known classical force definition from the Newton's equation. The term between brackets on the right hand of this equation corresponds to the total ground-state energy, which is minimized respect to the orbitals. The gradient of this minimized energy results in the force acting on the particle *i*. H^{KS} is the Kohn-Sham single particle Hamiltonian. The minimization respect to the orbitals is constrained by the condition of orthonormal orbitals, $\left\langle \phi_i \middle| \phi_j \right\rangle = \delta_{ij}$. This constrain results into the Lagrange's formalism[31,50] whose unconstrained variation with respect to the orbitals leads to a Hamiltonian definition function of Lagrange multipliers Λ_{ij}:

$$H^{KS}\phi_i = \sum_j \Lambda_{ij}\phi_j \tag{3.30}$$

Alternative approaches to Born-Oppenheimer molecular dynamics have been developed. The BOMD method is not an intrinsic dynamics, which means that time dependence of the electronic states is governed by the time dependent nuclei positions calculated through classical dynamics. AIMD methods in which the electronic states evolve in time according to the time-dependent Schrödinger equation rather than the Newton's classical model. This method is known as Ehrenfest molecular dynamics[50] and share similar features with the BOMD method regarding the classical and quantum treatment of nuclei and electrons, respectively. The main difference lies on the time evolution electrons, which is not describe through the static Schrödinger equation, as in BOMD. Other remarkable description of the nuclei and electrons dynamics was revealed by Carr and Parrinello, who unified the separate description of nuclei motion and electronic ground state into an extended quantity that combines classical and quantum total (kinetic and potential) energies; this quantity is called the Carr-

Parrinello's extended Lagrangian. This AIMD method is known as Carr-Parrinello molecular dynamics (CPMD),[31,50] which includes dynamic degrees of freedom to the electrons as in the case of the Ehrenfest molecular dynamics. However, the CPMD method reduces the quantum description of the electron potential energy, to a classical derivative of the functional with respect to the orbitals. This approach allows the use of large time steps for the dynamic trajectories, which is restricted by the electronic dynamics in the Ehrenfest model. Detailed information about Ehrenfest and Carr-Parrinello methods can be found in the references.

4. INTERPLAY OF CATALYST SIZE AND METAL-CARBON INTERACTIONS ON THE GROWTH OF SINGLE WALLED CARBON NANOTUBES[*]

4.1 Summary

Single-wall carbon nanotubes grow by decomposition of a carbon-containing precursor gas over metal nanocatalysts. It is known that shape, size, and chemical nature of the catalysts play significant roles in the nucleation and growth processes. Here we use reactive molecular dynamics simulations to analyze how the catalyst particle size and the strength of adhesion between the surface and nascent carbon structures may affect the growth process. As a result we determine if the process leads to cap lift-off or if it causes graphitic encapsulation and therefore poisoning of the catalyst. In agreement with the Hafner-Smalley model, our MD simulation results illustrate that the work of adhesion must be weak enough so the curvature energy of a spherical fullerene is less favorable than that of a single-wall carbon nanotube of the same diameter, thus allowing the cap lifting process to take place. Moreover, we propose that a simple model combining curvature energy and kinetic effects may help to identify regions of single-wall carbon nanotube growth in the phase space defined by work of adhesion, temperature, and catalyst size.

4.2 Introduction

Since their discovery in 1993 by Ijima,[51] single-wall carbon nanotubes (SWCNTs) have been the subject of numerous experimental and theoretical investigations focusing on the analysis of their excellent mechanical and electrical properties as well as on their structure/property relationships and applications.[52-56] Given

---

[*] Reprinted with permission from Juan C. Burgos, Humberto Reyna, Boris I. Yakobson, and Perla B Balbuena. "Interplay of Catalyst Size and Metal−Carbon Interactions on the Growth of Single-Walled Carbon Nanotubes." The Journal of Physical Chemistry C **114**(15): 6952-6958. Copyright 2010, American Chemical Society.

that structure and therefore properties are defined during the synthesis process, the growth mechanism of SWCNTs has been also extensively studied. Several methods for producing SWCNTs such as laser ablation,[10] arc discharge,[1,57] and chemical vapor deposition (CVD)[58] have been developed in the last decades. Although these methods have achieved a high level of refinement,[59-61] they are still far from reaching complete control over important structural variables such as nanotube length, diameter, and especially chirality.

Here we focus on CVD processes, where recent advances have accelerated progress in selective growth, [21,62,63] although details of the underlying growth mechanisms are not completely understood. A great deal of information has been recently drawn from in situ observations based on transmission electron microscopy (TEM) and high resolution transmission electron microscopy (HRTEM).[64-66] However important questions remain to be answered related to events occurring during synthesis stages, such as carbon feedstock decomposition mechanism, role of the carbon-containing gas flow rate, diffusion rates of carbon atoms inside the catalyst particle and on its surface, carbon saturation level reached inside the catalyst particles before starting the nucleation, effect of the catalyst particle size on nucleation and structure of the nascent nanotubes, and reasons for catalyst poisoning, among others.

Graphitic encapsulation of catalyst particles has been thoroughly studied. Some of the best known requirements to avoid encapsulation are high kinetic energy of the carbon atoms on the surface[67,68] and fast carbon diffusion.[69,70] However, based on the fact that either spherical-like fullerenes or single wall carbon nanotubes may grow from the same catalyst particle of a given diameter, Hafner et al[71] proposed that due to the exceeding degree of curvature of the fullerene ball with respect to that of the nanotube, the energy per atom of a SWCNT will be lower than that of a spherical fullerene of the same diameter, and therefore there would be always growth of SWCNTs unless the work of adhesion of carbon to the metal catalyst (W_{ad}) is strong enough to make the energy of the spherical fullerene lower than that of the nanotube.

To analyze this proposal, the energies per C atom relative to that of a graphite sheet for both SWCNT and spherical fullerenes can be calculated. A mathematical expression based on the classical theory of elasticity has been proposed to represent the curvature energy of a carbon nanotube E_{cT}[72,73]:

$$E_{cT}(D) = \frac{C}{D^2} \tag{4.1}$$

Where D is the nanotube diameter, assumed to be the same as that of the catalyst particle, and C is a constant that depends on Young modulus, tube thickness, and atomic volume. The curvature energy can be calculated for several tube diameters as the difference of total energy between a carbon nanotube and that of its corresponding graphene sheet using ab initio methods,[72,74,75] yielding a value of 0.084 $\mathrm{eV.nm^2}$ for the constant C.

On the other hand, Adams et al[76] found an expression to calculate curvature energies of fullerene balls as a function only of n, the total number of atoms in the fullerene. But in order to do a fair comparison with the results of Equation (4.1), it is useful to rewrite the equation using the same dependent variable, thus converting n to D. Considering that the surface number density $\sigma = n/\pi D^2$ is a constant value for spherical fullerenes that can be calculated for C_{60} for which $D = 0.71$ nm,[77] then for any spherical fullerene with n atoms, the diameter D is related to n by: $D = 0.71*(n/60)^{½}$. Substituting this relationship in the equation proposed by Adams et al[76] yields an expression for the curvature energy of fullerenes:

$$E_{cF}(D) = 0.351666\left(\frac{1}{D^2}\right) - 0.065895\left(\frac{1}{D^2}\right)^2 \tag{4.2}$$

Figure 4.1 illustrates Hafner-Smalley's model that the energy of a cylindrical fullerene would be lower than that of a fullerene with a spherical shape for any particle diameter even though both energies get closer when the diameter increases. However, in presence of the catalyst, the work of adhesion between carbon and catalyst atoms becomes really decisive to determine growth or encapsulation. For example, at strong metal-carbon interactions, the curvature energy of the spherical fullerene may become lower than that of the nanotube, even reaching or overcoming the curvature energy of a SWCNT, thus favoring catalyst encapsulation.

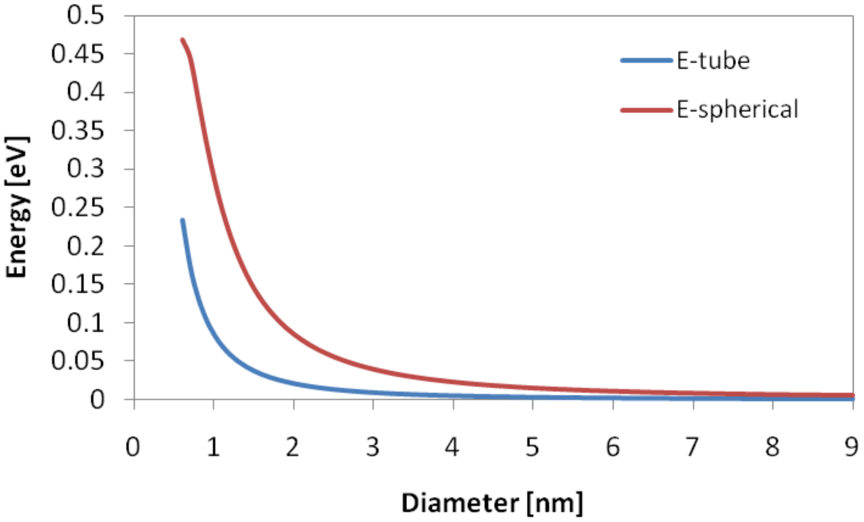

Figure 4.1. Energies per C atom of SWCNTs and spherical fullerenes relative to an infinite graphite sheet as function of their diameters.

Therefore, the necessary condition for growth of SWCNTs can be mathematically represented as follows:

$$E_{cT} < E_{cF} - W_{ad} \tag{4.3}$$

and rewritten as:

$$W_{ad} < E_{cT} - E_{cF} \tag{4.4}$$

The inequality (3b) indicates that for SWCNT growth the strength of interaction (W_{ad}) between a graphite sheet and catalyst atoms must be lower than the difference of curvature energies of fullerene balls and carbon nanotubes of a given diameter.

Computational techniques such as classical molecular dynamics (MD) simulations and ab initio calculations have been successfully used in order to observe and understand events taking place at the atomic level during the growth process.[78-83] In previous work, our group developed a reactive force field that describes C-C and C-metal interactions[84] and a molecular dynamics algorithm[85] that is able to simulate the CVD process under the real conditions of pressure and temperature. The simulation results[80,86] have illustrated possible stages of nanotube growth: from the dissolution of carbon inside the catalytic particle, followed by precipitation of C atoms on the surface forming chains and then rings, and finally formation of a cap that eventually lifts off and becomes a growing single-wall carbon nanotube.

Recently Ribas et al[87] using these force fields and MD algorithm were able to identify a phase diagram, that for a fixed catalyst size, describes the conditions of temperature and W_{ad} where SWCNT growth is possible, as well as regions of that phase space where the catalyst is encapsulated. In this work we address an important related question regarding the effect of catalyst size, along with the chemical nature of the catalyst (given by W_{ad}), on SWCNT growth at a typical temperature of current synthesis processes (1000 K). MD simulations are used to prove the theoretical analysis of Hafner-Smalley et al., focusing on the implications of the curvature energy when a fullerene cap starts to nucleate over the catalyst, and on the combination of catalyst properties (particle size and metal-carbon work of adhesion) that would determine cap lift-off without graphitic encapsulation. Moreover, the growth mechanism and also the impact of the catalyst diameter on the structure of the nanotube are also analyzed. We expect that new insights can provide the key for understanding structural selectivity and for avoiding catalyst poisoning.

4.3 Computational and system details

Our MD simulation setup consists of a metal cluster floating in a gas phase inside a periodic box; the gas phase corresponds to C-containing precursor molecules randomly distributed in the box which are irreversibly catalyzed (converted into C atoms) when they get close enough to the metal surface. Carbon-carbon interactions are represented by a modified potential[84] based on the second-generation reactive REBO potential developed by Tersoff and Brenner which allows bond formations and bond breaking and is able to describe the main phases of carbon: graphite and diamond and their phase transformations.[39] Metal-metal interactions are described by the Sutton-Chen many body potential that is widely employed for transition metals.[38] Metal-carbon interactions are given by the reactive potential developed by Martinez-Limia et al,[84] that follows the Tersoff-Brenner scheme for C-C interactions, and incorporates a new potential between carbon and metal atoms. The metal-carbon potential depends on the total number of metal atoms surrounding a carbon atom, and also on carbon hybridization. A relationship between the work of adhesion (W_{ad}) and the metal-carbon interaction strength for carbon atoms with sp2 hybridization was obtained by Ribas et al.[87] Such relationship, found from a set of MD simulations of a graphene sheet located above a Ni(111) slab (see Ref. 41 for full details), permitted us to relate W_{ad} to values of the potential parameter representing the metal-carbon interaction strength for sp2 carbon atoms.[84]

MD simulations were carried out over eight different sizes of Ni clusters between Ni_{12} to Ni_{160}, each metal particle was placed inside a periodic cubic box with an edge length of 5 nm. For each particle size simulations were performed at ten different W_{ad} between 30 and 210 meV approximately. The precursor gas density was kept constant during each simulation at 0.04 atoms/nm^3, at 1000 K, to simulate experimental synthesis conditions.[21,62] This set of simulations was repeated five times (a total of 400 MD simulations) with the objective of developing a statistical analysis. The equations of motion were integrated using the predictor-corrector algorithm with a time step of 0.5 fs. The initial total number of steps was set as 30 million, although sometimes it was not necessary to reach this limit since we were interested in the first stages of the process where important events such as encapsulation or cap lift off may occur.

4.4 Results and discussion

Each simulation yields one of two possible scenarios: cap lift-off or graphitic encapsulation. MD simulations provide detailed information about the critical instant where the system must choose between both scenarios. Figure 4.2 shows the evolution of the system from the initial bare metallic cluster. At the chosen process density (0.04 molecules/nm^3), there are at least 4 atoms of the precursor gas in the periodic box during the whole simulation, this represents a high probability of collision between metal and precursor gas atoms. When the precursor atoms are in contact with some of the surface metal atoms, they are immediately irreversibly catalyzed becoming carbon atoms. The first catalyzed carbon atoms easily dissolve into the catalyst particle because the floating small metal cluster is highly flexible and mobile at the high temperature of the process. Once the number of carbon atoms inside the cluster increases, the mobility of the cluster becomes reduced due to the presence of carbon atoms located in interstitial sites able to lock metal atoms in their sites as illustrated at 0.25 ns in Figure 4.2. This reduced mobility in the metal atoms leads to a decrease of carbon solubility in the cluster, therefore, new catalyzed carbon atoms would prefer to adsorb onto the catalyst surface without diffusing into it, even if the cluster has not reached a saturation limit. In addition, metal-carbon interactions inside the cluster are quite weak and single carbon atoms may flow from inside toward the surface to form covalent bonds with other adsorbed atoms; thus, forming dimers, trimers, and then longer carbon chains and rings on the catalyst surface as shown at 0.5 ns in Figure 4.2.

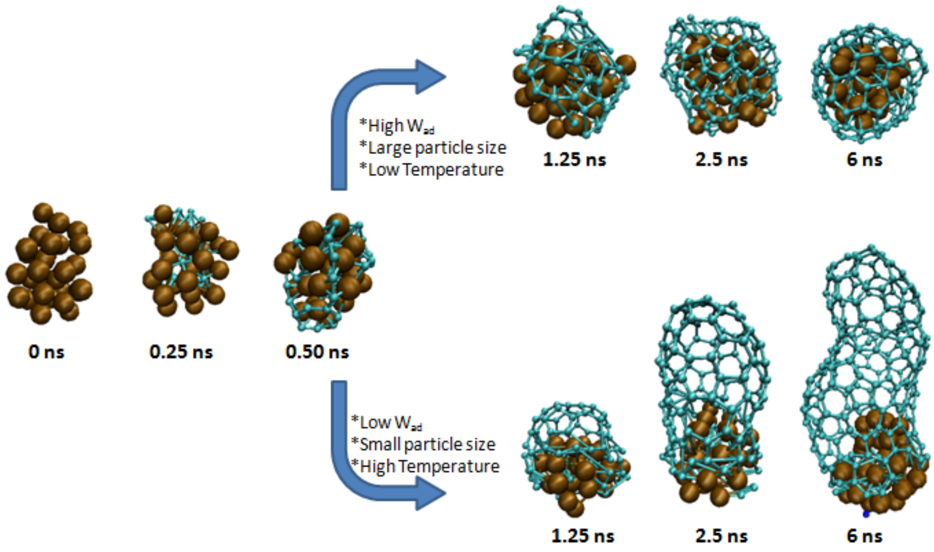

Figure 4.2. Scheme of SWCNT growth as described by MD simulations. Combination of several synthesis conditions could lead to a graphitic encapsulation or cap-lift off and later growth.

After 0.5 ns the addition of more carbon atoms may lead to graphitic encapsulation or otherwise to the growth of a single wall carbon nanotube, depending on combination of variables such as temperature, and nature of the catalyst (particle size and work of adhesion). Several publications[67,68,87] have reported that in order to observe cap lift-off the kinetic energy of carbon atoms must be high enough to overcome the work of adhesion, that is, high temperatures raise the probabilities of observing cap lift-off (1.25 ns, Figure 4.2, bottom) resulting in subsequent growth (2.5 and 6 ns, Figure 4.2, bottom). On the other hand, if the work of adhesion overcomes the kinetic energy of the carbon atoms, carbon rings and chains would remain strongly attached to the particle surface even though sometimes small caps with diameters smaller than that of the catalyst particle can lift-off the surface (1.25 ns, Figure 4.2, top); however, these small caps would be re-adsorbed on the surface because of the strong metal-carbon bonds. Thereby, new catalyzed atoms would stay on the surface building carbon structures until complete catalyst encapsulation (2.5 and 6 ns, Figure 4.2, top).

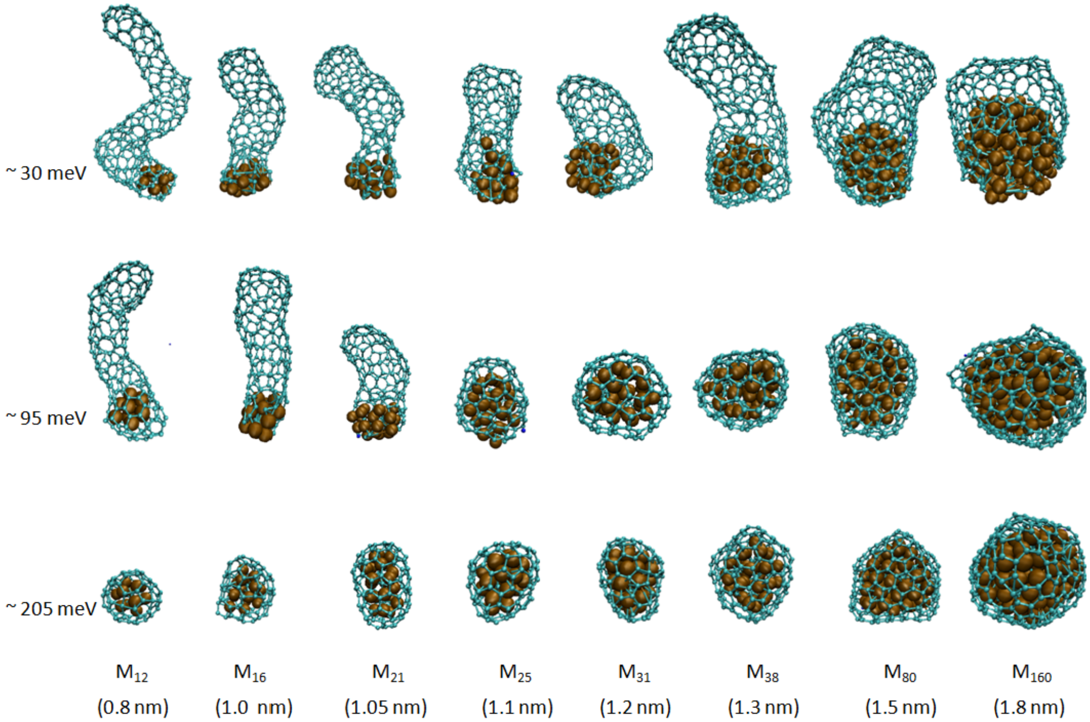

Figure 4.3. Cap lift-off versus graphitic encapsulation at 1000 K. Large particle diameters and strong adhesion forces between catalyst and nascent carbon structures could cause encapsulation of the catalyst. Values between parentheses correspond to particle diameters of the M_n catalyst particles. Values on the left correspond to the work of adhesion of the shown systems.

In addition to the kinetic energy, the catalyst particle size also plays an important role on determining growth or encapsulation. Figure 4.3 shows the result of MD simulations performed at 1000 K, at three different works of adhesion (W_{ad}), and for eight different particle diameters, showing that a very small work of adhesion (~30 meV) allows the growth of single wall carbon nanotubes for a wide range of particle sizes. In agreement with the Hafner-Smalley model (Equation 4.4) these results suggest that the energetic value for the work of adhesion is not high enough to overcome the difference in curvature energies between the nanotube and its corresponding spherical fullerene of the same diameter in the range of 0.8-1.8 nm. In consequence, this catalyst would not be poisoned unless the metal particle has a diameter larger than 1.8 nm or the synthesis process is carried out at an exceptionally low temperature. In contrast, when the work of adhesion is extremely high (~205 meV), all the catalyst particles in the 0.8-1.8 nm diameter range are encapsulated, this suggests the energetic difference in curvature energies between nanotubes and ball-like fullerenes of same diameter range (0.8-1.8 nm) are always below 205 meV, therefore this catalyst would be always encapsulated unless a high temperature is employed, or a very small catalyst particle is used, which would allow the formation of spherical fullerenes with a higher curvature relative to that of its respective nanotube of the same diameter.

Furthermore, at intermediate values of work of adhesion (~95 meV), nucleation and growth of SWCNT's are observed only for small particle sizes up to ~1 nm (Figure 4.3 middle). Catalysts with particle sizes greater than 1.05 nm are encapsulated for the given process variables. Thus, 1.05 nm would become a limit between growth and encapsulation when the rest of variables are kept constant. However, when the particle size gets close to this limit, the probability of finding either encapsulation or growth in the system starts to be even; therefore systems where the catalyst is finally encapsulated despite the formation of small caps at the beginning of the process are mostly observed at these limiting states (Figure 4.2, at 1.25 ns top, and Figure 4.3, at ~95meV with M_{25}). Thus, at these intermediate states, any minor change in the process variables such as a change in temperature or a slight modification in catalyst diameter may lead to a total encapsulation, or otherwise to an evident growth of a carbon nanotube.

However, since at high temperature there is a high atomic mobility, the nanoparticle changes shape and diameter continuously (in the order of ~0.2 nm). Therefore, the diameter of the fullerenes formed over the catalyst also changes during the process. As a consequence, the difference in curvature energies between fullerene and nanotube of same diameter would not be a constant throughout the process and a critical change in particle diameter due to the mobility of metal atoms could drive the system to either growth or encapsulation, reversing the direction of the inequality 3b. Thus, there is some degree of uncertainty in the transition region where the differences in curvature energies are almost equal to W_{ad}. This can be easily demonstrated by repeating several times the MD simulations at a specified transition point, such as M_{25} at ~95meV and 1000K.

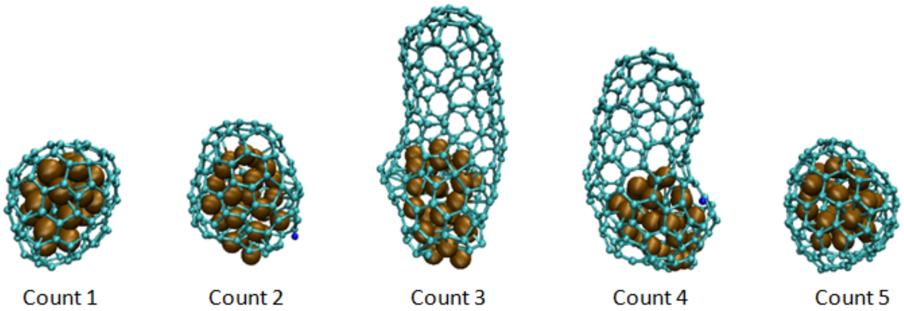

Figure 4.4. Molecular dynamics simulations carried out five times over the same catalyst particle (M_{25}) at the same W_{ad} (95 meV) and temperature (1000 K). The results are not totally reproducible despite all the conditions are being replicated. Growth or encapsulation can be observed since the conditions correspond to a metastable transition point.

The results are illustrated in Figure 4.4, where despite the simulations were carried out at the same conditions (temperature, W_{ad}, catalyst size, density, etc) encapsulation was observed three times, while growth was only observed twice.

The statistical results are summarized in Figure 4.5 which shows the count of number of growths (height of the blue bars) obtained at every state. Despite the bar heights distribution in Figure 4.5 seems to be somewhat random, it provides the approximate location of the transition points where the differences in curvature energy equals the energy of adhesion between metal and carbon. As seen in Figure 4.5, states far away from the transition region (small particle size and low W_{ad}) show consistent growth. Changes in shape and diameter undergone by catalyst at those conditions are not enough to induce the formation of a spherical fullerene with significantly high curvature energy. However, as the particle size increases, transition points move toward lower W_{ad}. It is noted that the transition points are not located exactly at a given W_{ad} value, instead, for every particle size there is a range of W_{ad} between 30-50 meV in which growth is observed randomly, and the probability of predicting either growth or encapsulation becomes very low. As the particle size increases further, the transition region moves totally toward low W_{ad}, and for a wide range of W_{ad}, encapsulation is constantly found (no blue bars in Figure 4.5). This is because at large catalyst sizes, the temperature effects on the mobility of the metal atoms are less significant.

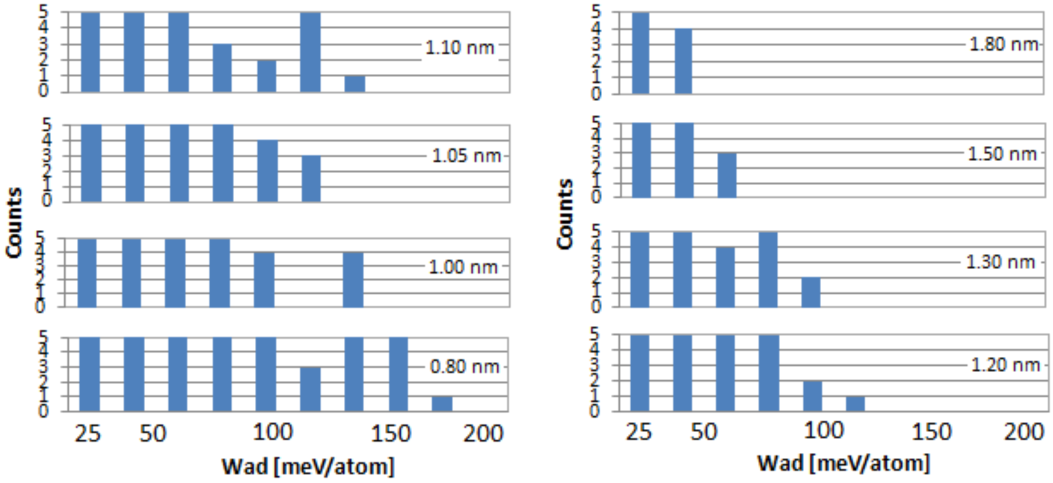

Figure 4.5. Statistical plots of the number of nanotubes formed at a given catalyst particle size from 0.8 nm to 1.8 nm at different Wad from ~25 meV to ~210 meV.

The results shown in Figure 4.5 are translated to a phase diagram in Figure 4.6 where the blue curve represents states between growth and encapsulation, and the vertical black bars signify the range of uncertainty in which probabilities of finding either growth or catalyst poisoning are even. We note that the transition line has many different slopes on its trajectory. The temperature effects described above may be related with this behavior. The global trend of the limiting curve calculated from MD simulations is quite comparable with that theoretically obtained from Hafner et al[71] (dotted red line in Figure 4.6).

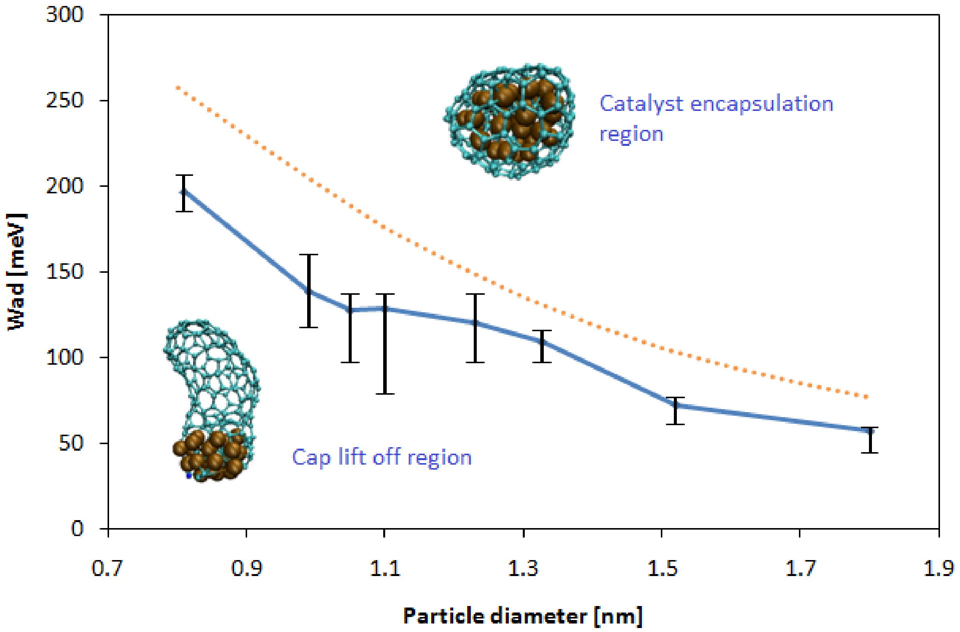

Figure 4.6. W_{ad} versus particle diameter shows a clear differentiation between a wide catalyst encapsulation region and a cap lift-off region, as calculated by MD simulations (solid line) at 1000 K. The dotted line corresponds to the analytical equation for the difference between the curvature energies of the fullerene capsule and that of a SWCNT. Theoretically, all combinations W_{ad}- particle diameter below this line should lead to a cap lift-off.

As discussed above, the competition between cap-lift off and graphitic encapsulation can be explained from the differences between curvature energies per carbon atoms from spherical fullerenes and nanotubes relative to an infinite graphite sheet. It was proposed that W_{ad} is an energy that reduces the curvature energy of spherical-like fullerenes (inequality 3a). However, W_{ad} is not the only energy directly involved, and the kinetic energy E_k of the carbon atoms in the carbon structures plays the opposite role to that played by W_{ad}, lowering the curvature energy of the nanotubes when the temperature is increased. Therefore, the mathematical expression (inequalities 3a and 3b) provided previously as necessary condition to observe cap-lift off can be rewritten including the temperature effects on the curvature energies of the fullerenes.

Thus, a negative kinetic energy term is included on the left side of the inequality 3a in order to have a more complete model where kinetic and curvature energy effects are involved, so inequalities 3a and 3b can be rewritten as follows:

$$E_{cT} - E_K < E_{cF} - W_{ad} \qquad (4.5)$$

Therefore,

$$W_{ad} < E_{cF} - E_{cT} + E_K \qquad (4.6)$$

The blue curve in Figure 4.6 intrinsically includes the kinetic term since all the simulations were performed at 1000 K, for that reason the theoretical curve (red dotted line) and the blue curve from MD simulations cannot be quantitatively compared. However, taking advantage of the qualitative similarity and based on inequality 4b, it is possible to predict the tendency of the transition line as the process temperature is modified.

In order to accomplish this goal, we define a new energetic variable as function of particle diameter and temperature $\bar{E}(D,T) = E_{cF} - E_{cT} + E_K$, assuming that nanotubes and fullerene balls take the same diameter as the catalyst particle. This energetic variable can be calculated based on equations (4.1) and (4.2), and approximating the kinetic energy as $E_K \approx k_B T$, where T is the temperature and k_B is the Boltzmann constant. After plotting $\bar{E}$ as function of the fullerene diameter and for different temperatures (Figure 4.7a), it is seen that the transition lines are moved down when the temperature gets lower, making the growth zone smaller and increasing the probability of catalyst poisoning. Thus, when a set of growth conditions is established (W_{ad}, T, and D) and the pair (D, W_{ad}) is located in the graph $\bar{E}$ vs. D, the growth of a single wall carbon nanotube would be assured if the point (D, W_{ad}) is located below the theoretical isotherm corresponding to the process temperature.

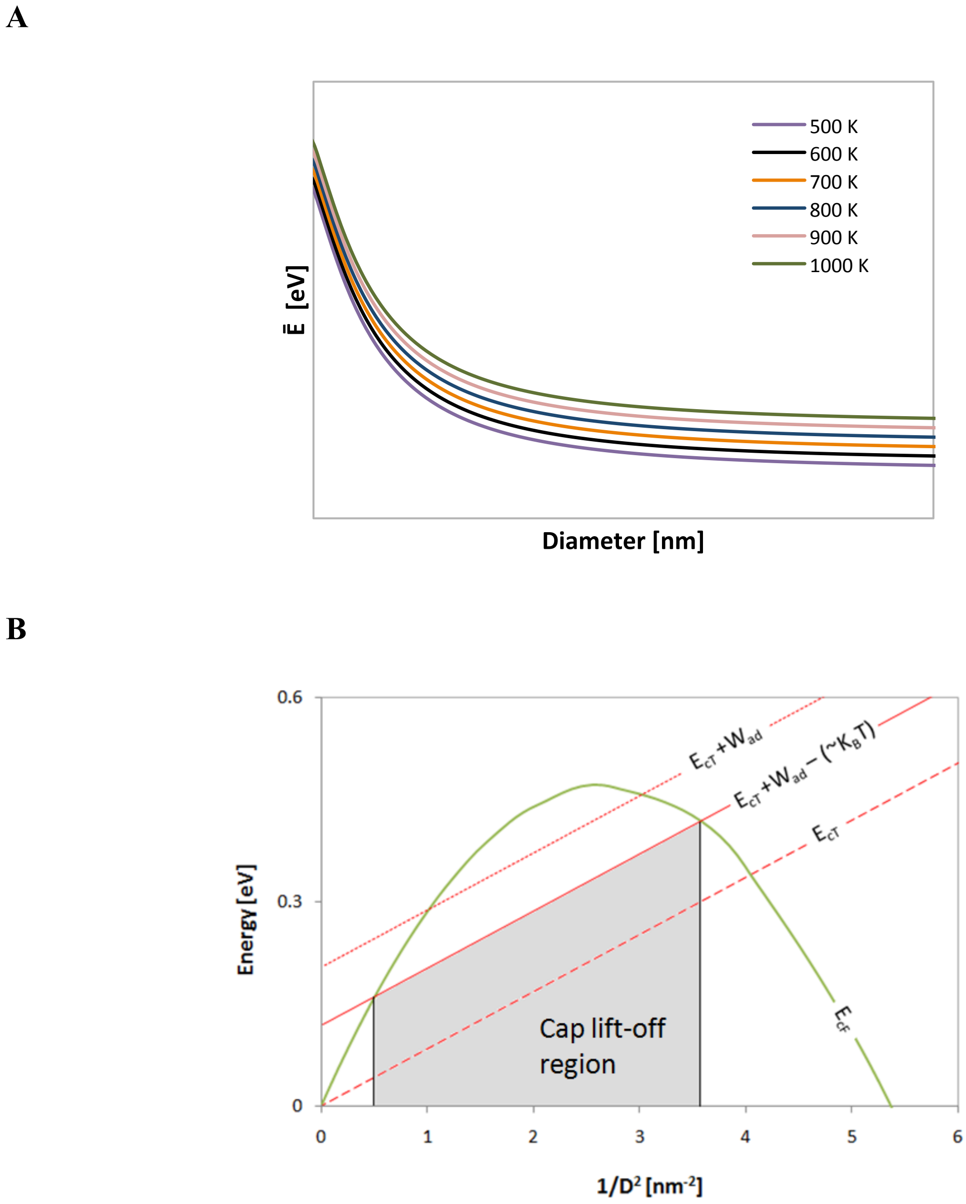

Figure 4.7. a) Transition limits between growth and encapsulation as a function of the temperature. Ē is calculated as Ē= $E_{cF} - E_{cT} + E_{K.}$ This suggests that if $W_{ad} < \bar{E}$ then cap-lift off will be observed, while if $W_{ad} > \bar{E}$ graphitic encapsulation will take place. Otherwise ($W_{ad} = \bar{E}$) will equal the probabilities of finding either growth or encapsulation. b) Curvature energies as function of $1/D^2$. Wad and $E_K \approx k_BT$ modify the slope of E_{cT} defining new intersection points with E_{cF} which represent limits between the encapsulation region and the growth region.

The growth zone is also defined as the interval of diameters where the curvature energies of the nanotubes (E_{CT}) are below those of the respective fullerenes of same diameter (E_{CF}) (Figure 4.7b). Thus, the work of adhesion and the thermal kinetic energy influence the curvature energy of the nanotubes E_{CT}, making it rise when W_{ad} is increased or decrease when the temperature is augmented. Therefore, W_{ad} and E_K define a new limit for the transition from the graphitic encapsulation zone to the cap lift-off zone (intersection with E_{CF}). It is evident from Figure 4.7b that the region of growth would be significantly reduced for catalysts with high W_{ad} and low temperatures. Although Figure 4.7 represents theoretical trends based entirely on the combination of two models separately proposed (curvature energy and kinetic model), our MD simulations have provided basis to conclude that curvature effects are as important as kinetic effects in the SWCNTs nucleation stage, despite the typical growth processes are non-equilibrium processes where the curvature effects may be thought as less relevant.

Theoretical values of W_{ad} have been reported for different transition metals. Adsorption energies of graphene on the (1 1 1) surfaces of Co, Ni and Cu have been calculated as 160, 125 and 33 meV/C, respectively.[88] Limited theoretical information is found for graphene deposited on Fe surfaces, principally because of the lattice mismatch that exists between surfaces cleaved from the BCC lattice of iron and the graphene lattice. However, non-periodic calculations of individual atoms and clusters allow us to approximate this interaction to a range of 150 and 240 meV/C.[89,90] Despite most of the reported experimental data do not match the exact growth conditions of our MD simulations, some floating catalyst CVD (FCCVD) experiments have demonstrated qualitative agreement with our data. Ferrocene is the most widely used catalyst precursor in FCCVD techniques.[91-93] Processes with growth conditions similar to our simulations parameters led to growth of SWCNTs with ~2.0 nm of maximum diameter.[91,92] The combination of this diameter with the W_{ad} range reported above for iron lie within the encapsulation zone in the Figure 4.6; the explanation for this discrepancy is related to the experimental reaction temperatures above 1200 K that favor the growth of large diameter SWCNT, as seen in the figure 4.7. Similarly, Co and Ni catalyst have led to the formation of SWCNTS with diameters up 2 nm and 3 nm, respectively;[94] which is expected since Ni has a weaker interaction with graphene compared to Fe and Co.

4.5 Conclusions

Analysis of the results from molecular dynamics simulations demonstrate that for a given catalyst (i.e., at fixed work of adhesion) and temperature, the size of the catalyst particle is quite decisive during the nucleation stage, driving the system toward encapsulation or nanotube growth. This is summarized in a work of adhesion vs. catalyst size phase diagram, defining a limit between SWCNT growth and catalyst encapsulation regions. Furthermore, it is suggested that this limit is given not only by thermal kinetic energy, but also by differences in curvature energies between ball-like fullerenes and nanotubes. To account for these findings, we propose a simple model which can be used to predict catalyst poisoning or growth based only on three variables, temperature, strength of interaction between carbon and the catalyst surface, and diameter of the catalytic particle.

5. EFFECT OF THE METAL-SUBSTRATE INTERACTION STRENGTH ON THE GROWTH OF SINGLE-WALLED CARBON NANOTUBES*

5.1 Summary

Single-walled carbon nanotubes are usually synthesized by catalytic growth driven by reaction of a precursor gas over metallic nanoparticles supported on a substrate. Here we use molecular dynamics simulations (MD) with the purpose of determining how the catalyst-substrate strength of adhesion influences the structure of the carbon networks synthesized on the catalyst surface. It is found that the strength of the catalyst/substrate interaction energies define the shape of the catalyst particle. When these energies are attractive, the nanocatalyst height decreases due to enhanced wetting, and in turn favors the lifting up of carbon nanotube caps during the synthesis process. In addition, the presence of an appropriate substrate may avoid catalyst poisoning. This effect may result from repulsion forces from the substrate toward catalyzed carbon atoms, which cause carbon atoms to diffuse to upper layers thus keeping the catalyst-substrate interface exposed to continuous catalytic activity. However, too strong metal-substrate interactions may take the cluster to the limit of complete wetting thus promoting the formation of graphene or amorphous carbon over carbon nanotube-like structures. A growth diagram is constructed in the space of metal-substrate vs. metal-carbon strengths of adhesion. The phase diagram defines regions of nanotube growth and encapsulation; in the first we are able to identify also zones of higher or lower quality of the nanotubes grown. This theoretical characterization is very useful to guide a controlled synthesis.

---

* Reprinted with permission from Juan C. Burgos, Erick Jones, and Perla B Balbuena. "Effect of the Metal−Substrate Interaction Strength on the Growth of Single-Walled Carbon Nanotubes." The Journal of Physical Chemistry C **115**(15): 7668-7675. Copyright 2011, American Chemical Society.

5.2 Introduction

The unusual properties of single walled carbon nanotubes (SWCNTs) have made them the focus of many investigations aiming to correlate their exceptional mechanical and electronic behavior to their structure[52,54,55]. Since the discovery of SWCNTs by Iijima in 1991[1], researchers have been actively involved in research tending to elucidate and explore their outstanding properties that make them potentially useful for numerous technological applications. Thus, in the last years, several processes have been proposed for mass production of high quality carbon nanotubes[10,57,58]. However, despite their refinements[59-61] and achievements[21,62] on the selectivity toward certain diameters and chiralities, none of them has reached complete control on the resulting structure of the synthesized nanotubes. Consequently, most of the processes result in a random mixture of single walled nanotubes with different chiralities, multi walled nanotubes, graphite and even amorphous carbon, which limits their technological applications since the separation methods can become difficult and expensive. Therefore, scientists have focused their efforts in studying the reasons that may favor selectivity in the catalytic process of synthesis of carbon nanotubes. In some cases these efforts have led to a high level of control over diameter and chirality,[13,63] which mostly define the tubes mechanical and electronic behavior. This research has shown that an appropriate management of process conditions such as temperature, pressure, catalyst composition and diameter, and substrate nature may direct the synthesis to the formation of SWCNTs over any other carbon species.

Although chemical vapor deposition (CVD) methods consisting on decomposition of carbon precursor compounds on the surface of metal catalyst nanoparticles are the most common techniques employed for producing SWCNTs, the process variables need to be carefully controlled in order to avoid catalyst poisoning and/or formation of undesirable carbon species. Even though the CVD initial stages have been analyzed through several experimental techniques such as transmission electron microscopy (TEM) and high resolution transition microscopy (HRTEM)[64,65], important details of these stages are still under discussion. In addition, theoretical works[95-97] have provided useful insights about the CVD catalytic process. It has been suggested that elemental carbon diffuses into the cluster until a high level of saturation is reached and the carbon atoms segregate toward the surface where they start to combine into forming carbon chains and rings. Theoretical and experimental research has identified this step within the process as critical for defining either lifting up of caps or encapsulation and catalyst poisoning. For instance, Hafner and Smalley[71] defined the probabilities of finding encapsulation or growth as an energetic competition between curvatures of nanotubes and spherical fullerenes of same diameter. Furthermore, they introduced the strength of adhesion (W_{ad}) between graphene nucleated on the catalyst and metallic catalyst surfaces as an important factor capable of unbalancing the close competition between curvature energies of nanotubes and spherical fullerenes. Thus, Hafner and Smalley's model proposes that in order to observe the growth of a SWCNT, its curvature energy must be overcome by the combined action of W_{ad} and the curvature energy of a spherical fullerene of the same diameter. On the other hand, Kanzow et al[67,68] analyzed the graphitic encapsulation from a kinetic point of view. They established that enough kinetic energy is required to observe cap lifting up and later growth, which will always be observed as long as the energy of adhesion (W_{ad}) does not overcome the kinetic energy at the substrate-catalyst interface, which can be represented through the following condition:

$$E_{kin} > W_{ad} \tag{5.1}$$

Where the kinetic energy is a function of temperature approximated by $\sim k_B T$. Ribas et al[98] corroborated this theory using molecular dynamics simulations. They were able to find out the transition from encapsulation to growth on a two dimensional W_{ad} vs T diagram, and thus, to quantify the amount of kinetic energy required for lifting the graphene layer off from the cluster. Other theoretical works have also agreed with the curvature and kinetic theories, although the kinetic model is by far the most accepted due to failures of the curvature model when considering clusters deposited on substrates and neglecting kinetic effects. We recently suggested that the curvature model should not be completely neglected; [99] on the contrary, both theories can become complementary merging into a simplified combined model. Thus, a new model was proposed with the kinetic energy and energy of adhesion (W_{ad}) as unbalancing factors on the competition of curvature energies of nanotubes and spherical fullerenes. However, none of these individual models (curvature and kinetic), nor the combined, are able to predict the conditions at which the nanotubes are capable to grow when the catalyst particle is deposited on a substrate.

Several investigations have been carried out trying to analyze the influence of the substrate during the synthesis process. For instance, Ward et al[100] characterized several silicon containing substrates, as well as alumina and magnesium oxide structures, finding a correspondence between the type of substrate employed as support and the selectivity toward the formation of SWCNTs over MWCNT's. On the other hand, Li et al suggested that the substrate-particle binding force might influence the activity of the catalyst particle. They argue that the nature of the interaction defines the geometry of the catalyst, which in turn determines the carbon concentration profiles within the catalyst particle, and therefore, the orientation of carbon structures nucleated on the catalyst surface.[101] Other studies have also analyzed the influence of the substrate on the shape of catalytic particles.[102]

This work aims to develop a better understanding of the role of the substrate on determining catalyst encapsulation or cap lifting up, and about its influence on the structure of the synthesized carbon species. Despite graphite encapsulated metal particles have shown exceptional magnetic properties, and therefore, potentially useful for technological applications, in the SWCNT synthesis they are considered undesirable products. Thus, unlike previous works studying floating catalyst systems, molecular dynamics simulations are employed here with the purpose of clarifying details related to the presence of the substrate such as its influence on the catalyst geometry, and its role avoiding graphitic encapsulation, therefore facilitating the formation of SWCNTs instead of any other kind of carbon structure.

5.3 Computational model and force field details

The growth of single walled carbon nanotubes is studied by molecular dynamics simulations through a set of force fields describing the principal atomic interactions involved during SWCNTs nucleation and growth processes. The system over which the simulations were carried out consists of a periodic orthorhombic box with a rectangular base 25.565 Å wide (x direction) and 22.140 Å deep (y direction). The periodic box was set to be 84 Å high (z direction) which provides a high enough height capable of covering relatively long nanotube growths, as shown in Figure 5.1. The density of the precursor carbon atoms in the box was set to 0.0001 molecules/$Å^3$ and the temperature to 1000K with the purpose of emulating as close as possible real synthesis conditions.[21,62] Thus, under these pressure and temperature conditions and with the volume provided by the box dimensions, C-containing molecules are randomly introduced in the simulation box facilitating the catalytic process via frequent collisions between the precursor atoms and the metal atoms. An FCC metallic catalyst, formed by thirty two atoms arranged in a quasi-spherical shape with mainly 111 facets exposed, is placed at the bottom of the simulation box and deposited on a model substrate represented by a graphene sheet (Figure 5.1). We employ a Ni_{32} cluster herein because it has been shown in our previous studies[99] that this cluster size leads to the formation of SWCNTs of ~ 1 nm of diameter which is approximately the diameter of the nanotubes (9,1), (6,5) and (7,5). These are the most produced SWCNTs in the CoMoCAT process,[103] considered as one of the most effective in achieving diameter and chirality selectivity.

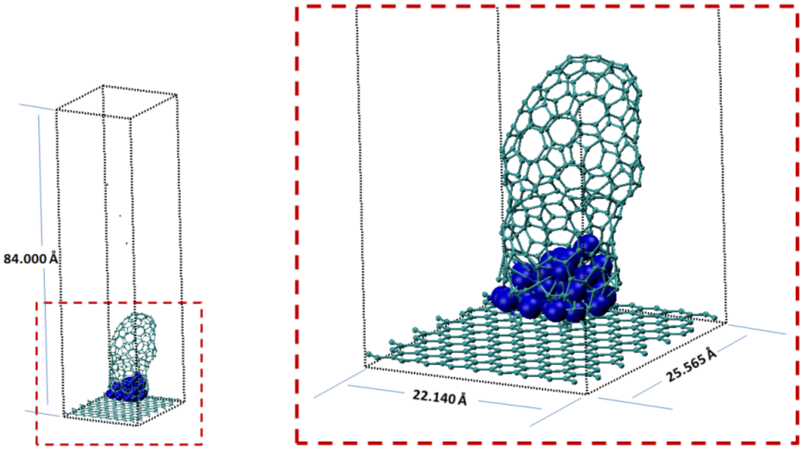

Figure 5.1. Scheme of the periodic box of the system depicting the catalyst, substrate, and growing nanotube.

Three main interactions can be easily identified in the growth process. Metal-metal interactions are described by the well known many-body Sutton-Chen potential[38] which has been successfully employed to describe several properties of transition metals. In addition, carbon-carbon interactions are characterized through a modified potential[104] inspired on the second-generation reactive empirical bond order (REBO) potential developed by Brenner[39], which is known to describe the main carbon phases such as diamond and graphite and the transformations between them. Metal-carbon interactions can be classified into three different categories according to the states of the carbon and metal atoms involved in the interaction. All of them are represented by the same reactive potential developed by Martinez Limia et al[104], that is based on the Tersoff-Brenner scheme, but parameterized in such a way that the potential is able to differentiate among states of the carbon atom, including its position relative to the metal atoms, its hybridization state, and its role in the system. This means that the potential is capable to distinguish whether carbon is part of the substrate graphene, or a catalyzed active carbon located inside or on the surface of the catalytic metal cluster. Taking advantage of this wide parameterization, we were able to represent the effect of different catalysts that interplay dissimilarly with the substrate and the catalyzed carbon. The interaction energies between *metal and carbon atoms* with sp2 hybridization were precisely controlled and set to eleven desirable values in the range 160-560 meV. This was possible through the manipulation of a parameter that balances the attractive and repulsive components of the *metal-carbon* force field, as done by Ribas et al[98]. The metal-carbon interactions of systems relevant for synthesis of SWCNTs are close to the lower limit of this range of values. For example, Ni/graphene and Co/graphene systems were reported to have 125 and 160 meV of interaction respectively[88], whereas Fe/graphene also approximates this range since Fe is found to bind carbon atoms as strong as Co and Ni do.[105] The *metal-substrate* energies were controlled manipulating a different parameter, setting thirteen values between 160 and 925 meV. This range of values agrees with some values reported in the literature for metallic clusters adsorbing on ceramic substrates. Our lowest interaction is comparable to that of the Ag/MgO[106] system which lies within the range 143 - 399 meV, whereas other metal-substrate interactions, such as, Cu/MgO (360 meV)[107], Ni/MgO (620 meV)[107] and Co/SrTiO$_3$ (2470 meV)[108] are in the higher range of our metal-substrate interaction values. The integration of the equations of motion was performed by the predictor-corrector algorithm with a time step of 0.5 fs. The total time of the simulation was set to 10 ns approximately, that represents a reasonable time to register any cap lifting up for the catalyst size used in this study. The thermodynamic state of the system is statistically defined by means of the thermodynamic ensemble where the total number of particles is allowed to change, whereas the temperature and volume are kept fixed.

Despite the correct representation of several physical phenomena taking place during nucleation and initial stages of SWCNTs growth, our MD simulations are based on some approximations that limit the accuracy of the emulated synthesis process. The simplified approach taken for the disproportionation of carbon precursor molecules, the neglect of the effect of other species, such as hydrogen, water, and reaction intermediates that may interact with the catalyst surface and catalyst-substrate interface, and the artificial acceleration of the reaction process driven by the need of having accessible simulation times, are among of the principal constraints of our MD simulations. Nonetheless, our realistic modeling of the most important atomic interactions involved in the synthesis process, provide close insights over reaction pathways at nucleation and initial stages of growth, where many structural features start to be forged. A better understanding of these initial stages is thought to be the key of the diameter and chirality control during the growth of SWCNTs.

5.4 Metal carbon interactions and the cluster shape

The first step in the analysis of the complete synthesis process of SWCNTs on substrates is to investigate the pretreatment of the catalyst, including heat treatment, adsorption on the substrate and final atomic arrangement of the catalyst. As mentioned in previous studies,[109] the shape and diameter of metal cluster employed as catalyst may determine the structure of the tube nucleated on it, and therefore its physical properties. Although here we use a predetermined initial configuration of the catalyst that is deposited on the substrate, other variables such as the kinetic energy, the substrate geometry, and the strength of the metal-substrate interactions will influence the instantaneous configuration of the catalyst particle during SWCNT growth. The substrate structure defines the most likely adsorption sites of the atoms at the bottom layer of the metal cluster. In this study, we have used a model graphene substrate, and we have varied the interaction strength with the metal atoms to represent variable substrates. As seen in Figure 5.2a, the metal atoms in direct contact with the substrate adsorb on the center of the hexagons in the honeycomb lattice, and the total number of metal atoms directly attached to the model graphene substrate depends on the strength of the metal-substrate adsorption energies. Furthermore, the force of adhesion between catalyst and substrate determines the height of the cluster respect to the substrate plane; which is given by the number of layers and number of atoms per layer of the catalyst particle. The results are summarized in the z-density profile shown in Figure 5.2b, where there is no carbon addition. Thus, strong metal-substrate interactions induce the cluster to keep its 3-D structure, which is represented by the three peaks in the z-density profile.

However, as the strength of adhesion between metal and substrate increases, the metal atoms in the upper layers start to diffuse toward lower layers spreading over the surface. The kinetic energy and the strong attraction undergone by the metal atoms and the substrate become the driving forces for the solid-solid wetting transformation of the 3-D cluster structures into single layers. In the z-density profile reported in Figure 5.2b, this phenomenon is evident in the height reduction and in the vanishing of the peaks corresponding to the upper layers.

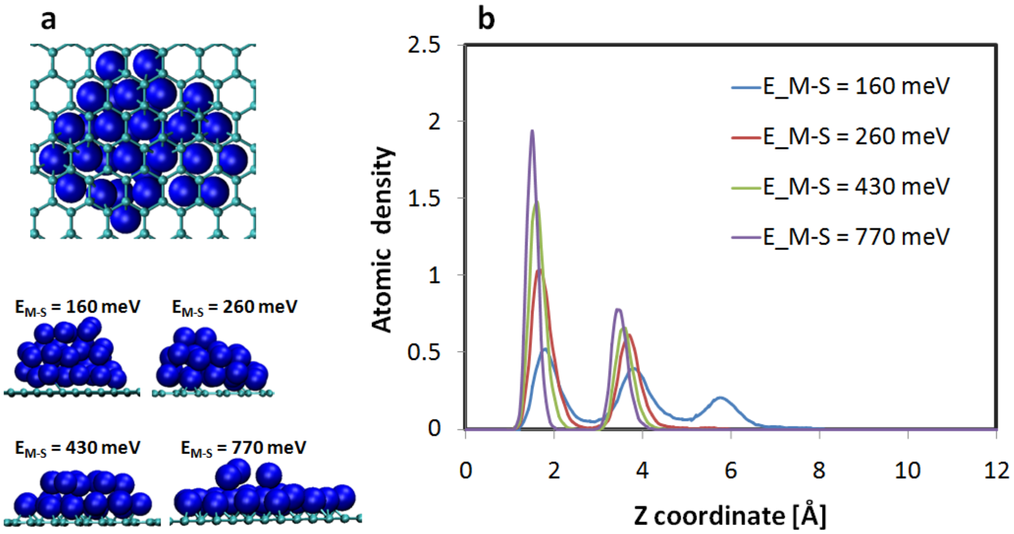

Figure 5.2. (a) Structure of the metal cluster over a model graphene-like substrate for various metal-substrate interactions in the absence of carbon addition. (b) Density profile of the cluster metal atoms calculated in the direction perpendicular to the substrate.

On the other hand, during growth of SWCNTs, other factors start to gain relevance in the structural conformation of the catalyst particle. Since carbon species are added to the system during the simulated synthesis process and irreversible catalysis is assumed, catalyzed carbon atoms are easily accommodated in the interstitial sites of the catalyst, reducing the kinetic energy effects by restricting the metal atoms mobility.

Moreover, the diffusion of carbon atoms towards the surface and later formation of carbon networks introduce an additional energetic variable counteracting the affinity of metal atoms with the substrate. Under these conditions metal atoms, particularly those located at upper layers, will undergo opposite forces along the z coordinate which will mainly define the catalyst shape and location relative to the substrate. Thus, if the metal-substrate interaction is weak enough, metal atoms at the top of the catalyst will remain in their locations interacting with graphene structures synthesized on the cluster surface. On the other hand, if the metal-substrate interaction is sufficiently strong, the metal atoms at the top of the catalyst will prefer to diffuse toward the substrate despite the decrease of mobility caused by the presence of single carbon atoms and carbon chains formed inside the catalyst particle. In consequence, the height of the catalyst particle is now a function of an energetic competition between metal-substrate and metal-carbon interactions. However, the effect of the carbon graphene-like structures on the catalyst surface becomes relevant at later growth stages. These features can be observed through analysis of z-density profiles (Figure 5.3) at different stages of the simulation for all the $E_{M\text{-}S}$ analyzed above in Figure 5.2.

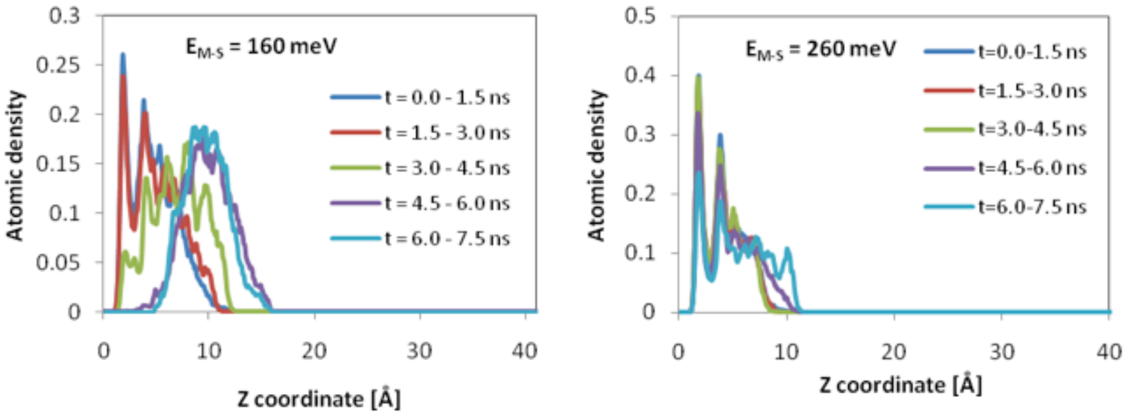

Figure 5.3. z-density profiles of the metal atoms in the cluster at various metal-substrate interaction strengths, and at several growth stages (indicated by the times in nanoseconds).

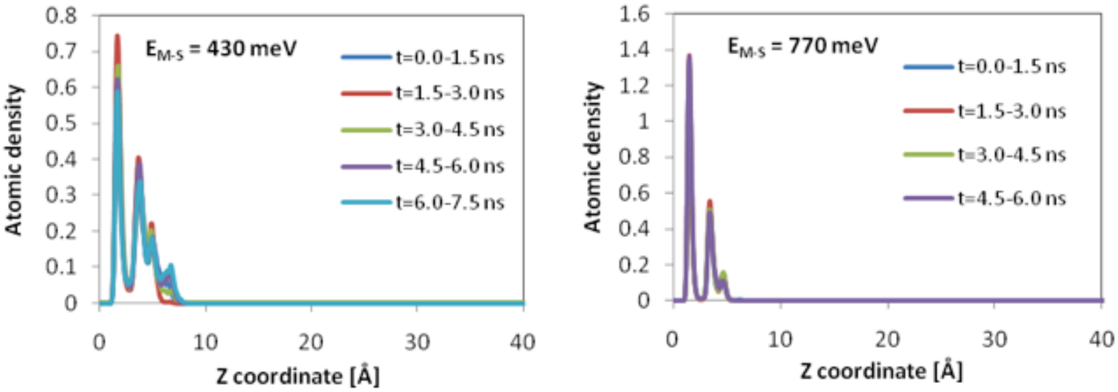

Figure 5.3. Continued.

Figure 5.3 shows clearly that at the very beginning of the synthesis process (before 3 ns of simulation) the metal atoms remain attached to the substrate and keep their positions around the initial configuration. At this point carbon structures have not yet nucleated on the catalyst surface and there is no driving force trying to pull the metal cluster along the z direction. As soon as the carbon structures are produced on the catalyst surface (after 3 ns), at low metal-substrate energies of adhesion, the carbon structures start to pull the metal atoms upwards, and even occasionally separate the whole cluster from the substrate surface; this fact is represented by the peaks around 10 Å and the absence of peaks below 5 Å observed in the z density profile obtained at the lowest metal-substrate energy of adhesion ($E_{M-S} = 160\ meV$). On the other hand, for substrates with strong metal-substrate adhesion the catalyst structure remains intact during growth.

As the metal-substrate adhesion increases, not only the catalyst height and volume are reduced, but also the amount of interstitial sites available for diffusion of carbon atoms. This event is reflected by the reduction of the number of carbon atoms inside the catalyst as depicted in Figure 5.4, where the number of carbon atoms inside the cluster drops suddenly to zero when the cluster spreads completely over the substrate. Thus, the decrease of the available interstitial sites in addition to the rigidity gained by the catalyst may reduce the rate of carbon diffusion into the cluster.

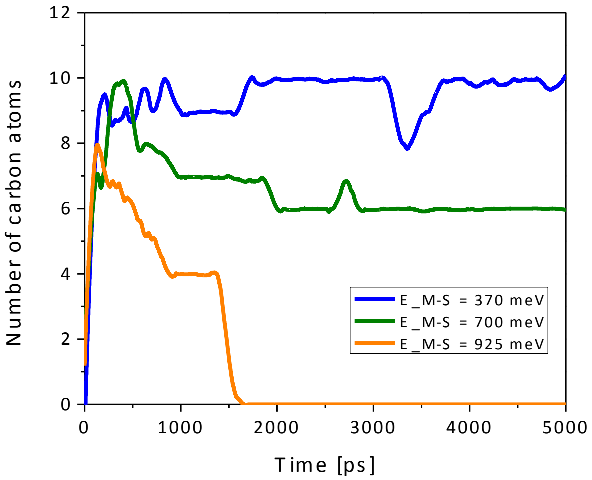

Figure 5.4. Number of carbon atoms inside the metal cluster as a function of time for various metal-substrate interactions.

5.5 Cap lift off vs. graphitic encapsulation

Catalyst encapsulation or growth is also influenced by the action of the substrate. Previous works have concluded that weak adhesion of the carbon structures to the catalyst, high temperatures, fast diffusion of carbon atoms into the cluster, and small catalyst particles are absolutely essential for the growth of SWCNTs on floating catalysts.[67,68,71,98,99] However, our current results confirm that the presence of a substrate induces variations to this growth vs. encapsulation behavior. For instance, carbon structures produced at 1000K on floating Ni_{32} encapsulated catalyst particles when the energy of adhesion to the metallic cluster was as high as 160 meV.[99] On the other hand, the situation becomes favorable for caps lifting off and growth if a substrate that interplays strongly with the catalyst particle is employed for carrying out the reaction.

The behavior shown in the z-density profiles of Figure 5.3 is supported by snapshots taken for the highest and lowest energy of adhesion in Figure 5.5. If the metallic cluster is not strongly attracted to the substrate ($E_{M\text{-}S}$ = *160 meV* in Figure 5.5), the cluster becomes completely separated from the substrate and the growth vs. encapsulation behavior is governed by the existing theories for floating catalysts. Snapshots in Figure 5.5 reveal that clusters strongly attached to the substrate ($E_{M\text{-}S}$ = *925 meV*) will favor the cap lifting off rather than leading to graphitic encapsulation. During the first steps of the reaction, carbon networks begin to be formed on the surface. As soon as this structure covers most of the top surface, it starts exerting a force that pulls the catalyst atoms stretching the metal cluster along the z direction. The continuous catalysis process occurring at the cap-catalyst-substrate interface leads to growing of a cap and performs an even stronger tensile force over the catalyst. However, the catalyst is also under an opposite tensile force from the substrate trying to keep the metallic cluster adhered to the support. Thus, if the catalyst-substrate force of adhesion is quite strong, it will induce weakening of the metal-carbon cap bonds thus favoring the catalyst to remain attached to the support. At this point, the cap lifts off starting CNT growth. Furthermore, extremely strong metal-substrate interactions ($E_{M\text{-}S}$ = *925 meV*) lead the catalyst atoms to overcome their self cohesion energy and induce their spreading on the substrate surface becoming a monolayer thin film that wets the support. Consequently, a larger number of atoms located at the cap-catalyst/substrate interface (Figure 5.5) are always available for catalytic activity. This increases the probability of carbon conversion that facilitates the cap lifting off.

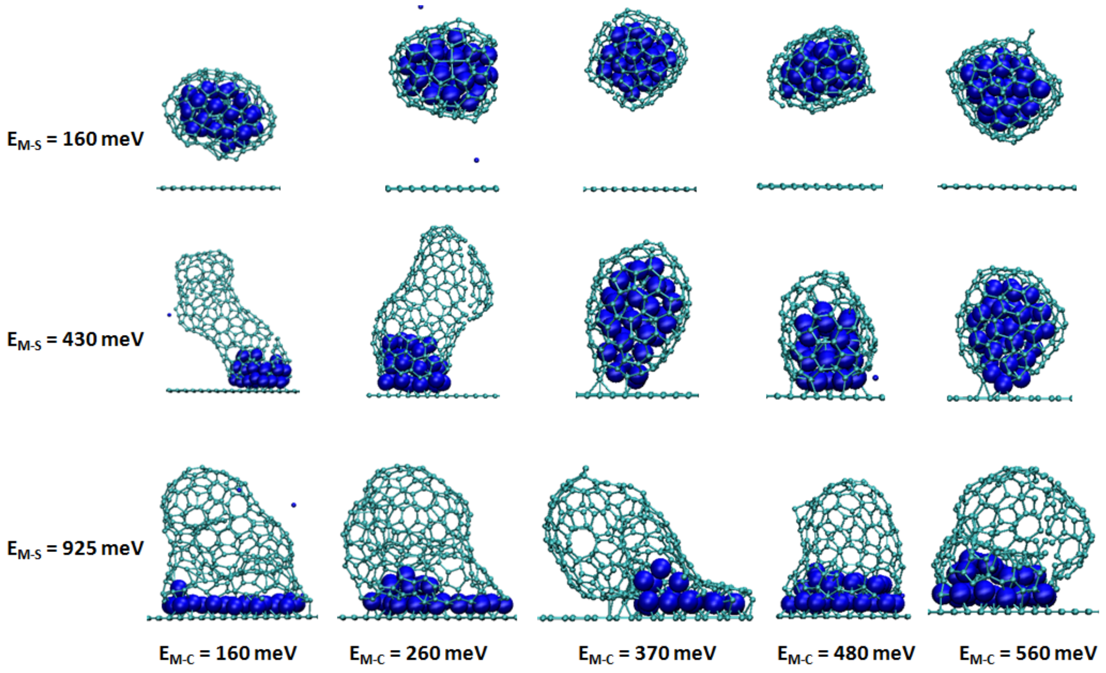

Figure 5.5. Snapshots of the catalyst structure and carbon species simulated at various E_{M-S} catalyst-substrate interactions, and at several E_{M-C} catalyst-carbon energy of adhesion.

On the other hand, in the limit of weakest metal substrate interaction (E_{M-S} = *160 meV*), the substrate is incapable of maintaining the metal particle attached, and the force exerted by the graphene cap gains pulling off the entire catalyst particle (Figure 5.5). The substrate in that case does not contribute to avoid encapsulations at all, since the catalyst particle is now floating at a considerable height from the support and the forces acting over the catalyst from the substrate can be neglected. In this limiting scenario, all the theories mentioned above for prediction of growth/encapsulation for catalyst floating in gas phase apply. Interestingly, a substrate with an intermediate energy of adhesion to the catalyst will boost the growth only in case of low metal-carbon work of adhesion as shown in Figure 5.5 (E_{M-S} = *430 meV*) where a transition from growth to encapsulation can be easily identified in the range 260 – 370 meV. Within this range, the forces contributing to growth and encapsulation become equated and only small perturbations to the relevant process variables can determine whether a cap will lift off or not. For instance, for a catalyst with 430 meV of adhesion to substrate and 480 meV of adhesion to carbon, formation of a small cap can be observed even though the metal-carbon energy is far from the transition range defined by the equilibrium of the metal-carbon energy in conjunction with the metal-substrate and kinetic energies. This can be explained based on the fact that although at these conditions the cluster remains attached to the substrate with a few metal atoms, the number of atoms at the interface is larger than in the two other cases. This difference may result in a slightly higher catalytic rate which increases the pulling force ending in cap formation.

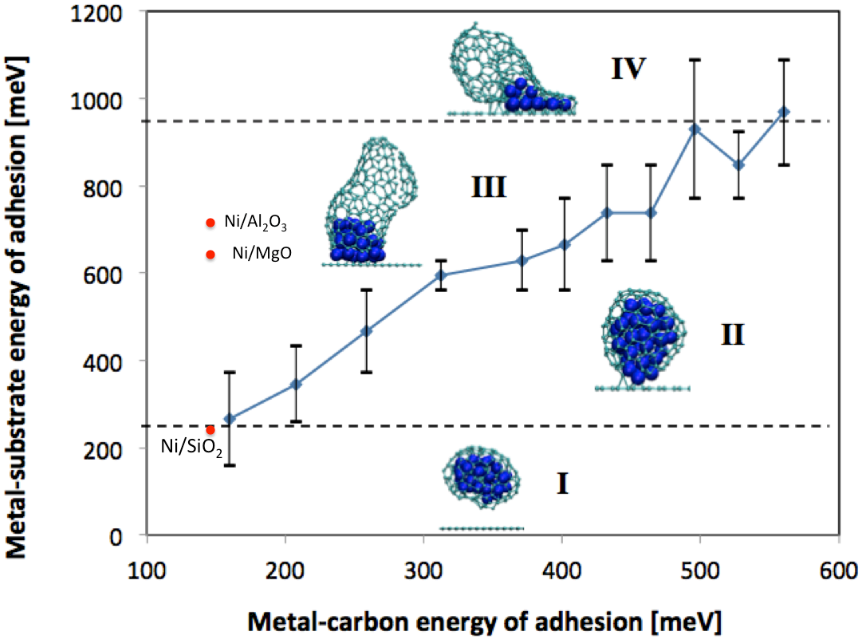

Figure 5.6. Growth diagram of growth vs. encapsulation as function of the catalyst-substrate and catalyst-carbon interaction strengths. The blue curve delimits the transition from encapsulation to growth and the top and bottom dashed lines separate two growth zones and two different encapsulation zones respectively.

In order to find the location of the transition ranges more precisely, simulations at eleven different metal-carbon energies of adhesion in the range 160-560 meV were carried out. For each value of metal-carbon interaction, simulations for thirteen different metal-substrate energies within the range 160-1088 meV were performed, and the whole set of simulations were repeated five times with the purpose of developing a statistical analysis. The results summarized in Figure 5.6 show a general trend of growth at high metal-substrate interactions and at low metal-carbon works of adhesion. The transition from growth to encapsulation is delimited by the blue curve in Figure 5.6, whereas the vertical black lines represent uncertainty intervals where growth or encapsulation is not well defined since near these conditions the resultant force acting at the catalyst-cap interface approaches to zero and any small perturbation made to the system may unbalance the equilibrium favoring either encapsulation or growth.

Additionally, four zones can be identified in the growth diagram plotted in Figure 5.6. The first zone located at the lowest metal-substrate interactions (below the bottom dashed line) corresponds to the states where the fullerene caps are able to pull off the catalyst from the substrate. At higher catalyst adhesions to the substrate, above the bottom dashed line but below the blue curve, there is a second encapsulation zone. Within this zone the graphitic caps are incapable of pulling off the catalyst, however the cap itself is also incapable of lifting off from the catalyst since the combined action of the kinetic energy and the effect of the substrate are not strong enough to overcome the metal-carbon energy of adhesion. If the catalyst adhesion to the support is stronger than that defined by limit of encapsulation (blue curve), the first zone of growth is found (region III), where the attraction experienced by the catalyst atoms is enough to break the cap-catalyst adhesion, allowing the cap to be released from the catalyst surface; however, that attraction is not high enough to spread the catalyst on the substrate, which let the carbons atoms in the nanotube sidewalls to adsorb on the hollow sites of the FCC (111) surfaces of the metallic cluster, allowing in such a way the formation of high quality and less defective SWCNTs. At extremely high adhesion catalyst adhesion to the substrate, above the limit demarked by the top dashed line, a second region of growth appears. At these conditions, the catalyst atoms try to maximize the contact area with the substrate reducing the cluster to a thin film and avoiding the contact with carbon atoms in the fullerene cap sidewalls. Under these circumstances, the epitaxy of the process is eliminated and complex carbon structures can be synthesized, such as, graphite, amorphous carbon, double walled carbon nanotubes, or large diameter SWCNTs but highly defective.

In addition to the values reported in the section 5.3 for different metal-substrate adhesion energies, other well known catalytic systems have been reported to be within our metal/support energy range. Ni/SiO_2 and Ni/Al_2O_3 systems have been found to interact at 229 [110] and 710 meV,[111] respectively. These values, along with the values reported for Ni/MgO, lie within the zone III of the chart (Figure 5.6) identified as the zone of quality growth, taking into account the weak W_{ad} between Ni and carbon (125 meV).[88] Thus, it is not unexpected that these catalytic systems have been extensively used to grow SWCNTs obtaining extraordinary results regarding quality and even selectivity.[112-116] On the other hand, cobalt adsorbing at 2.47 eV on $SrTiO_3$ will undoubtedly classify in the zone IV, zone of low quality nanotubes. This explains the absence of experimental data reporting synthesis of SWCNTs from this catalyst. Finally, values reported in the section 5.3 for metal/graphene adhesion[88] for Co, Ni, and Cu demonstrate that graphene is not a good candidate to support transition metal catalysts. Our MD simulations predict that a graphene support will not be able to hold a catalyst close to its surface, and the curvature energy model described in the previous chapter will govern the growth or encapsulation. Limited or no growth of SWCNTs on graphene-supported catalysts has been found up to date.

Unlike the synthesis of SWCNTs on floating catalysts where high diameter particles hinder the growth of SWCNTs,[71,99] it was demonstrated here that when the metal-substrate adhesion is strong the cluster tries to maximize its diameter and this scenario contributes to the lifting off of caps. These results corroborate that the curvature energy models do not apply when the catalyst is supported on a substrate. However, no matter if the growth is carried out in gas phase or on a substrate, the kinetic energy at the catalyst-cap interface will still play an important role on the fullerene caps lifting off. Therefore, we propose here a growth vs. encapsulation model based on the kinetic model mentioned previously (equation 5.1) and taking into account the metal-substrate strength of adhesion ($E_{M\text{-}C}$) for the growth condition.

$$E_{kin} + h*E_{M\text{-}S} > E_{M\text{-}C} \tag{5.2}$$

Metal atoms at the cluster's top surface, which are in direct contact with the cap, are the ones called to govern the growth or encapsulation according to the strength of attraction experienced from the substrate. Nonetheless, these atoms are not those in the range of the equilibrium binding distance with the substrate film. Therefore, it is probable that only a fraction of the metal-substrate adhesion energy ($E_{M\text{-}S}$) represents the real contribution to the kinetic energy on boosting growth over encapsulation. In consequence, a factor (h) must be introduced in equation (5.2) with the purpose of weighting $E_{M\text{-}S}$ according to the cluster height. The weight factor is a real number lying within the range 0-1 defined by the two limiting cases corresponding to the regions I and IV respectively, in the growth diagram of Figure 5.6.

5.6 Conclusions

Molecular dynamics simulations were carried out to investigate growth of carbon nanotubes on catalysts supported on a substrate. The results reveal that the substrate nature and level of interaction with the catalyst have a strong influence on the catalyst structure, and therefore on the structure of the produced carbon species. Z-density profiles demonstrate that the catalyst atoms arrange not only according to the metal-substrate level of adhesion, but also they are influenced by the interaction with the growing carbon networks that counteracts the effect of the metal-substrate adhesion. A growth diagram was found product of a statistical analysis from several simulations. Four main regions were identified, two encapsulation regions at low metal-substrate energy of adhesion and high metal-carbon interactions; and two growth regions, one of high quality SWCNTs at relatively high $E_{M\text{-}S}$, and other of more complex carbon species at extremely high $E_{M\text{-}S}$. Finally, a new model was proposed for the growth condition based on the kinetic energy model but including the term $E_{M\text{-}S}$ weighted by a variable that is a function of the cluster height.

6. DYNAMICS OF TOPOLOGICAL DEFECTS IN SINGLE-WALLED CARBON NANOTUBES[*]

6.1 Summary

Nucleation and healing of structural defects in single-walled carbon nanotubes (SWCNTs) studied through reactive molecular dynamics simulations (RMD) and RMD trajectories reveal formation and healing mechanisms of various topological defects on the catalyst surface. A quality percentage of nanotubes is measured by calculating the relative amount of hexagons per carbon atom relative to the same quantity for a perfect nanotube of the same length. Following this approach, the concentration of defects is estimated for nanotubes grown on catalysts with different sizes and morphologies, and for various temperatures and gas phase densities. From this analysis, we identify specific catalyst morphologies that favor the growth of SWCNTs with low defect concentration. Vacancies, 5-7 and Stone-Wales defects are observed to nucleate distinctly in the tubes depending on the catalyst morphology. We find that a strong interaction between the catalyst surface and the graphitic lattice of the nanotube is absolutely necessary for healing and formation of defects. Our study suggests that defects can be healed independently of the degree of embedment of the defective structure into the tube structure. Diffusion and catalytic events at the catalyst/tube interface are the main sources of nanotube structural recovery on the catalyst surface. Finally, optimal growth conditions are identified that allow significant structural healing in nanotubes.

6.2 Introduction

The discovery of carbon nanotubes in 1991 by IIjima[1] unleashed a great deal of research aiming to characterize their structure, properties, and structure/property relationships [2-4]. Both multi-walled and single-walled carbon nanotubes (SWCNTs)

---

[*] Reprinted with permission from Juan C. Burgos, Erick Jones, and Perla B Balbuena. "Dynamics of Topological Defects in Single-Walled Carbon Nanotubes during Catalytic Growth." The Journal of Physical Chemistry C **118**(9): 4808-4817. Copyright 2014, American Chemical Society.

exhibit excellent mechanical, electronic, and optical properties that lead this novel material to meet performance standards required for various technological applications.[7,117] Nevertheless, most of the outstanding properties of SWCNTs have been theoretically calculated assuming absence of topological defects along the nanotube lattice. However it is thermodynamically unrealistic to assume perfection in nanotubes structure given the high temperatures at which the synthesis takes place and constant shifts from equilibrium due to addition of carbon feedstock.[118] Despite the impressive development and optimization of catalytic chemical vapor deposition (CVD) processes aiming to produce defect free nanotubes,[119,120] imperfections will constantly nucleate and are stabilized on the nanotube structure as a consequence of the reaction conditions.[118]

The structural quality of SWCNTs may be assessed in terms of the concentration of six-membered rings (hexagons) along the nanotube sidewall. Pentagonal rings arising due to curvature effects at the nanotube tip are usually nucleated at the first stages of growth as the nascent carbon structure adapts to the rounded shape of the catalyst particle forming an initial cap. Once the cap has lifted off, the nanotube growth continues by carbon incorporation at the cap rim, which results into continuous formation of hexagons at the nanotube edge.[99] However, at temperature and pressure growth conditions hexagon formation is not always thermodynamically favored, and pentagons, heptagons, and larger carbon rings are formed as a result of carbon mobility and despite the high strength of the graphitic sp2 carbon bond. Vacancies and bond rotations have been identified as the principal source of imperfections in SWCNTs.[121,122] The presence of each of them is generally associated to particular arrangements of stable non-hexagon carbon rings. Mono-vacancies and di-vacancies result from removing one and two carbon atoms from the crystalline lattice of the nanotube, respectively. As a result of this carbon removal, carbon-carbon bonds are broken leaving unstable dangling bonds that induce restructuration of the nanotube lattice favoring the formation of strained pentagons in the nanotube wall.[123] Two neighbor interacting vacancies result in nucleation of a di-vacancy.[122] Recombination of low coordinated carbon atoms resulting from di-vacancies eliminates all dangling bonds in the lattice by nucleating two isolated pentagons separated by an octagon.[124] Unlike di-vacancies, mono-vacancies usually leave a low coordinated carbon atom as a part of an eight-membered ring separating two pentagons. On the other hand, bond rotations are slightly energetically favored over formation of point defects such as vacancies and di-vacancies. Lattice transformation resulting from a 90 degrees rotation of a carbon-carbon bond facilitates the nucleation of two pentagons and two heptagons conjugated in a 5-7-7-5 arrangement known as the Stone-Wales (SW) defect.[125] Pentagon-heptagon isolated hybrids can be also nucleated in replacement of two adjacent hexagons of the nanotube wall generating a 5-7 defect.[122] Unlike SW defects, the 5-7 introduces misorientation in neighbor hexagons and the whole lattice, altering properties that depend on the helicity of the nanotubes.[121,122,126]

Although extensive experimental and theoretical studies have determined energetics and elucidated mechanisms related to defects formation, there is limited information about the role of the catalyst nanoparticle on nucleation and healing of these defects during growth. Using density functional theory (DFT), Ding demonstrated that SW and vacancy defects become more stable as they approach the open end of the nanotube.[127] Therefore a feasible mechanism would require defect diffusion toward the open end. However, this study neglected the presence of the catalyst and its possible effect stabilizing the defect. Ding and coworkers later demonstrated that pentagons, heptagons and 5-7 pairs could be efficiently healed on catalyst surfaces through bond rotations and carbon additions at the nanotube rim.[128] Through the calculation of energy barriers for defect healing at different positions relative to the growth front, these authors concluded that healing topological defects becomes impossible once they get embedded into the SWCNT structure.[128] Though using equilibrium thermodynamics the authors calculated the defect concentration on catalyst surfaces at different growth conditions (temperature, growth rate), their study neglected the effect of carbon bulk diffusion and segregation on defect healing. Similarly, Zhang et al used RMD simulations to identify reaction pathways for self-healing mechanisms in absence of catalyst.[129] They demonstrated that vacancy defects are quite unstable and therefore susceptible to be annealed through different mechanisms that include recombination of dangling bonds.

The absence of catalyst in the simulations required temperatures in the order of 1500K in order to break C-C bonds and facilitate annealing via surface reconstruction. However, this temperature is slightly above typical growth temperatures used in CVD synthesis. Morokuma and coworkers found out that reducing the carbon supply rate minimizes the defect concentration by enhancing free carbon surface diffusion on the catalyst surface.[118,130] Nonetheless, their cap-catalyst complex model disregarded the continuous carbon diffusion/precipitation taking place during cap nucleation and its possible implication in the healing of defects. Morokuma and coworkers were able to demonstrate the importance of low growth rates on defects healing, although they did not establish the requirement of a catalyst for the healing process to occur.[118] In contrast to previous studies, we analyze results from classical RMD simulations aiming to understand the role of the catalyst surface on defect healing under *more realistic reaction conditions*. The catalyst shape is tuned through various catalyst/support interactions in order to consider effects of net exposed catalyst surface as well as those of bulk and surface carbon diffusion. We evaluate the effects of temperature and growth rate on defect concentration and elucidate defect formation and healing mechanisms during nanotube growth on catalyst surfaces.

6.3 Computational details

RMD simulations are carried out in a periodic orthorhombic box with a rectangular base 39.824 Å wide (x direction) and 38.799 Å deep (y direction). The periodic box was set to be 84 Å high (z direction), which provides a high enough height for covering the growth of relatively long (up to 6 nm) SWCNTs. The temperature of the system is set to 1000K, whereas pressures between 2 and 8 atmospheres are used with the purpose of emulating as close as possible real CVD synthesis conditions.[12,21] These pressures are given by C-containing molecules randomly introduced in the simulation box and the catalytic process takes place via frequent collisions between the precursor atoms and the metal atoms. Nickel catalyst nanoparticles (Ni_{32} to Ni_{160}) initially of quasi-spherical shape are placed at the bottom of the simulation box over a substrate model represented by a single graphite sheet. It has been reported in our previous studies[99] that catalyst particles within this range of sizes lead to nucleation of SWCNTs of 0.8 – 1.8 nm diameters. This is approximately the diameter distribution range of nanotubes produced by highly selective CVD synthesis techniques. [12-14,62]

A set of force fields as implemented in the RMD code SIMCAT[104] is used to describe the principal atomic interactions involved during nucleation and growth of SWCNTs. Three main interactions are identified in the growth process. Metal-metal interactions are described by the many-body Sutton-Chen potential[38] which has been successfully employed to describe several properties of transition metals.[131-133] Carbon-carbon interactions are characterized through a potential[104] inspired on the second-generation reactive empirical bond order (REBO) potential developed by Brenner[39], which is known to describe the main carbon phases such as diamond and graphite and the transformations between them. Modifications were introduced to the REBO potential[104] to represent C-C interactions according the carbon coordination relative to the metal atoms. Metal-carbon interactions are described by the reactive potential developed by Martinez Limia et al[104], that is based on the Tersoff-Brenner scheme, but parameterized to differentiate among states of the carbon atom, including its position relative to the metal atoms and its hybridization state. This means that the potential is capable of distinguishing whether a catalyzed carbon is located inside or on the surface of the catalyst and if the bond is saturated or low coordinated. Similarly, the potential is able to differentiate among carbon atoms belonging to the nanotube or to the graphitic substrate. Therefore its complex parameterization can be used to model catalysts that interplay dissimilarly with the substrate and nanotubes. The *metal-substrate* adsorption energies were controlled manipulating an independent parameter in the metal-carbon potential, covering seven values between 160 and 925 meV. This range of energies agrees with some values reported in the literature for metallic clusters adsorbing on ceramic substrates. Our lowest interaction is comparable to that of the Ag/MgO[105] system which lies within the range 143 - 399 meV, whereas other metal-substrate interactions, such as, Cu/MgO (360 meV)[134], Ni/MgO (620 meV)[134] and Co/$SrTiO_3$

(2470 meV)[135] are in the higher range of our metal-substrate interaction values. The integration of the equations of motion was performed by the predictor-corrector algorithm with a time step of 0.5 fs. The total time of the simulation was set to 15 ns approximately, that represents a reasonable timescale in which relevant events are expected to occur, such as carbon defect formation and healing on catalyst surfaces, and lift off of nascent carbon caps giving rise to SWCNT growth.

We acknowledge that RMD simulations face some disadvantages that impede to fully emulate the CVD synthesis process. Our algorithm neglects the precursor dissociation process from which other species might be released thus changing the scenario for defects nucleation and healing. Furthermore, the limited time scale of the simulations (in spite of the process being artificially accelerated) hinders a more detailed analysis of defects lifetime and formation/healing mechanisms at later stages of growth. However, realistic modeling of all the atomic interactions involved in the synthesis process, provide close insights over reaction pathways at nucleation and initial stages of growth, where many structural features start to be forged. A better understanding of these initial stages is suggested to be the key for the synthesis of defect-free long SWCNTs with enhanced mechanical and electronic properties, as well as it could provide useful information regarding chiral selectivity during synthesis.

6.4 Results and discussion

Initially, RMD simulations of CVD growth were performed over a Ni_{32} catalyst particle. The metal-support interaction (E_{MS}) was modified from 0.26 eV to 1.02 eV in steps of ~0.25 eV through the adjustment of an independent parameter that regulates this interaction. The interaction between metal and saturated sp2 carbon was set to 0.1 eV, which is lower than all the values used in our previous report [136] and is actually closer to theoretical values for nickel.[137] A total of seven simulations were run at 1000K of temperature, whereas a high pressure of 8 atmospheres was used to guarantee rapid growth. The trajectories were followed after completion of 20 million of steps (10 ns). In order to quantify the concentration of defects in the nanotube wall, we calculated the number hexagons formed in the nanotube structure per catalyzed carbon that is not dissolved into the nanoparticle. To have a reference value for comparison, we can roughly establish a value of 0.5 as the theoretical number of hexagons per carbon (HPC) in an infinite long perfect nanotube with both ends open. This value is obtained by sequentially closing hexagons in the circumference and growth direction, until forming the cylindrical honeycomb lattice (Figures 6.1A and 6.1B). For both zigzag and armchair nanotubes the nucleation of the first (yellow) hexagon requires six carbon atoms, whereas closing the first rim requires four atoms per each hexagon, up to the final hexagon that requires only two. This gives an average of one hexagon formed each four carbon atoms added to the rim (HPC=0.25), which is independent of the rim diameter. However, the nucleation of the first hexagon of the second row (grey hexagon) requires only three carbon atoms for zigzag nanotubes whereas four atoms for armchair. In the case of zigzag tubes, additional hexagons in the same row are closed after addition of two carbon atoms per hexagon. The last hexagon of the second row closes by the addition of only one atom, compensating in such a way the three atoms needed to form the first hexagon of the row and giving an average of one hexagon per each two C atoms added to the structure (HPC=0.5). The same HPC value is obtained for the second row of armchair tubes, by closing hexagons with less amount of carbon that compensate the four atoms needed to form the first hexagon of the row (grey hexagon in Figure 6.1B). Independent of chirality, all hexagons formed starting at this point will follow the same mechanism of the second row with a HPC=0.5. Consequently, as the nanotube grows to an infinite length, the number of carbon atoms needed to form the hexagons in the rim will be negligible compared to the number of carbon atoms required to form hexagons in the body. Therefore, the overall theoretical HPC for a perfect nanotube will approach a value of 0.5 as it grows to infinite length, and this value will not depend on the diameter or chirality of the tube.

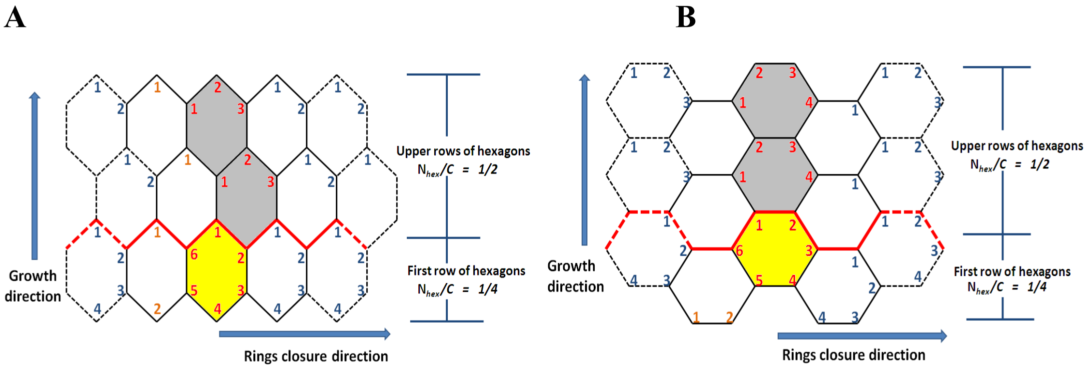

Figure 6.1. Number of hexagons formed per catalyzed carbon in SWCNTs. A. Zigzag. B. Armchair. Redlines separate the first (bottom) row from the upper row. The yellow hexagon corresponds to the first hexagon closed overall. Grey hexagons represent the first hexagon of the corresponding row.

From the previous analysis, we infer that the total number of hexagons per carbon atom of two perfect nanotubes will differ if both nanotubes do not have the same length. This makes a time-based comparison from the simulations to be unfair if the nanotubes do not exhibit similar dimensions at a given time. Consequently, at each instant, the total number of hexagons per carbon calculated through MD simulations ($(N_{hex} / C)_{MD}$) must be normalized respect to an equivalent quantity for a perfect nanotube with the same length ($(N_{hex} / C)_{theory}$). This gives us a variable that we call percentage of quality (quality %) and measures the relative defectiveness of the nanotube structure (equation 6.1).

$$quality\% = \frac{\left(\frac{N_{hex}}{C}\right)_{MD}}{\left(\frac{N_{hex}}{C}\right)_{theory}} \times 100 \tag{6.1}$$

Following the analysis of Figure 6.1, the general form of the $(N_{hex} / C)_{theory}$ is then calculated as a function of the number of rows (N_{rows}) and the number of hexagons per row which depends on the diameter ($N_{hpr}(D)$) (equation 6.2).

$$\left(\frac{N_{hex}}{C}\right)_{theory} = \frac{N_{rows} N_{hpr}(D)}{4N_{hpr}(D) + 2(N_{rows} - 1)N_{hpr}(D)} \tag{6.2}$$

The numerator in equation (6.2) corresponds to the total number of hexagons in the entire structure of a defect-free nanotube with two open ends. On the other hand, the first term of the denominator represents the four carbon atoms per hexagon needed to close the first row. The second term, in turn, introduces a correction for the rest of the nanotube where only two carbon atoms per hexagon are needed to complete a row. After simplifying the equation (6.2), all the $N_{hpr}(D)$ terms are canceled, removing in such a way the diameter dependence of the number of hexagons per carbon in a perfect nanotube (equation 6.3).

$$\left(\frac{N_{hex}}{C}\right)_{theory} = \frac{1}{2\left(1 + \frac{1}{N_{rows}}\right)} \tag{6.3}$$

Equation (6.3) is in agreement with every postulate aforementioned: It exclusively depends on the number of hexagon rows (length); when the number of rows is one, it takes a value of 0.25; and when the number of rows (length) goes to infinity, it approaches a value of 0.5. After substituting equation (6.3) into equation (6.1) we obtain the final expression for the quality percentage of nanotubes that is used in this paper to evaluate the concentration of topological defects in SWCNTs.

$$quality\% = 2\left(\frac{N_{hex}}{C}\right)_{MD}\left(1 + \frac{1}{N_{rows}}\right) \times 100 \tag{6.4}$$

After visual analysis of final configurations of each nanotube, the results were in agreement with our previously reported results.[136] For example, nanotubes grown on catalysts strongly attached to their support were more defective, whereas catalyst nanoparticles interacting weakly with the substrate led to growth of less defective tubes. This information is summarized in Figure 6.2, where the percentage of quality calculated through equation (6.4), is plotted as a function of time for four different metal-support interactions. Up to 4 ns, the structural quality of the nanotubes for the four cases remains quite comparable, around 50%. At ~5 ns the nanotube grown on the catalyst with the strongest adsorption on the support begins to nucleate preferentially non-hexagonal rings per catalyzed carbon. The quality of these tubes drops to ~30% as the nanotube keeps growing. After 7 ns, the quality of the nanotube grown on the catalyst interacting at 0.26 eV with its support is slightly enhanced to above 55%. On the other hand, the nanotube growing on the nanoparticle interacting at 0.77 eV with the substrate slightly dropped its quality to ~40% after 7 ns (Figure 6.2). The metal-substrate interaction has a critical repercussion on the catalyst shape, and on the total metallic surface in contact with the graphitic structures growing on the catalyst. This evidences the essential role that the catalyst surface might play on the healing of topological defects.

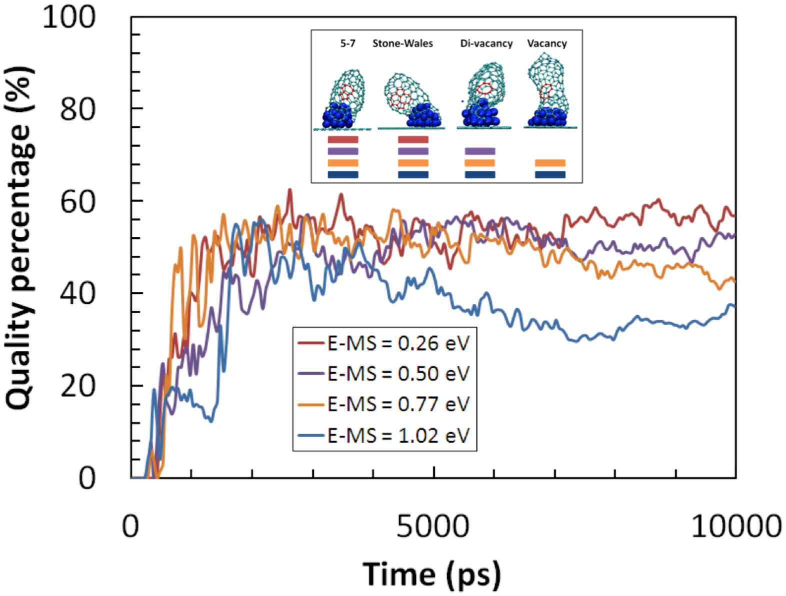

Figure 6.2. Percentage of quality calculated through equation (6.4) as a function of time for different metal substrate interactions (E-MS). Inset shows the various kinds of defects that might be present at given conditions. The color code in the inset is equivalent to the color code of the curves.

Z-density profiles previously reported for similar systems demonstrated that catalyst atoms tend to spread over the support when the attraction force between them is strong.[136] This leads to flattened catalyst shapes that keep reducing the number of atomic layers as the growth takes place. After 7 ns, the catalyst particles at E_{MS} = 26, 50, 77, and 102 meV present 4, 3, 2 and 1 atomic layer(s), respectively (Figure 6.3), which suggests a direct correlation between catalyst shape and concentration of defects. In order to address this hypothesis, we evaluated the role of the catalyst surface as a medium to heal defects and improve the quality of the nanotubes. The RMD trajectories demonstrated that defects nucleated on the catalyst surface were able to reorganize into hexagonal networks (Figure 6.3). As long as the non six-membered rings stayed in close interaction with the catalyst surface, surface diffusion, carbon precipitation and catalytic events at the catalyst/nanotube interface, enabled the restructuration of the lattice to heal defects.

Nonetheless, as soon as the defective carbon network lifted off, defects became stable since the catalyst surface lose its capacity to lower energetic barriers for carbon diffusion and bond rotations. Therefore, as catalysts with flattened shapes reduce their contact surface with nanotube sidewalls, they favor the fast stabilization of defects and the high concentration of non-hexagonal rings on the nanotube structure (Figure 6.4).

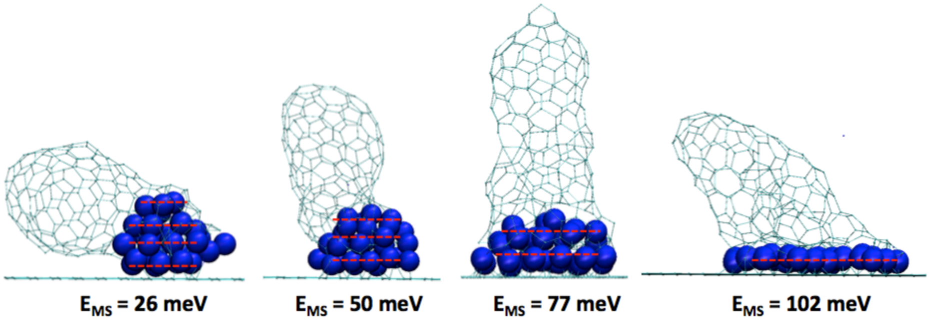

Figure 6.3. Number of layers exhibited by a Ni_{32} catalyst cluster as a function of the strength of interaction with the support.

Not only the concentration of defects is closely related to the catalyst shape. The type of topological defect that nucleates in the nanotube wall is also linked to the catalyst shape and therefore to the metal-support interaction energy. The 5-7 type of defect was found in every nanotube grown from our RMD simulations (Figure 6.2, inset), no matter what E_{MS} value was set. Because of the low formation energy of 5-7 defects compared to other defects, the dynamic nature of the growth process, and the high growth rates, the presence of 5-7 defects turns out to be unavoidable. As the metal-support interaction is made stronger and the catalyst becomes flatter, 5-7 defects are more frequently found in the tube structure as a result of rapid detachment of carbon rings and interrupted carbon diffusion seeking more stable configurations (Figure 6.4). Although Stone-Wales (SW) defects can be found at low metal-substrate interactions (associated with low amount of defects), their presence in the nanotube sidewall results from local concentrations of 5-

7's that recombine into 5-7-7-5 arrangements. As a consequence of a further increase in the metal-support attraction force, five and seven-membered rings stop being the exclusive source of topological defects on the structure. Flat catalysts lead to the formation of larger rings associated with vacancy and di-vacancy type of defects. Large carbon rings such as octagons and nonagons are nucleated only on catalysts with extremely flat structures, and generally demand formation of surrounding pentagons in order to eliminate dangling bonds. This has a significant impact in the total number of carbon atoms not used to form hexagons, and therefore, in the quality percentage calculated using equation (6.4). Vacancy defects were seen more often in nanotubes grown on bi/mono-layer catalysts. At these conditions, carbon caps lift-off so rapidly that they are not able to minimize dangling bond through structural rearrangements on the catalyst surface. Therefore, low coordinated carbon atoms were frequently observed in the tube sidewall during growth on catalysts with these particular shapes (Figure 6.2, inset).

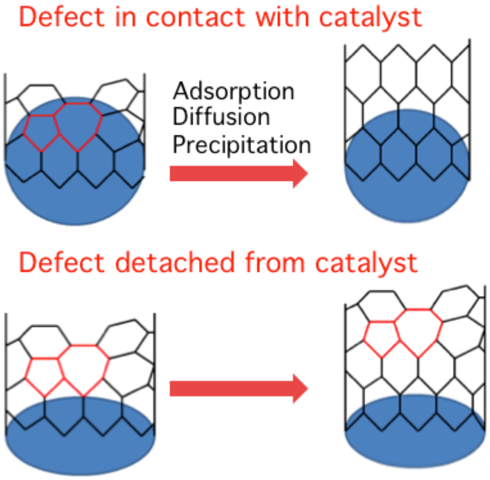

Figure 6.4. Role of the catalyst surface in healing defects. Defects can be healed on the catalyst surface via three mechanisms: Carbon adsorption, carbon surface diffusion, or carbon precipitation from bulk (top). Once the defect lifts off, the defect cannot be healed (bottom).

Figure 6.5 illustrates a defect formation mechanism valid for vacancy and di-vacancy defects. The mechanism follows six steps after starting with the formation of nanotube edge delimited by carbon atoms potentially forming a defect. Rapid addition of catalyzed carbon to the edge as a result of high pressures, leads to the fast growth of carbon chains in close interaction with the support. Carbon chains formed in the second step bend as a consequence of substrate repulsion to neighbor carbon atoms. Highly unstable pentagons are formed due to rapid formation of rings, which leads to ring recombination into larger rings assisted by carbon diffusion on the catalyst surface. Part of the large ring lifts off the catalyst surface. The size of the ring grows, as the flatness of the catalyst does not allow the healing of this defect through further carbon diffusion. Catalysis of carbon atoms at the edge leads to formation of even less stable carbon squares and triangles that end incorporated into a bigger carbon ring. However, very large rings are also unstable and low coordinated carbon atoms from the large ring try to interact with metal atoms at the top of the catalyst. This favors the ring size reduction by imposing a bamboo growth through formation of carbon chains at the inner part of the nanotube cap. Once the large ring lifts off from the catalyst surface eliminating any kind of interaction with it, the defect becomes stable and the catalytic healing is impossible. This mechanism differs in some details for different growths at the same conditions. Intermediate states may vary (Figure 6.5), such as the number of pentagon formed at the edge, the size of the first ring, and/or the extent of ring growth and reduction. Nonetheless, the overall defect formation mechanism remains the same, and vacancy/di-vacancy defects are generally related to bamboo growth. This is in agreement with our previous results in which inner walls were grown only on flat catalysts at high metal-support interactions. [136,138]

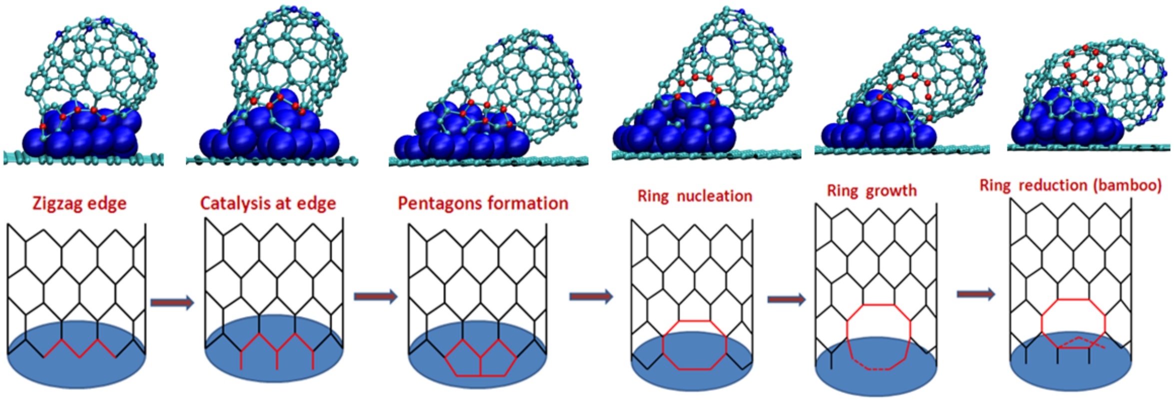

Figure 6.5. Formation mechanism for vacancy type of defects (mono and di-vacancy). The flatness of the catalyst is the key factor to the nucleation of large rings due to their fast stabilization on the nanotube wall. Red dots represent the atoms that will finally form the large ring.

The analysis of defect equilibration within the nanotubes structure, as shown in Figure 6.4 applies to most kind of defects. However, Stone-Wales arrangements are not included in this hypothesis and stabilize along the nanotube structure as soon as all carbon atoms belonging to the defect stop interacting with the catalyst surface. Figure 6.5 illustrates the formation mechanism of a SW defect elucidated by the RMD trajectory. Unlike what it has been said about SW defects, the nucleation of this defect does not involve a bond rotation in the graphitic structure of the tube. Although carbon diffusivity makes bond rotations plausible on catalyst surfaces, we can reliably say that the net rotation of the main bond (green bond in Figure 6.6) is practically null. The time frames in Figure 6.5 demonstrate that only ~3 ns elapse since the main bond is initially formed until the SW defect is finally stabilized outside the reach of the catalyst surface. During these 3 ns, the main C-C bond undergoes insignificant alterations in its orientation respect to the nanotube principal axis, despite catalytic phenomena taking place around it. This bond becomes part of different carbon rings before permanently settle in the center of the 5-7-7-5 configuration of the SW defects. The SW defects are then nucleated as a result of the incorporation of a newly created 5-7 defect into a preexistent 5-7 defect (1.99 ns). This phenomenon is frequently observed in our RMD simulations due to high local concentration of 5-7 defects because of the use of elevated growth rates. Accounting the presence and measuring the concentration of SW defects in nanotubes represents an experimental challenge since this defect affects only four adjacent hexagons without having repercussions on the physical behavior. We demonstrate that SW defects might be present in the graphitic lattice of the nanotube at these specific growth conditions. The net energetic cost for SW formation in nanotubes has been said to approach the thermodynamic limit of 3.5 eV due to the reactivity of carbon atoms involved.[122] The RMD trajectory here reported (Figure 6.5) proves that the catalyst allows the SW defect formation without comprising a bond rotation, which might ease the thermodynamic path and lower the formation barrier through carbon supply and surface diffusion.

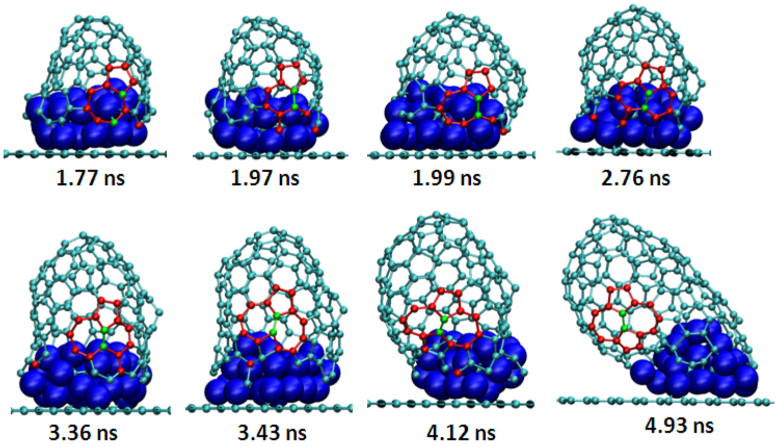

Figure 6.6. Formation mechanism for Stone-Wales defects. The green bond represents the principal bond separating the two heptagons in the 5-7-7-5 configuration. The rest of atoms involved in the defect are represented by red dots.

Further simulations were performed with the purpose of studying the effect of precursor gas phase density on the defects concentration. The temperature was kept at 1000 K and the metal-substrate interaction was fixed to 50 meV, which reduces the probability of mono-vacancy formation and dangling bond presence along the nanotube body. The pressure was sequentially decreased in steps of 2 atmospheres from 8 atm down to 2 atm. The pressures were calculated assuming ideal gas conditions for density values between 0.015 and 0.06 atoms/nm^3. It has been said in discussions above that rapid incorporation of carbon atoms into growth front contributes to the low quality of the nanotubes. The results summarized in Figure 6.7A show that, indeed, after decreasing the density of the gas phase, and consequently the growth rate, the concentration of defects can drop to values as low as 25% (Blue curve at ~15 ns, Figure 6.7A). Despite the growth at 6 atm resulted in a more defective nanotube compared to the one grown at 8 atm, the qualitatively trend remains. Eight and six atmospheres translate into the presence of 8 and 6 precursor atoms in a simulation box ~130 nm^3. In either case, the growth rate is so high that impedes the effective healing of defects on the catalyst surface. The rates of carbon addition to the nanotube rim overcome the time frames required for defect healing.

Simulations modifying the nature of the carbon source were also performed with the same range of pressures, and same growth temperature and metal-substrate interaction. Instead of monomer precursor, we now simulate the supply of carbon in the form of dimer. Although the pressure values are equivalent in gas phase for both cases, the total carbon supplied after catalytic collision is actually doubled for the case of dimers. Figure 6.7B shows a comparison between carbon supplied in form of monomer and dimer. After 15 ns, the nanotubes grown from single carbon atoms exhibited better quality than those grown from dimer, as represented by the blue curves above the red ones in Figure 6.7B. These results suggest that the carbon addition in form of dimer may introduce an additional constraint for carbon mobility and diffusion on the catalyst surface that hinders the defect healing process. The results are even more evident at low growth rates, as seen from comparing the dotted blue and red curves in Figure 6.6B.

Carbon supplied as a dimer represents a situation in which the catalyst fails to dissociate carbon-carbon bonds in precursors such as ethylene or ethanol.

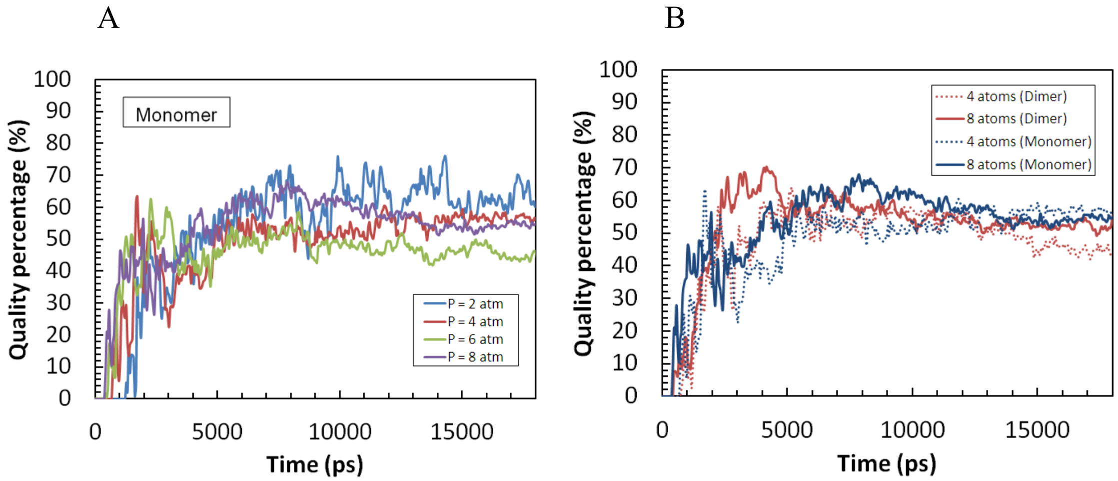

Figure 6.7. Percentage of quality calculated through the equation (6.4) as a function of time and for different gas phase total pressures. A. Results for monomer type of precursor. B. Comparison between addition of 4 and 8 precursor atoms in form of dimer and monomer

In order to deepen into the role of the catalyst surface on healing defects, simulations for catalyst of different sizes were carried out. Besides Ni_{32}, catalyst particles with 80 and 160 nickel atoms were used. Ni_{32}, Ni_{80} and Ni_{160} are nanoparticles characterized by having diameters of 1.1, 1.5 and 1.8 nm, respectively. Temperature and metal-support interaction remained the same as in the study of the pressure effect. Results for different catalyst sizes, shown in Figure 6.8, reveal a tendency for caps nucleated on small catalysts to reach better qualities just after lifting off. The snapshots inside Figure 6.8 correspond to the instant in which each nanotube has reached ~1 nm of separation from the topmost layer of the catalyst nanoparticle. As can be inferred from the figure, the larger the catalyst the most defective the initial cap. Nonetheless, as the nanotubes continue to grow, the quality of the nanotube grown on a Ni_{32} nanoparticle starts to steep declining in quality toward values around 50%. After 10 ns, the amount of defects present in the nanotube is independent on the catalyst size. It is worth it to remark that as the catalyst nanoparticle becomes larger the total surface area exposed increases, and therefore, the fraction of the nanotube lattice remaining in contact with the catalyst surface will be larger. Snapshots in Figure 6.8 illustrate how the nanotube cap nucleated on Ni_{160} still has plenty of carbon atoms deposited on the catalyst surface. One may conclude that defective carbon structures on Ni_{160} still have a chance to heal as a consequence of the large surface and bulk diffusion at which they are exposed. Actually, no matter if defects are embedded into the nanotube body, the chances to heal remain intact as long as they are still interacting with the catalyst surface.

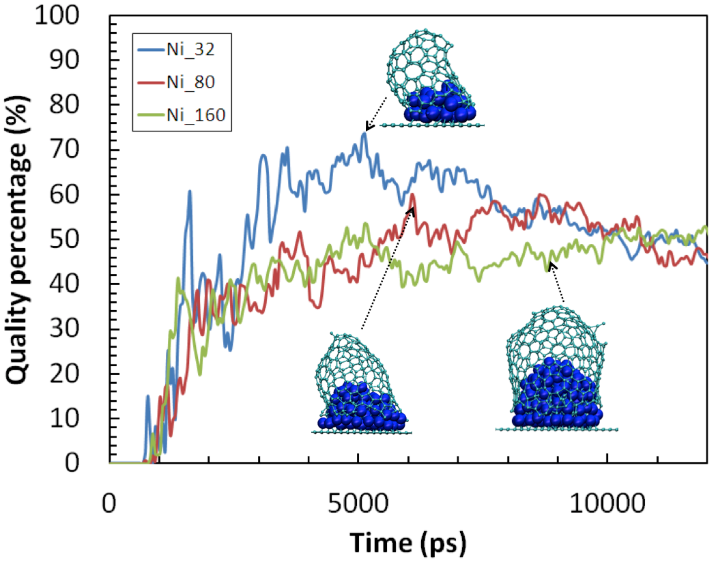

Figure 6.8. Percentage of quality calculated through equation (6.4) as a function of time and for different gas catalyst sizes. Snapshots correspond to nanotubes with the same length (1nm) respect to the top of the catalyst, and grown from different catalysts. The arrows point out the time at which they reach the given length

Figure 6.9A verifies the previous assumption. A 5-7 defect completely embedded into the nanotube sidewall at t_1 is healed following several steps of ring openings and reconfigurations that end in a nearly-perfect hexagonal network at t_6. Ding and coworkers reported that healing a 5-7 defect is almost impossible once it is embedded into the hexagonal network due to high energy barriers for healing. Instead our RMD simulations suggest that, under growth conditions, defects embedded into the network can find their energetic path to healing via carbon surface diffusion and precipitation from the bulk, as demonstrated in Figure 6.9A.

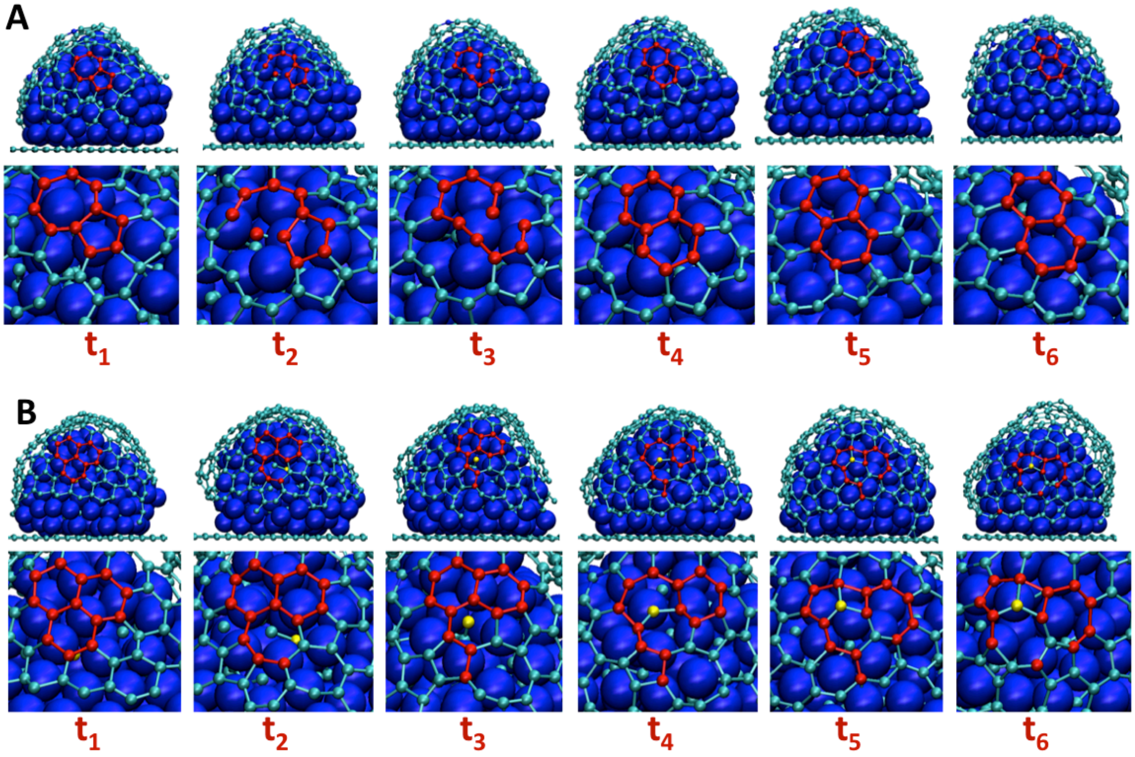

Figure 6.9. Reconstruction mechanism of embedded carbon networks. Systems were analyzed by the time (t_i), where $t_6 > t_5 > t_4 > t_3 > t_2 > t_1$. A. Embedded 5-7 defect is healed on the catalyst surface via carbon surface diffusion. B. Embedded hexagonal network is disrupted via carbon surface diffusion and precipitation of carbon atom (yellow) from bulk.

The enhanced surface area of the largest catalyst particle, however, does not only assist defect healing but also favors defect formation. Hexagons embedded into a near perfect graphitic network are exposed to network reconstruction, as they remain deposited on the catalyst surface. The stability of the hexagonal network might be then jeopardized by the high kinetic energy at the catalyst-cap interface and the mass transfer from the bulk of the catalyst toward the interface. As seen in Figure 6.9B, an embedded network comprising three adjacent hexagons (t_1) is disrupted by surface diffusion and reorganization into a transitional 6-6-7 configuration (t_2). The instability of this arrangement allows the reconfiguration of the network back to six adjacent hexagons (t_3). A single carbon (yellow atom in Figure 6.9B) is precipitated into the nanotube-catalyst interface at t_3 and favors breaking of a C-C bond in order to accommodate in the middle of two heptagons at t_4. After this event takes place, the original perfect hexagonal network is never recovered despite the probability for defect healing inherent to the cap-catalyst interaction. The carbon precipitation at the interface has a significant repercussion on the concentration of defects. The time frame t_1 to t_6 in Figure 6.8B corresponds to ~5 to ~6 ns. Figure 6.8 illustrates that the green curve, corresponding to Ni_{160}, undergoes a sudden drop in 14% of quality within this interval.

It has been experimentally observed that the growths carried out at low temperature induce the formation of nanotubes with lower amount of defects. We decided to explore the influence of temperature on defects concentration through RMD simulations. A Ni_{32} particle was used as a catalyst at a constant pressure of 8 atmospheres for a monomer precursor, and a metal-substrate interaction of 50 meV. Results summarized in Figure 6.9 demonstrate that low temperatures are not favorable for the growth of quality nanotubes, contrary to what it has been suggested theoretically. Ding et al reported that the combination of low temperatures and low growth rates improve the quality of the nanotube,[128] although typical high growth rate of classical molecular dynamics simulations may result on an inverse effect. From their results it is inferred that when the growth rate is too high defects concentration increases as the temperature decreases since healing rarely takes place at these simulation conditions.

Nevertheless, defective nanotubes grown at low temperature have been also observed experimentally.[139,140] RMD growth rates corresponding to our simulations performed at lowest temperatures were not even approaching experimental values (in the order of μm/s), as seen in the appendix A (Figure A1). The effect of temperature in our simulations is given by the rate of carbon collision to the catalyst surface. However, less frequent catalytic conversion at the second lowest temperature (300K) lead to a growth rate of ~0.07 m/s, which is lower than typical *ab initio* molecular dynamics growth rates at 1200 K (1 m/s).[141] Therefore, we may infer that the growth is not so fast and the low kinetic energy is having a negative impact on the cap quality as significant as the MD growth rate. Low temperatures approaching room temperature may induce thermodynamic phase transitions in the catalyst nanoparticle. From 400 to 300 K, nickel nanoparticles with ~1 nm of diameter (32 atoms) may experience first order phase transition as demonstrated by the steep jump in the Lindemann index observed in this range of temperatures (See appendix A (Figure A2)). Catalyst particles in solid state obstruct the diffusivity of carbon atoms during nucleation, and as stated above, carbon bulk and surface diffusion are essential for defect healing on catalyst surface. Consequently, catalyst nanoparticles in quasi-liquid states are also desirable to avoid nucleation of topological defects. Low temperatures and growth rates might improve the quality of the nanotube as long as the temperature is not so low that could induce a solidification or even encapsulation of the catalyst nanoparticle. Our results demonstrate that CVD at temperatures below 400 K lead to nucleation of amorphous carbon rather than carbon nanotube due to the lack of diffusion and defect healing. Below 400 K, cap lifting off is also restricted so that caps remain so small and defective that could not even be considered as nanotube caps, as seen in the appendix A (Figure A3).

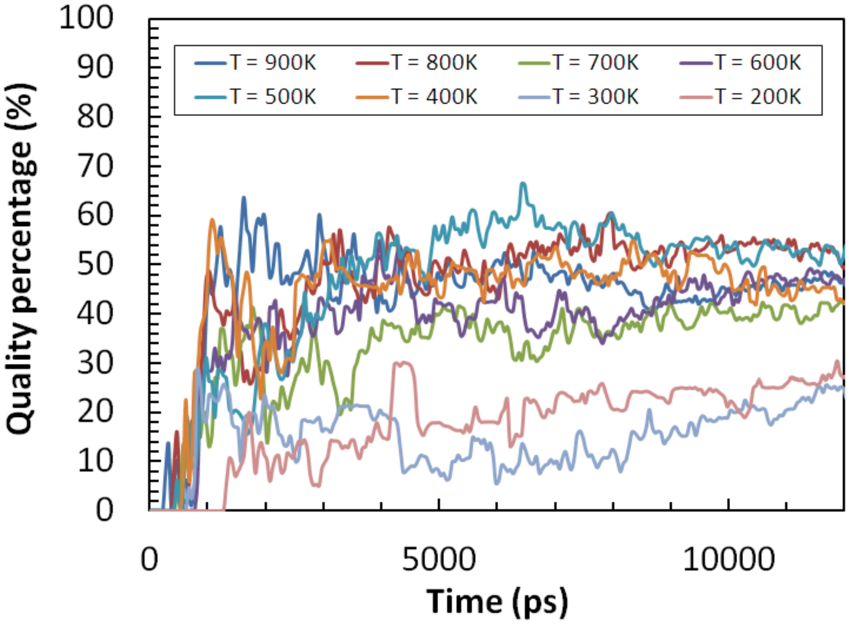

Figure 6.10. Percentage of quality calculated trough the equation (6.4) as a function of time and for different temperatures.

6.5 Conclusions

RMD simulations helped elucidate the crucial role played by the catalyst on healing defects in SWCNTs. Trajectories demonstrated that defects could be healed as long as the carbon network is still adsorbing on the catalyst surface. Surface diffusion and precipitation from the bulk, as well as catalysis at the nanotube edge, appear as the principal mechanisms for defect healing. It was proven that the type of defect that nucleates in the nanotubes sidewalls is directly linked to the catalyst morphology. Stone-Wales and 5-7 defects are present on nanotubes no matter how rounded the catalyst shape is, whereas vacancy and di-vacancy defects are characteristic of nanotubes grown on flat-shaped catalysts. In consequence, catalysts strongly deposited on the substrate led to the synthesis of more defective tubes than those grown on spherical catalysts. Our results were in agreement with different theoretical and experimental studies that establish low growth rates as essential to enhance the nanotube quality. Since the growth rate also depends on the strength of the metal-carbon interaction, these results can be extended to other types of catalysts. Catalysts with weak metal-carbon adhesion are expected to nucleate more defective nanotubes due to fast cap lift-off and reduced deposition times, which does not allow carbon diffusivity and healing on the catalyst surface. It was also shown that a dimer precursor introduced a mobility constraint on the catalyst surface that hinders the healing process. Due to the growth rates herein used, which are typical of classical MD simulations, low temperatures did not privilege the growth of high quality SWCNTs. The results suggest that temperature is having a more significant impact on the mobility of catalyst, and therefore on the diffusivity of carbon atoms, than on the growth rate. Consequently, in spite of the lower growth rate, they cannot be healed due to the lack of diffusivity of carbon atoms. Small catalyst nanoparticles led to nucleation of caps with high structural quality, although the concentration of defects converges to similar values as the growth continues. RMD trajectories showed that larger net surface of catalysts favors equally defects nucleation and healing. Trajectories of defects healing/formation on large catalyst particles showed that embedded networks, either defective or hexagonal, can be reconstructed via surface diffusion and/or carbon precipitation. SW and vacancy type of defects were proven to be formed through mechanisms different than bond rotations and carbon atoms removal, respectively.

7. PREFERENTIAL ADSORPTION OF ZIGZAG SINGLE-WALLED CARBON NANOTUBES ON THE ST-CUT SURFACE OF QUARTZ*

7.1 Summary

Synthesis of horizontally aligned single-walled carbon nanotubes (SWCNTs) has achieved high degree of orientation and selectivity when specific cuts of quartz surfaces are used as support. In this study we demonstrate that finite-length zigzag nanotubes are adsorbed stronger than armchair tubes on the quartz support. This is done through density functional theory calculations that evaluate the interaction between SWCNTs and the ST-cut surface of the quartz substrate. Among the nanotubes studied, the (7,0) presents the strongest adsorption energy, found along the [010] direction, which is parallel to the y-axis. Unexpectedly, patterns delineated by silicon and oxygen atoms along the [010] direction established the strongest as well as the weakest adsorption energies. This suggests that the nanotube electronic band structure is a key factor on the preferential adsorption of zigzag tubes. Charge analysis demonstrates the role of oxygen atoms on the partial oxidation of nanotube atoms closest to the substrate. Finally, the analysis of the electronic density of states proves that atomic interactions between substrate and nanotubes induce modifications of the occupied states near to the Fermi level, which can potentially modify the metallic or semi-conducting character in adsorbed SWCNTs.

7.2 Introduction

Since their discovery by Iijima in 1991[142], single-walled carbon nanotubes (SWCNTs) have been suggested as candidate materials for numerous technological applications because of their extraordinary mechanical and electrical properties. Some nanoelectronic devices, especially field effect transistors, are potential application fields

---

[*] Reprinted with permission from Juan C. Burgos and Perla B Balbuena. "Preferential Adsorption of Zigzag Single-Walled Carbon Nanotubes on the ST-Cut Surface of Quartz." The Journal of Physical Chemistry C **117**(9): 4639-4646. Copyright 2013, American Chemical Society.

in which SWCNTs may satisfy performance demands due to their outstanding thermal conductivity, mobility and good mechanical stability [143,144,145] . The wide range of applicability of SWCNTs has led to the development of a large number of techniques that aim to produce these novel materials in an inexpensive and massive way [146,147]. Most of the growth techniques, however, are not selective enough to control the structural features of the nanotube. The nanotube diameter and chirality, which determine their electronic behavior[148], remain the most difficult properties to control despite recent advances in this field [14,149,150]. The direct use of random mixtures of SWCNTs, that contain different chiralities, diameters, and lengths as a result of growth processes, may hinder their performance in electronic devices. Consequently, expensive and complex separation processes, such as dielectrophoresis[151,152] and density gradient centrifugation[153], are frequently demanded to fractionate pure semiconducting SWCNTs before their final utilization.

Therefore, researchers are putting their efforts in finding reliable methods to produce bundles of nanotubes for direct use in applications requiring selective chiralities. However, the alignment of SWCNTs in the bundle arises as a further issue - in addition to chirality homogeneity- obstructing the development of fully functional SWCNT-based electronic devices. Recently, Liu and coworkers[154] found an experimental strategy to grow horizontally aligned SWCNTs on ST-cut surfaces of quartz. This surface corresponds to a specific crystallographic plane lying at 42° from the y-axis approximately; however, the full identification through its crystallographic indices have been matter of debate by researchers, as it will be seen in the next section. In Liu's work, lines of catalyst particles were disposed on a patterned ST-cut surface of quartz for the catalytic synthesis of nanotubes. Growth of high densities of aligned carbon nanotubes was explained on the basis of the suppression of the tip growth mechanism that led catalyst nanoparticle collisions and preferential atomic interactions in the x-axis direction. The particle collisions led to an increase in the diameter of both the particles and nanotubes. This was followed by the loss of the preferred atomic interaction line and the consequent bending of the growth directions. Other authors have reached a different conclusion that affirms that the bending angle, which may be observed in the growth direction, is directly related to the angle of the O-Si-O segments of the quartz surface [155]. Liu and coworkers later demonstrated that the aligned growth directions are exclusively owed to epitaxial interactions between the outer shell of nanotubes and the atoms of the quartz surface[156] even though the important contribution of surface annealing on the enhancement of the tube alignment has also been demonstrated [155]. Additionally, it was found out that the use of specific cuts of quartz as a substrate for catalyst nanoparticles and the presence of methanol in the precursor gas mixture have led to preferential growth of aligned semiconducting SWCNTs[149]. The highest degree of alignment and semiconducting selectivity is exhibited in the 36˚ and 42˚ Y-cuts of quartz. It was stated that OH radicals generated from methanol at reaction temperatures (900˚C) etch most metallic nanotubes; however, the role of the substrate lattice on the semiconducting selectivity remains unclear. Hong et al[157] were able to find semiconducting selectivity on the ST-cut (36˚ Y-cut) surface of quartz with a growth mechanism assisted by UV irradiation. The experiment design led them to conclude that the UV irradiation was responsible for the destruction of metallic caps at very early stages of growth.

Even though different experimental approaches have been able to enhance the alignment and semiconducting selectivity, the molecular bases for this alignment/selectivity have not been fully established yet. Thus, in this work we present a detailed theoretical study based on density functional theory (DFT) calculations for SWCNTs on specific quartz surfaces which aims to correlate the alignment and selectivity to the structural and electronic properties of SWCNTs.

7.3 Computational and system details

DFT calculations were carried out using the Vienna ab initio simulation package (VASP) [158,159]. The code describes electronic interactions by the projector-augmented (PAW)[160] method, which is expanded within plane wave basis sets. Only plane waves with kinetic energies below 400 eV were included in the basis set. The Perdew-Burke-

Ernzerhoff (PBE) exchange model[47], which is a generalized gradient approximation (GGA) function, was employed to describe the electron exchange and correlation effects. GGA functionals included in VASP satisfy the uniform density limit. This feature makes them ideal for the suitable representation of periodic boundary conditions and predictions of physical properties of bulk materials and surfaces. Because of the semiconducting and insulating character of the system, the partial occupancies were set to each orbital following the tetrahedron method with Blochl corrections[161]. The smearing width was established in 0.1 eV. Convergence criteria were set to $1x10^{-4}$ and $1x10^{-3}$ for electronic and ionic minimizations, respectively, whereas a 6x6x1 Monkhorst pack grid[49] was used for the Brillouin zone integrations carried out over the system.

Structural information about silica (SiO_2) surfaces at growth conditions was obtained from literature in order to select the most appropriate model system for the DFT calculations. A typical chemical vapor deposition (CVD) process to produce SWCNTs is operated at approximately 700°C and 1-10 atm[147,162]. At these specific conditions, bulk SiO_2 can be found at two possible thermodynamic phases, a trigonal α-quartz or a hexagonal β-quartz [155]. Since β is the stable phase of quartz above 650°C and phase transformations from β to α are slow [155], we chose a β-quartz bulk unit cell to cleave our silica surface. In this study, the ST-cut surface of quartz was used because of its remarkable selectivity and capability for induction of alignment, which have been observed experimentally when nanotubes grow horizontally on this type of substrate. Despite the lack of information about the crystallographic plane associated to the ST-cut, different studies have been able to identify its Miller indices. Rutkowska et al used X-ray diffraction experiments to distinguish the (01-11) as the crystallographic plane corresponding to the ST-cut surface of quartz. The normal to the surface lies near to the [121] direction, which in turn forms an angle of 42.5° with the y axis [010]. Other authors suggested (01-11) as a different crystallographic plane called r-face [163]. They claimed that the ST-cut surface of quartz is in fact a collection of diminutive r-faces that results in the (0 23 -23 27) crystallographic plane. These findings let us construct our surface using the surface cleavage tool of the Materials Studio package[164]. For simplicity, and because of the structural proximity of both surfaces, the (01-11) plane was chosen over the (0 23 -23 27) plane. The surface was modeled using a 1x2 supercell with 4 layers of thickness and 15 Å vacuum (Figure 7.1). Each layer is composed by 6 Si atoms and 12 O atoms, which keep the stoichiometric relation of silica. Three different SWCNTs were optimized and placed on top of the surface along different directions. SWCNTs (4,4), (6,0) and (7,0) with finite lengths were fit in the unit cell and saturated with hydrogen atoms at the open edges (Figure 7.1) to minimize the effect of the dangling bonds. Electronic band structure calculations of SWCNTs have shown that all armchair nanotubes are metallic, whereas zigzag nanotubes are semiconductors with a band gap width dependent upon their chiral indices (n,m) [148,165] . With the selection of our three nanotubes, we are considering three possible electronic behaviors. SWCNT (4,4) is metallic (n–m = 0). Chiral indices (7,0) correspond to a semiconducting tube with a moderate band gap (n-m ≠ 3k, k=1,2,3,...). The remaining zigzag tube (6,0) is a narrow-gap semiconductor (n-m = 3k, k=1,2,3,…), although it has been found to be metallic because of hybridization of σ* and π* orbitals that results from the small diameter. [166] In total, 6 positions corresponding to 4 crystallographic directions were tested for each nanotube (Figure 7.1).

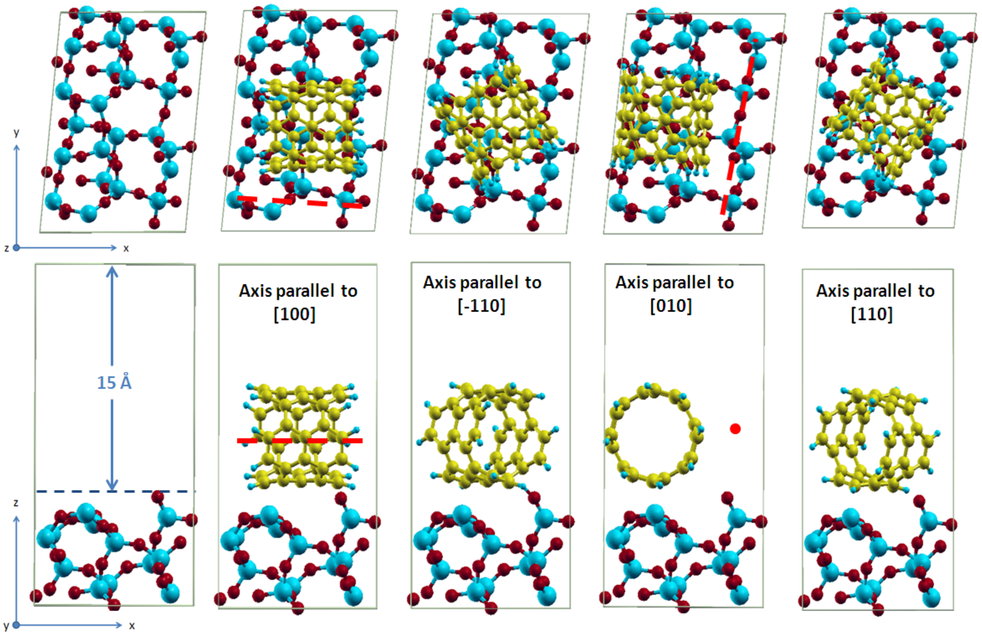

Figure 7.1. Top and side views of ST-cut surface of quartz represented by a 2x1 slab with a vacuum space of 15 Å. Blue and red spheres represent silicon and oxygen atoms, respectively. The two bottom layers were fixed whereas the two on top were allowed to relax. Three different directions were tested: [100], [-110], [010], and [110]. Carbon atoms forming nanotubes are represented by small yellow spheres, whereas small blue spheres correspond to hydrogen. Two additional positions were tested next to the [100] and [010] directions as shown by the red dashed line or the red dot.

7.4 Results and discussion

7.4.1 Adsorption energies

The adsorption energy per carbon atom (E_{ads}) was calculated based on the total number of carbon atoms of each nanotube, ($N_{C\text{-atoms}}$), according to the following equation: $E_{ads} = (E_{system}–E_{clean\text{-}surface}–E_{SWCNTs})/N_{C\text{-atoms}}$. Segments of SWCNTs (4,4), (6,0), and (7,0) were formed by 40, 36 and 42 carbon atoms, respectively. The results are summarized in Figure 7.2. Both zigzag nanotubes exhibited stronger adsorption than the armchair one along every direction of the quartz substrate (Figure 7.2). Carbon nanotubes (6,0) and (4,4) found their ideal alignment when their principal axes lied parallel to the [110] direction which is 45° away from the x-axis. Nevertheless, in the case of the armchair tube the magnitude of its binding energy was 0.045 eV/C weaker than the binding energy of SWCNT (6,0) along its most favorable [110] direction (Figure 7.2). On the other hand, the nanotube (7,0) adsorbed favorably on both parallel positions along the y-axis ([010](1) and [010](2)). The overall strongest adsorption energy was obtained for SWCNT (7,0) when its axis was aligned parallel to [010](2) (0.137 eV/C). The result is comparable to that found for interactions of graphene on silica. [167,168] However, when the same nanotube (7,0) adsorbed aligned to the [-110] direction, the binding energy was only 0.02 eV/C weaker than the strongest binding energy. The small difference in adsorption energies between both directions can provide some clues for the nanotube bending during the growth on quartz, which has been observed experimentally[154,155]. The existence of a low energetic barrier between two growth directions may allow the bending of the nanotube axis as a result of small structural or dynamic variations. The catalytic growth of SWCNTs is a kinetic process in which length, diameter and chirality undergo fluctuations, which therefore affect the substrate/nanotube interactions. Since the energetic cost to bend is not too high, especially for nanotubes with long diameters,[169] a significant change in the tube structure is not required to shift the preferential substrate/SWCNTs interaction and deviate the nanotube axis.

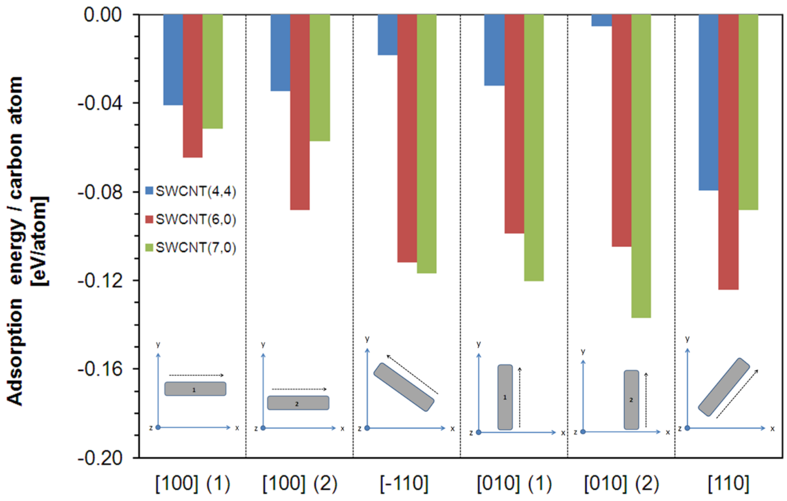

Figure 7.2. Adsorption energies per carbon atom on the indicated positions for the three nanotubes under study: SWCNT (4,4) (blue bars), (6,0) (red bars) and (7,0) (green bars).

Most nanotubes horizontally deposited along their preferential directions have been found interacting closely with silicon atoms (Figure 7.3). In the specific case of the SWCNT (7,0) along the [010](2) (strongest adsorption), two carbon atoms are found interacting tightly with two different silicon atoms from the surface top layer at distances below 2 Å. Interestingly, the strongest adsorption energy was the only case in which a carbon atom is in a close contact with an oxygen atom at a distance shorter than 1.5 Å. Similarly to SWCNT (7,0), for SWCNTs (6,0) and (4,4) along their respective favorable adsorption lines, silicon atoms set the main binding points between the nanotubes and the quartz substrate (Figure 7.3). Thus, lines of silicon atoms on silica supports might establish surface patterns for the growth of horizontally aligned SWCNTs.

Charge analysis was performed in order to assess the contribution of oxygen and silicon atoms to the adsorption phenomena. The most notorious pattern on the entire support is perhaps the deep channel delimited by a line of silicon atoms and a line of dangling oxygen atoms parallel to the y-axis. Along this channel, the nanotubes maximize their contacts with the substrate, minimizing in such a way the overall energy of the system. Surprisingly, along this channel aligned with the [010] direction, the strongest and the weakest adsorption energies were found for SWCNTs (7,0) and (4,4) respectively. This fact suggests a dependence of the adsorption energy on the structure of the nanotube.

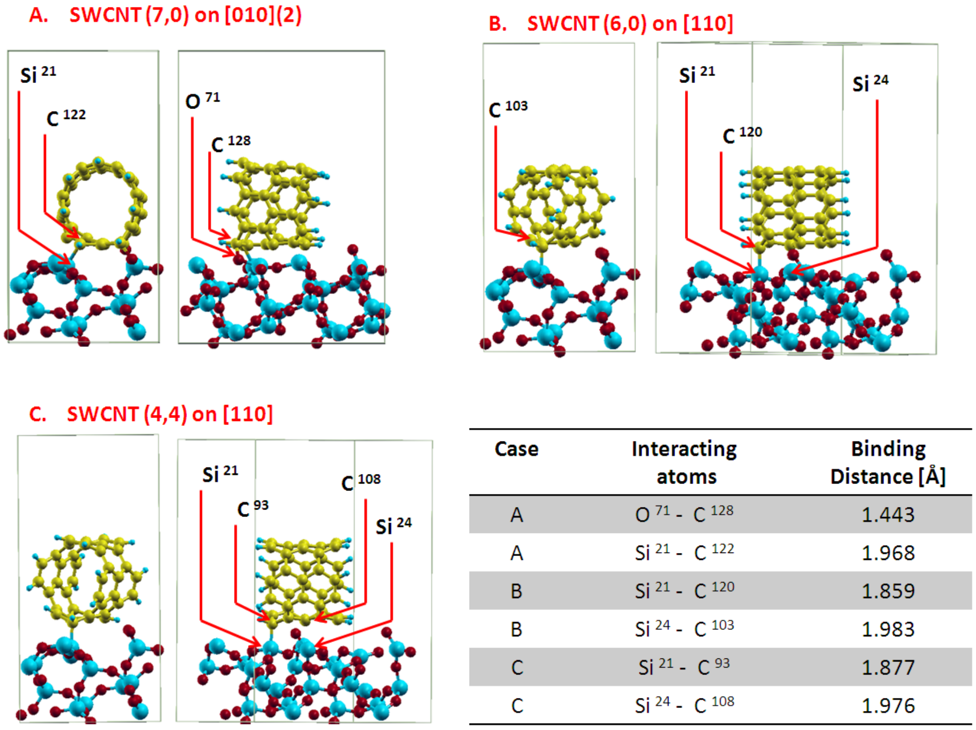

Case	Interacting atoms	Binding Distance [Å]
A	O ^{71} - C ^{128}	1.443
A	Si ^{21} - C ^{122}	1.968
B	Si ^{21} - C ^{120}	1.859
B	Si ^{24} - C ^{103}	1.983
C	Si ^{21} - C ^{93}	1.877
C	Si ^{24} - C ^{108}	1.976

Figure 7.3. Interaction distances for a) SWCNT (7,0) along [010](2), b) SWCNT (6,0) along [110], and c) SWCNT (4,4) along [010], which correspond to their strongest energy adsorption directions. Color code for the atoms as in Figure 7.1.

Because the three nanotubes in this study have approximately the same diameters (~5Å) and lengths (~ 7Å), differences in chiral angles remain as the only structural feature responsible of the preferential (n,0) adsorption. The nature of the weak affinity of the SWCNT (4,4) with the ST-cut surface of the quartz support may be linked to the electronic and magnetic properties of armchair nanotubes. The results herein reported suggest electronic affinity between zig-zag nanotubes and the ST-cut surface of quartz. Additional evidence is collected from electronic characterization of the nanotubes, and this will be a discussion topic in the following sections.

7.4.2 Charge analysis

After optimizing the nanotube-substrate systems, the charge density distributions were mapped on discrete planes parallel to the z-axis intersecting the closest binding distances. In principle, the charge density mapping confirmed the null electronic interaction between nanotubes sidewalls and the periodic image of the substrates in the z direction. The wide red space at the top of nanotubes (Figure 7.4) evidences the lack of net charge within this gap, which confirms the appropriateness of the simulation cell dimensions for the vacuum space. On the other hand, the map illustrates that the strongest interaction energies are always dominated by close contacts between silicon and carbon atoms, as discussed above. Intermediate electron population (green regions) was found at the interface between silicon atoms on the topmost layer of the substrate and carbon atoms from the nanotube side wall For nanotubes (4,4) and (6,0) aligned along the [110] direction, a net charge density in the range 0.6 – 0.8 e/$Å^3$ is observed at that interface (Figures 7.4A and 7.4B). Similar values of charge density are found at the Si-C contacts between SWCNT (7,0) and the quartz substrate along the [010](1) direction (Figure 7.4C). However, for the three cases just mentioned, the charge concentration at the interface between nanotubes and support is still low, which might be associated to the absence of oxygen atoms along the path of the nanotube. Indeed, the presence of an oxygen atom along the adsorption line of the nanotube induces the largest charge density at the nanotube/support interface. This is the case of the strongest adsorption energy (SWCNT (7,0) on [010] (2)), where the charge concentration reaches up to 1.4 e/$Å^3$ along the carbon-oxygen line of interaction (Figure 7.4D). Surprisingly, charge accumulation on top of oxygen from the uppermost layer is not a usual feature for all nanotubes aligned along [010](2). Unlike SWCNT (7,0), for the (4,4) armchair-support system, high levels of charge population at the nanotube-support gap are not found at any point of the interface (Figure 7.4E). Thus, the adsorption trend favoring the (7,0) nanotube along that direction is correlated to dense electronic clouds between interacting atoms, especially at C-O contacts.

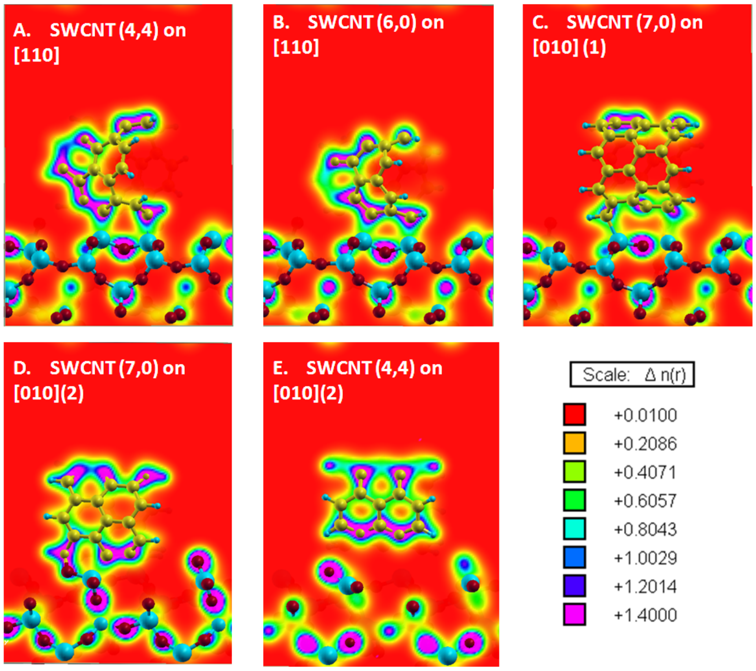

Figure 7.4. Charge density mapping for a) SWCNT (4,4) along [110], b) SWCNT (6,0) along [110], c) SWCNT (7,0) along [010](1), d) SWCNT (7,0) along [010](2), and e) SWCNT (4,4) along [010](2). The color chart displays ranges for the charge densities in e/Å^3.

To obtain a better insight about the role of nanotube structure on the strongest and weakest adsorption cases along the same direction, a further analysis of charge differences before and after adsorption was performed. Calculations of electron accumulation and depletion were carried out for the three nanotubes along the [010] (2) direction for an isosurface value of 0.7 e/Å^3. The results are shown in the Figure 7.5. For both zigzag nanotubes, there is a trend for the electron density to migrate from the top external region to the top inner region revealed by enhanced depletion on the top outer surface and accumulation in the top inner surface. Similarly, electrons migrate from the bottom inner region of the nanotube (enhanced depletion in Figures 7.5A and 7.5B) to the outer bottom region of the nanotube in contact with the substrate (enhanced accumulation). At discrete points within the interface corresponding to the Si atoms closest to the nanotube wall, a tendency of charge displacement toward the support is observed; nonetheless, silicon atoms do not redistribute their electronic density avoiding the overlap of silicon and carbon orbitals. Charge density changes in the quartz surface are specifically observed in oxygen atoms of the uppermost layer. These changes take place mostly in the direction perpendicular to the substrate plane by depletion at the interface and accumulation in the bulk (SWCNT (6,0) and (4,4)). SWCNT (7,0) adsorbing on the [010] (2) direction was the only case where the oxygen and carbon orbitals overlapped at the interface as a result of increase of the charge density accumulation on the oxygen atom. On the other hand, the (4,4) armchair nanotube does not undergo charge depletion neither accumulation as a consequence of its alignment on the [010](2) direction (Figure 7.5C), thus confirming a weak interaction. The charge population of the uppermost oxygen is displaced in the direction of the bulk suggesting the oxidation of the carbon atom in close contact with the oxygen atom. However, this oxidation is localized, and the charge density of the majority the armchair nanotube remains unperturbed by the substrate. Therefore, this analysis indicates how the charge distribution differs from zigzag to armchair nanotubes when they occupy the same positions on the substrate. The stronger adsorption energies and the charge accumulation at the bottom of (7,0) and (6,0) nanotubes suggest an affinity of the ST-cut surface of quartz with zig-zag nanotubes.

The analysis can be extended to nanotubes of larger diameter. For instance, zigzag SWCNTs of chiral index larger than seven can have a larger number of interaction contacts with surface oxygen atoms, making the effective total adsorption energy stronger. However, normalizing the energy by the augmented number of carbons will adjust the adsorption energies per atom to comparable values to those reported in

Figure 7.2. In consequence, the qualitative trends discussed here should be kept for nanotubes of larger size.

Process variables such as temperature can alter the interaction between nanotubes and support. The DFT calculations are carried out at 0K, however they provide a good description of the electron exchange and correlation interactions that also take place at high temperatures. In addition, other side reactions can occur as consequence of the elevated thermal energy that may affect the nanotube/substrate interaction. For example, at the high temperatures at which the reaction takes place hydroxyl groups may be formed on the surface as a result of dissociation of precursors (such as ethanol) and inert species (such as water). It is expected that he oxygenated termination of the silica surfaces may probably enhance the adsorption energies. Moreover, species in the gas phase not only interact with the substrate. Experimental works have demonstrated that strong reacting atmospheres rich in air and water can induce oxygen doping of carbon nanotubes.[170] Semiconducting nanotubes, such as the SWCNT (7,0) studied here, can switch from n-type to p-type semiconductor as a result of charge transfer-induced phonon renormalization by oxygen. [170,171] The acceptor nature of the nanotube may then further enhance its interaction with the surface.

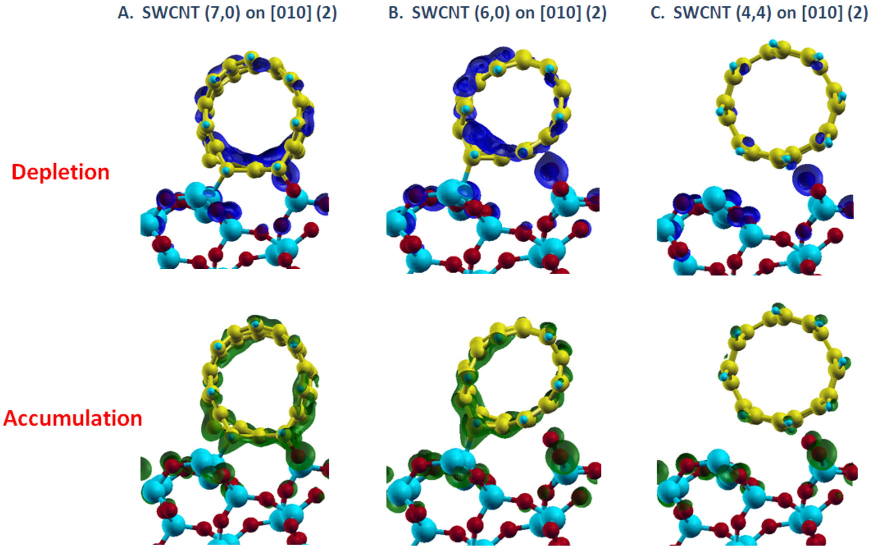

Figure 7.5. Charge density difference analysis on the [010](2) position for the three nanotubes. This position produced the strongest and the weakest adsorption energy, as shown in Figure 7.2. The charge density difference is depicted in green. In the top images, such green regions correspond to electron depletion, whereas in the bottom images, the green regions correspond to accumulation. Color codes for the atoms as in Figure 7.1.

7.4.3 Electronic density of states

In order to elucidate the electronic basis of the preferential zigzag adsorption, additional DFT analyses were performed based on the electronic density of states (DOS). A single ionic step was calculated increasing the number of grid points in the density of states to 2000 and doubling the Monkhorst pack grid for Brillouin zone integration to 12x12x1. The electronic density of states was calculated before and after adsorption and analyzed separately for carbon atoms and atoms belonging to the two upper layers of the substrate. Figure 7.6 summarizes the change in the spin resolved electronic density of states of the s and p-orbitals for the three nanotubes along their respective preferred adsorption directions. Due to the finite size of the nanotubes in our study, the calculated electronic DOS for the three nanotubes differs slightly from typical DOS reported for SWCNTs. Electronic states concentrate within narrow energy ranges near to energetic minima of neighbor subbands. This produces discrete peaks that resemble *van Hove* singularities. Despite the fact that our nanotubes can be considered as molecular systems, useful information can be assessed from their electronic density of states. For SWCNTs (7,0) and (6,0) (Figures 7.6A and 7.6B, left), electronic population is observed right below the Fermi level, whereas in the nanotube (4,4) the highest occupied molecular orbital (HOMO) is found at the calculated Fermi level, while leaving a gap of ~1 eV with the lowest unoccupied molecular orbital (LUMO) (Figure 7.6C, left). It is worthy to note that the SWCNT (4,4) is the only nanotube presenting symmetry in electronic population of the p-up p-down electronic orbitals, which indicates lack of spin polarization for this nanotube before adsorption. However, after adsorption of the armchair nanotube, as a result of interaction with the support and transfer of charges to the interface, the DOS shows a spin-polarized pattern. Discrete inner core states become highly populated, whereas the spin-polarized population near to the Fermi level is slightly modified.

Similarly, after adsorption of the nanotube (6,0) along its preferred adsorption direction, the electronic states in the inner core turn into a continuum population as a result of orbital hybridizations between nanotube and support (Figure 7.6B, right). The high peak in the vicinity of the Fermi level (Figure 7.6B, left) disappears after adsorption as a result of the oxidation of the lower half of the nanotube as described in Figure 7.5B. This kind of charge transfers are also manifested in the DOS of the SWCNT (7,0) adsorbed along the [010](2) direction (Figure 7.6A) where the two peaks near to the Fermi levels are reduced due to the strong interaction with the substrate. Hybridization of the core electrons is also evidenced.

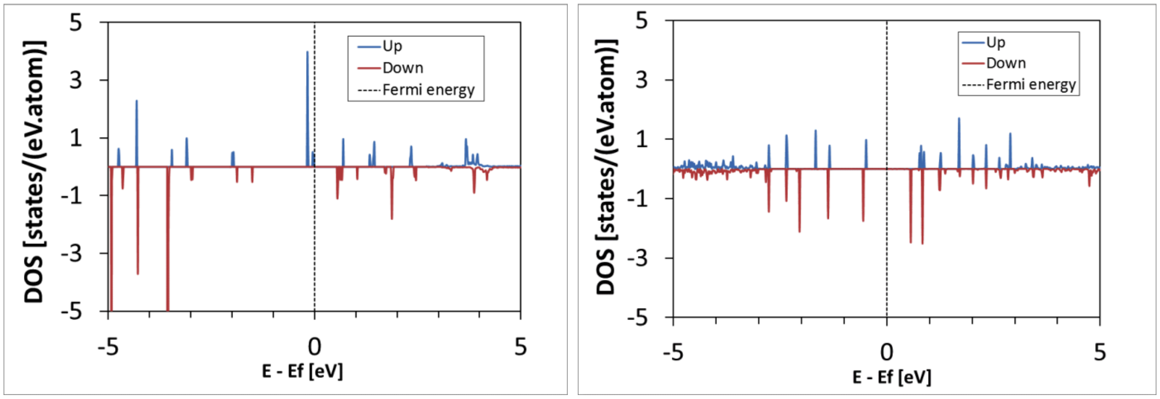

(a) (7,0) on [010](2)

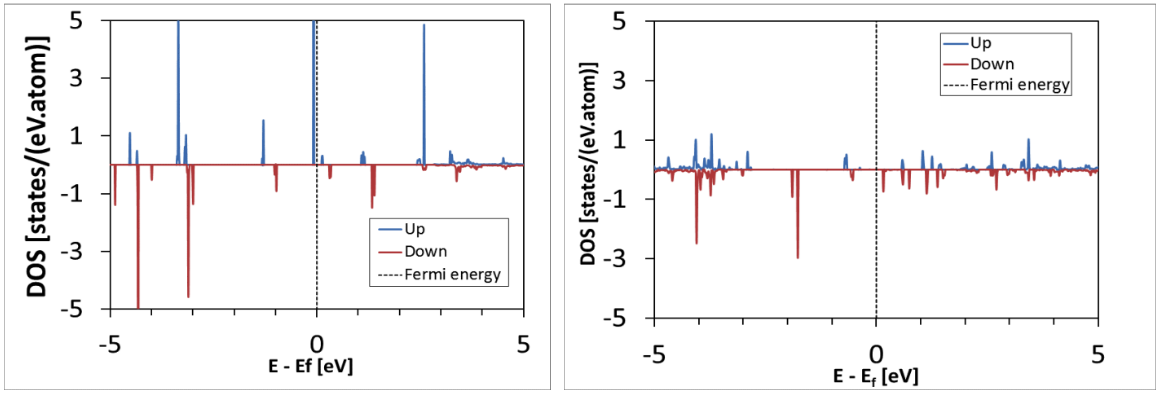

(b) (6,0) on [110]

Figure 7.6. Electronic density of states for carbon nanotubes along their preferred adsorption directions. a) SWCNT (7,0) along [010](2), b) SWCNT (6,0) along [110], c) SWCNT (4,4) along [110]. Analysis before (left) and after (right) adsorption on ST-cut surface of quartz.

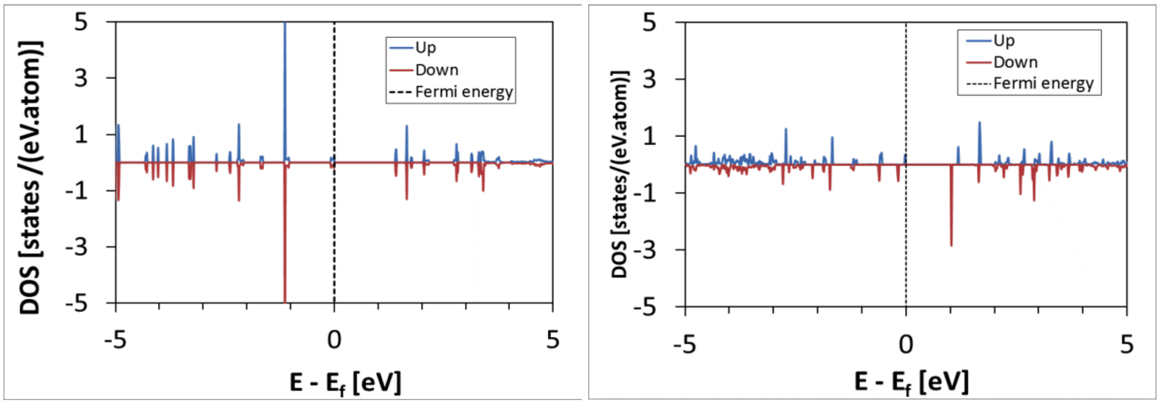

(c) (4,4) on [110]

Figure 7.6. Continued.

The electronic density of states for the atoms on the two upper layers of the substrate is also analyzed. Unlike the DOS for nanotube carbon atoms, the DOS of silicon-oxygen atoms do not vary significantly after adsorption, respect to the clean surface (Figure 7.7A). When the nanotubes adsorb along their lowest energy directions, the occupation of states near the Fermi level is only slightly perturbed (Figures 7.7B- 7.7D). The DOS of the clean surface shows a very low orbital occupation near the Fermi level.

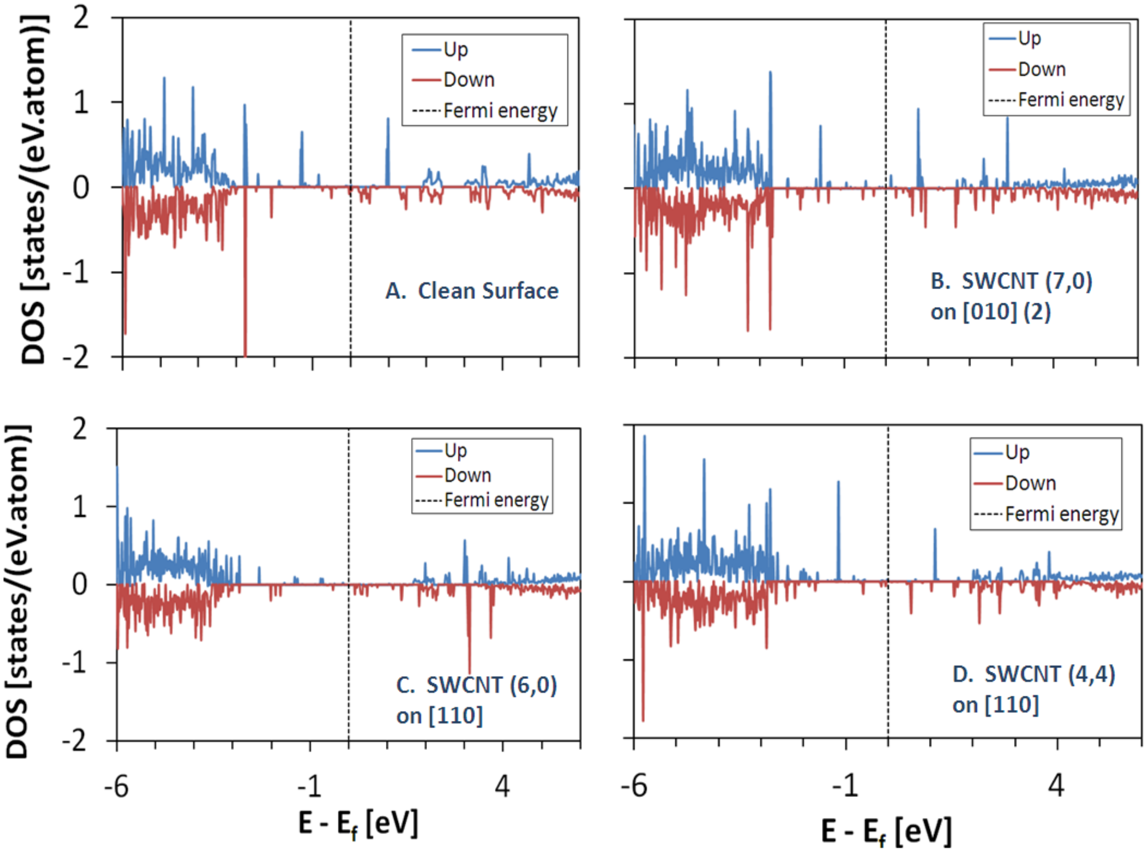

Figure 7.7. Electronic density of states of atoms belonging to the two uppermost layers of the substrate for a) clean surface, and surface after adsorption of b) SWCNT (7,0) along [010](2), c) SWCNT (6,0) along [110], d) SWCNT (4,4) along [010].

7.5 Conclusions

Density functional theory analyses of the structure, electronic density of states, and charge density at the interfacial region provide valuable information that suggests an enhanced affinity between zigzag tubes and the ST-quartz substrate. Among the nanotubes studied, the strongest adsorption energy is found for the (7,0) nanotube along the [010] direction, parallel to the y-axis. Such strong adsorption of the (7,0) nanotube is driven by silicon-carbon and oxygen-carbon interactions along the [010] direction. Charge analysis demonstrates the role of oxygen atoms on the partial oxidation of nanotube atoms closest to the substrate. Interestingly, the armchair (4,4) nanotube shows the weakest adsorption energy along the same [010] direction, suggesting that the nanotube electronic band structure is a key factor on the preferential adsorption of zigzag tubes found in these surfaces.

DOS analyses before and after adsorption demonstrate that the surface may in some cases induce spin polarization on the adsorbed nanotube, and in other cases changes in the electronic density of core and valence electrons due to electron transfer between nanotube and surface. In particular, modifications of DOS at the Fermi level resulting from interactions with the support may induce electronic behavior in the adsorbed nanotubes which differs from that of the not adsorbed tubes. This change needs to be taken into account when interpreting the experimental readings of density of states and band gaps in supported nanotubes. Overall, this study suggests that the existence of enhanced carbon nanotube/substrate interactions may be responsible for the semiconducting selectivity experimentally observed on SWCNTs horizontally grown on quartz substrates. Therefore, further investigations are needed in this direction.

8. ENGINEERING PREFERENTIAL ADSORPTION OF SINGLE-WALLED CARBON NANOTUBES ON FUNCTIONALIZED ST-CUT SURFACES OF QUARTZ*

8.1 Summary

Horizontal alignment during synthesis of single-walled carbon nanotubes has been found experimentally along certain directions of well-defined quartz surfaces. The reasons for such alignment are here examined using first-principles computational analysis, as a function of structure and chemistry of the specific exposed facet, presence and location of OH and H functional groups, and degree of hydration of the surface. It is found that selective functionalization of low-coordinated surface sites may cause exposure of low-coordinated Si atoms that bond strongly to nanotube walls. On the other hand, saturation of low-coordinated oxygen also favors carbon nanotube adhesion to the substrate. As found previously on bare silica surfaces, a chirality preference is confirmed on functionalized surfaces towards *zigzag* over *armchair* nanotubes. Magnetization effects on the surface originated by the presence of adsorbed functional groups are found to enhance adsorption of arm-chair nanotubes compared to that on clean surfaces. Based on the findings, it is suggested that surfaces may be engineered to favor horizontal adsorption of specific chiralities along preferential directions.

8.2 Introduction

Carbon nanotubes arose into the scientific spotlight in 1991[1], and since then they have been the focus of numerous studies aiming to characterize them mechanically and electronically. These novel materials have shown excellent mechanical, electronic, and optical properties that led them to meet performance standards required for various technological applications.[5-7] Among their potential high technology applications, field

---

* Reprinted with permission from Juan C. Burgos and Perla B Balbuena. "Engineering Preferential Adsorption of Single-Walled Carbon Nanotubes on Functionalized ST-cut Surfaces of Quartz." ACS Applied Materials & Interfaces **6**(15): 12665-12673.Copyright 2014, American Chemical Society.

effect transistors are devices in which single-walled carbon nanotubes (SWCNTs) may satisfy performance demands due to their outstanding thermal conductivity, mobility, and mechanical stability [172-174]. Nevertheless, two main drawbacks prevent carbon nanotubes achieving high performance in field effect transistors: the *lack of chirality selectivity and alignment* on dielectric substrates during growth. Chirality is the structural variable that defines carbon nanotubes electronic band structure, and it is perhaps the most difficult property to be controlled during chemical vapor deposition (CVD) synthesis, in spite of significant advances in this field [13,14,24]. While researchers continue investing significant efforts on finding reliable methods to produce bundles with homogeneous chiralities, the alignment of SWCNTs in the bundle remains an issue obstructing the development of fully functional SWCNT-based electronic devices.

Experimental strategies have been proposed to guide nanotubes along specific directions on insulator substrates such as silicon oxide. Liu and coworkers [27] achieved growing of horizontally aligned SWCNTs on the stable temperature cut (ST-cut) surface of quartz, whose crystallographic plane was identified as the $(01\bar{1}1)$ by X-ray diffraction techniques.[175] The approach consisted on patterning the quartz surface by drawing parallel lines of catalyst nanoparticles from which carbon nanotubes grow.[27] Through this method, SWCNT root growth was favored over tip growth, while surface diffusion and collision of catalyst particles were suppressed. The absence of catalyst sintering and Ostwald ripening led to high density of horizontally aligned carbon nanotubes with narrow diameter distributions. Liu and coworkers[27] attributed nanotube bending during growth to an increase in catalyst and nanotube diameters and the consequent loss in preferential epitaxial interactions along the x-axis of the ST-cut surface, which has monoclinic unit cell (Figure 8.1). Conversely, other authors have concluded that the bending angle, which may be observed in the growth direction, is directly related to the angle of the O-Si-O segments of the quartz surface.[175] Liu et al. later determined that the direction of alignment was exclusively governed by epitaxial interactions between the outer shell of carbon nanotubes and the catalyst support surface,[176] although surface annealing may be critical on enhancing horizontal alignment of carbon nanotubes.[175] Moreover, our recent density functional theory (DFT) calculations demonstrated that patterns delineated by silicon and oxygen atoms along the [010] direction establish the strongest adsorption energy for zigzag nanotubes, and the weakest for armchair nanotubes.[177] This suggests that the nanotube electronic band structure is a key factor on the preferential adsorption of carbon nanotubes. We thus demonstrated that patterns delimited by silicon and oxygen atoms guide growing nanotubes along preferential directions via specific electronic interactions. However, our earlier study neglected the presence of different species in the feedstock gas phase that may functionalize unsaturated silicon and oxygen atoms on the surface topmost layer, therefore altering preferential growth directions.

Water, methanol, ethanol and other alcohols are some of the precursor and inert compounds fed into CVD reactors to grow carbon nanotubes. These species tend to release OH radicals and hydrogen into the system. The effect of OH radicals from alcohol and water dissociation has been extensively reported as a factor enhancing the semiconducting selectivity and SWCNTs density.[24,26] The nanotube selectivity has been commonly attributed to selective etching of metallic tubes based on observations of reduced density of SWCNTs grown on ST-cut quartz and the lower ionization potential of the metallic nanotubes that makes them vulnerable in oxidative environments.[24,26] Nonetheless, alignment has not been associated to the presence of OH radicals on the system, although it is known that products of water dissociation can hydrate, hydrogenate or hydroxylate surfaces modifying their reactivity towards adsorbates.[178] Even in the case of no dissociation, water molecules can alter the adsorption behavior of adsorbates on a surface.[179] In this study, we present a detailed DFT analysis of the effect of quartz surface functionalization on the horizontal alignment and chiral preferences on nanotube adsorption. New insights allow us to suggest directions towards engineering quartz surfaces to achieve preferential alignment of specific chiralities.

8.3 Computational methods

DFT calculations were carried out using the Vienna ab initio simulation package (VASP) [180,181]. The code describes electronic interactions by the projector-augmented (PAW)[182] method, which is expanded within plane wave basis sets. Only plane waves with kinetic energies below 400 eV were included in the basis set. The Perdew-Burke-Ernzerhoff (PBE) exchange model[47], which is a generalized gradient approximation (GGA) function, was employed to describe the electron exchange and correlation effects. Because of the semiconducting and insulating character of the system, the partial occupancies were set to each orbital following the tetrahedron method with Blochl corrections [183]. The smearing width was established in 0.1 eV. Convergence criteria were set to $1x10^{-4}$ and $1x10^{-3}$ for electronic and ionic minimizations, respectively, whereas a 5x5x1 Monkhorst pack grid [47] was used for the Brillouin zone integrations carried out over the system. For the DOS calculations, a single ionic step was performed increasing the Monkhorst pack grid for Brillouin zone integration to 10x10x1, and increasing the number of grid points in the density of states to 2000.

After an exhaustive literature review, we have established the thermodynamic phase and the crystallographic plane corresponding to the ST-cut surface of quartz at growth conditions. The ST-cut quartz was identified as the $(01\bar{1}1)$ crystallographic plane of the β-quartz, which lies at 42° from the y-axis approximately. Detailed information about the Miller indices selection can be found in our previous report.[177] This surface was chosen for our DFT calculations because of its remarkable selectivity and capability for induction of alignment, which have been observed experimentally when nanotubes grow horizontally on this type of substrate. We constructed our surface using the surface cleavage tool of the Materials Studio package[164]. The surface was modeled using a 1x2 supercell with 4 layers of thickness and 15 Å vacuum (Figure 8.1A). Each layer is composed by 6 Si atoms and 12 O atoms, which keep the stoichiometric relation of silica. Low saturated Si and O atoms in the topmost layer of the surface were targeted for saturation with hydroxyl radicals (*OH) and hydrogen atoms (H), respectively. Different combinations resulted in different OH terminations and concentrations on top layer of the surface (Figures 8.1B, 8.1C, 8.7C (inset), and 8.8B). Three different SWCNTs were optimized and placed on top of the surface along different directions. SWCNTs (4,4), (6,0) and (7,0) with finite lengths were fit in the unit cell and saturated with hydrogen atoms at the open edges (Figure 8.1D) to minimize the effect of the dangling bonds. The molecular formulae for SWCNTs (4,4), (6,0) and (7,0) correspond to $C_{40}H_{16}$, $C_{36}H_{12}$ and $C_{42}H_{14}$, respectively. Electronic band structure calculations of SWCNTs have shown that all armchair nanotubes are metallic, whereas zigzag nanotubes are semiconductors with a band gap width dependent upon their chiral indices (n,m)[2,3]. With the selection of our three nanotubes, we are considering three possible electronic behaviors. SWCNT (4,4) is metallic ($n – m = 0$). Chiral indices (7,0) correspond to a semiconducting tube with a moderate band gap ($n-m \neq 3k$, $k=1,2,3,...$). The remaining zigzag tube (6,0) is a narrow-gap semiconductor ($n-m = 3k$, $k=1,2,3,\ldots$), although it has been found to be metallic because of hybridization of σ^* and π^* orbitals that results from the tube small diameter.[184] In total, 6 positions corresponding to 4 crystallographic directions were tested for each nanotube (Figure 8.1B). The 18 calculations (3 nanotubes on 6 positions) were made for each one of the four surface terminations.

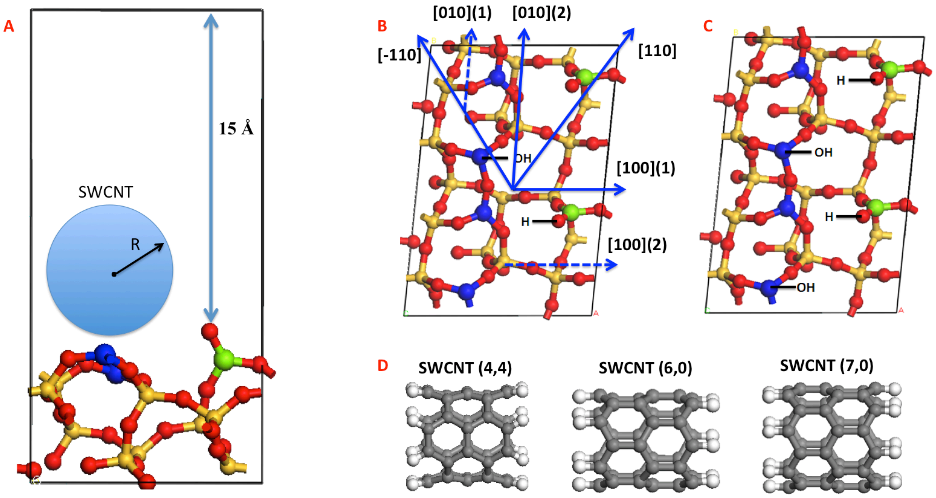

Figure 8.1. ST-cut surface of quartz, which corresponds to the (01 $\bar{1}$ 1) plane of the hexagonal lattice. A. Side view. Blue atoms: unsaturated Si atoms, yellow: saturated Si, red: O atom, and green: unsaturated Si bonded to unsaturated O. The distance between the unsaturated oxygen and the top of the cell gives the vacuum, calculated as 15Å. Nanotubes with diameter 2R are fit within the cell. The diameters are 5.43 Å, 4.70 Å and 5.48 Å, for SWCNTs (4,4), (6,0) and (7,0), respectively B. Top view for the *monohydrated* surface. Four directions indicated by solid blue arrows. The dashed blue arrow indicates parallel positions along *x*: [100](2) and *y:* [010](1) axes. C. Top view for *di-hydrated* surface. D. Three finite length nanotubes placed on the surfaces.

8.4 Results and discussion

8.4.1 Water dissociation on silica surfaces

Water is one of the non-reactive species added in a CVD process together with inert gases such as argon or helium. At SWCNT synthesis conditions (~1000 K and moderate pressures close to 1 atmosphere), high kinetic energy water molecules are found in vapor phase. As a part of the gas phase mixture, although it does not participate on the reaction directly, water can interact with carbon precursor molecules, catalyzed carbon from the nanotube, metal atoms from the catalyst or atoms on the surface of the catalyst support. Both, metallic surfaces and silicon oxide surfaces have shown to catalyze the dissociation of water molecules into hydroxonium and hydroxyl ions. [185-191] Reaction pathways and energy landscapes have been detailed.[192] *ab* initio molecular dynamics (AIMD) simulations of a water molecule over quartz (100), (110), and ST-cut surfaces were carried out at 1000 K. AIMD simulations were performed following the Born-Oppenheimer procedure to describe the classical motion of ions, as implemented in VASP. As in the case of relaxation of SWCNTs on quartz, the GGA-PBE functional was used with a plane wave energy cut-off of 400 eV. The time step was set to 1 femtosecond, and the systems were allowed to run enough time until water molecules dissociated or moved away from the substrate; this step corresponded to ~300 fs. The canonical ensemble with the Nosé algorithm to control the frequency of temperature oscillations was used. The Nosé-mass parameter was set to 0.5. Because of the high temperature and associated high kinetic energy and the very low water density, the water molecule rarely interacts with the studied surfaces, except for the case of quartz (110), where a water molecule dissociates on the substrate topmost layer due to the presence of low coordinated surface atoms (Figure 8.2). The AIMD simulations reveal a mechanism by which water molecules are dissociated on a silica surface. SiO_2 (quartz) (110) surfaces have both unsaturated O and Si atoms. The Si-O bond has a covalent component that has been estimated in 50%, although the ionic character increases in detriment of the covalent component when the coordination of atoms decreases.[193] Hence, the water molecule dissociates on the quartz (110) surface as a consequence of a proton transfer from water to a negatively charged low coordinated O atom of the top layer. Once the proton is attached to this oxygen, no further surface atomic diffusion was evidenced. Meanwhile, the released OH ions diffuse through the surface until they attach strongly to low coordinated Si atoms at the topmost layer, creating Si-OH surface terminations.

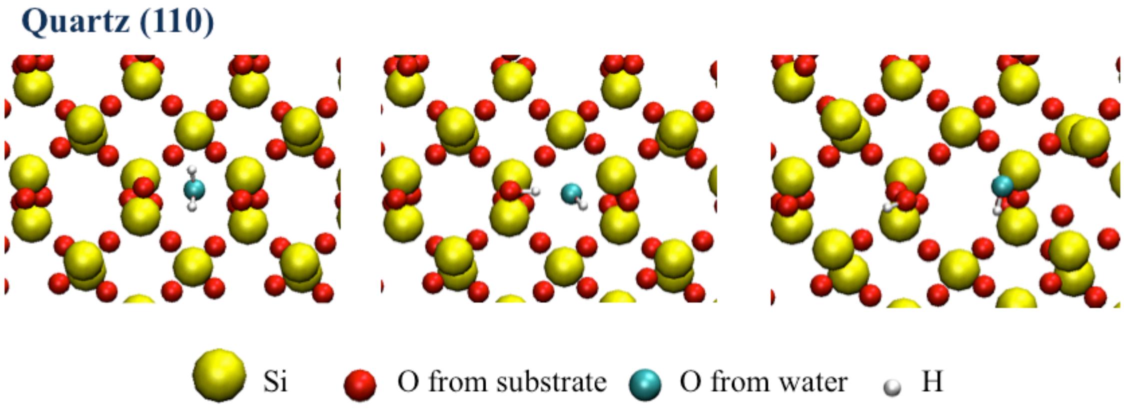

Figure 8.2. Water dissociation mechanism on quartz (110). Hydronium ion transfers to low coordinated O at the top of the surface. Hydroxyl ion migrates until finding an unsaturated Si atom and forming a Si-OH bond.

Based on the AIMD results, DFT simulations were carried out on ST-quartz surfaces functionalized with water dissociation products. We assume that this dissociation should also occur on the ST-cut surface of quartz since all silica surfaces studied share similar terminations with unsaturated Si and O atoms. Based on the concentration of unsaturated oxygen atoms in the surface unit cell, two water molecules represent the maximum capacity of the surface to chemisorb water through dissociation, proton transfer, and saturation of low coordinated atoms. Therefore, one and two molecule(s) represent water concentrations of 50 and 100%, respectively. di-hydrated surfaces is then the maximum concentration of water products per surface area.

A total of six surface low-coordinated Si atoms were identified, four at the top layer and (blue atoms in Figure 8.1) two at the subsurface (green atoms in Figure 8.1). Two low-coordinated surface O atoms are bonded to low-coordinated Si in the subsurface, as shown in Figure 8.1A. Thus, functional groups can saturate these atoms and define surface terminations with different OH concentrations and locations.

8.4.2 Adsorption of SWCNTs on the hydrated surfaces

SWCNTs (4,4), (6,0) and (7,0) (Figure 8.1D) were deposited along six different directions of the *mono-hydrated* (one water molecule per unit cell) and *di-hydrated* (two water molecules per unit cell) surfaces (Figure 8.1) separated from the top periodic image by a vacuum space of 15Å (Figure 8.1A). Figure 8.3A shows for a *mono-hydrated* surface similar trends to the ones reported previously for clean surfaces[177]. The (4,4) armchair tube is not energetically favored for alignment along any direction. The metallic character of this tube and the significant differences in adsorption energy with respect to zigzag tubes, make evident the existence of an effect of the substrate on the preferential deposition of semiconducting tubes. In contrast, zigzag tubes were clearly favored to adsorb on the mono-hydrated surface of quartz, although SWCNTs (6,0) and (7,0) did not align preferentially along the same direction. For the case of the SWCNT (7,0), the direction parallel to the [010](2) *y*-axis was found to be the direction of strongest adsorption energy. Along this direction, nanotubes with a diameter within the range of the three nanotubes studied (~5 Å) were exposed to close interactions with low-coordinated Si and O atoms. It is worth to note that this direction represented the strongest overall adsorption energy on the clean (*non-hydrated*) ST-cut surface of quartz.[177] In the hydrated surfaces, low saturated sites along that direction become saturated with products of water dissociation, i.e. having OH terminations side by side of the [010](2) direction (Figure 8.1B).

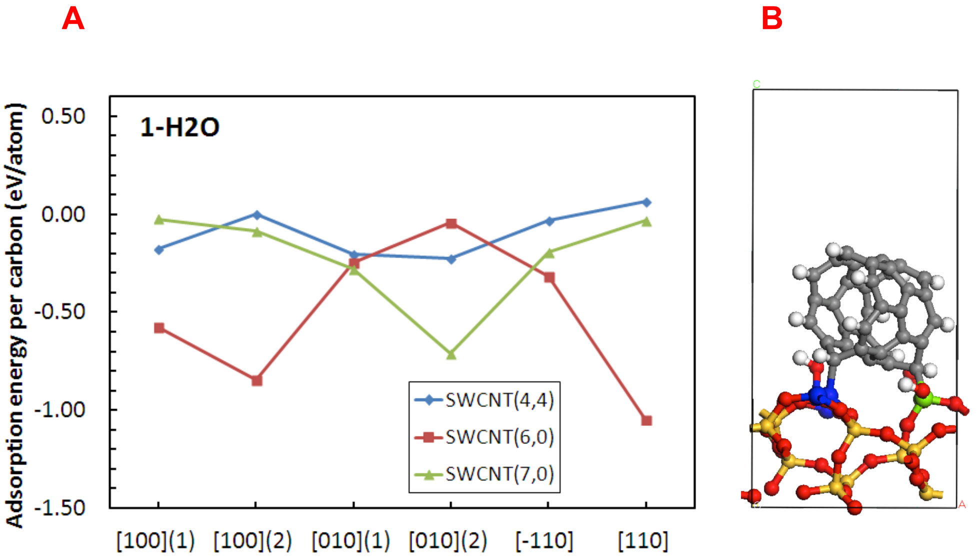

Figure 8.3. A. Adsorption energy per carbon atom in contact with surface for three different nanotubes on the *monohydrated* surface (top view in Figure 8.1B). The values are calculated along six surface directions. B. Scheme representing the SWCNT(6,0) along the preferred [110] direction.

It is also remarkable that the nanotube (6,0) undergoes a very weak attraction along the same *y* direction. The nanotube (6,0) has a smaller diameter than the (7,0), which places it in disadvantage respect to the (7,0). This is because the [010](2) direction is characterized by having a channel delimited by low-coordinated Si atoms at the topmost layer and the subsurface. A nanotube with a larger diameter is able to reach the effect of low-coordinated Si atoms at *both* sides of the channel. On the other hand, semiconducting (7,0) and metallic (4,4) have very similar diameters but different adsorption strengths on this direction, which confirms that the *electronic behavior of each nanotube defines its adsorption preferences*.

Figure 8.3A also illustrates that (6,0) adsorbs preferentially along the [100](2) *x*-axis and on the [110] direction. Along these directions, the epitaxial interaction between the nanotubes (6,0) and the silica surface allows the nanotube (6,0) to maximize its contacts with unsaturated Si atoms at the subsurface (green atoms in Figure 8.3B), sometimes even repelling OH functional groups attached to them, as shown in Figure 8.3B. Thus far, the results indicate that preferential adsorption is driven entirely by epitaxial interactions between C atoms and low-coordinated Si at the surface, suggesting that OH and O terminations play a minimal role. The effect of higher surface concentration of OH functional groups was analyzed on *di-hydrated* surfaces (two water molecules per unit cell), as shown in Figure 8.1C. The results in Figure 8.4 indicate a similar adsorption pattern to that in Figure 8.3.

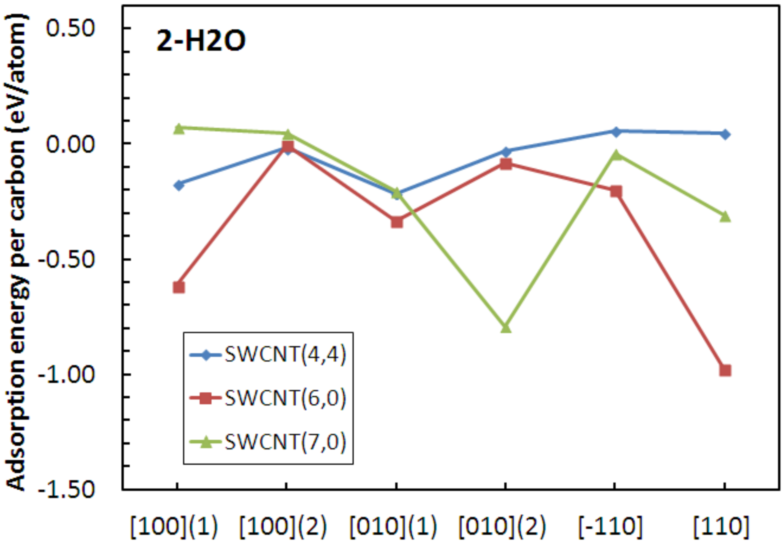

Figure 8.4. Adsorption energy per carbon atom in contact with the surface for three different nanotubes on the *di-hydrated* surface. The values are calculated along six surface directions.

The only significant difference lies in the adsorption energies when the nanotube (6,0) is deposited on the [100](2) direction. This result is expected because the [100](2) direction is the only one where the concentration of OH terminations can be changed along the path where the tubes adsorb. Thus, the adsorption energy of the SWCNT (6,0) on the [100](2) direction is shifted from a moderately strong adsorption in the monohydrated surface to a null, almost repulsive interaction when additional OH functional groups saturate these surface sites in the di-hydrated case. The reasons for this difference could be purely steric, or otherwise electronic. The steric argument would be valid if the OH group obstructs C atoms to access low-coordinated Si atoms at the subsurface. However, it has been observed that OH groups tend to be flexible when bonded to unsaturated Si (green atoms in Figure 8.1C), which allows deflection of the OH group and grants access of C atoms to interactions with unsaturated Si atoms. In contrast, the extra OH group in the nanotube path ([100](2) direction) saturates a Si atom *at the surface* (blue atoms in Figure 8.1C), stabilizing the Si via formation of a stiff (non-flexible) Si-OH bond. Consequently, the steric explanation can be disregarded, and the change in the chemical character of a Si atom at the topmost layer of the surface remains as the only factor disrupting the adsorption trends from monohydrated to di-hydrated surfaces. This result is strong evidence indicating the *importance of Si atoms on defining preferential directions of alignment of nanotubes on a silica substrate*. Therefore, the effect of OH radicals on the adsorption on quartz surfaces relies on modifications to the chemistry of Si surface atoms, rather than on physical constraints due to changes on the surface topology. It is important to remark that a moderate hydration (defined here as mono-hydrated surface) of the ST-cut surface increases significantly the preferential alignment of nanotubes towards directions parallel to the x-axis, respect to the clean surface, as seen by comparing Figure 8.3A with Figure B4 in the supporting information (appendix B). SWCNT (7,0), however, remains favoring the y-axis for adsorption no matter the degree of hydration. We note that the results in Figures 8.3 and 8.4 do not include surface dipole corrections. To verify the effect of this correction on the adsorption energies, we repeated the calculations and the results are reported in Figures B5 and B6. The results indicate that there is a small change in the adsorption energies that become ~0.1 eV weaker when surface dipole corrections are included, however the trend discussed in Figures 8.3 and 8.4 is kept.

In order to confirm our hypothesis of Si atoms governing the alignment of carbon nanotubes along specific directions, a charge density mapping was performed for selected cases. From previous work[177] it is known that the strongest adsorption energies are characterized by a high population of charges at the interface between nanotubes and the silica support. For the monohydrated surface along the [100](2) direction, only the SWCNT (6,0) exhibits significant concentration of charges, up to 0.7 e/Å^3 at the interface between carbon and silicon atoms. SWCNTs (4,4) and (7,0) do not exchange charges at the interface, not even over unsaturated Si atoms, which suggests a correlation between the nanotube electronic properties and their ability to carry charges towards the interface (Figure 8.5A). Moreover, the strongest adsorption energy on the monohydrated surface was observed for the SWCNT (6,0) along the [110] direction. This direction has the uniqueness of facilitating formation of two C-Si bonds along the nanotube path (Figure 8.3B), which allows concentrating charges at the interface in the order of 0.8 - 1.0 e/Å^3. Figure 8.5B shows the repulsion that causes the deflection of the OH functional group bonded to the unsaturated Si. The flexibility of this Si-OH bond allows a direct charge transfer at the interface between unsaturated Si and C atoms, as seen in Figure 8.5B. On the di-hydrated surface, charge density maps along the *y-axis* shows how the SWCNT (7,0) reaches Si atoms on both sides of its path thus maximizing charge sharing at the interface (Figure 8.5C).

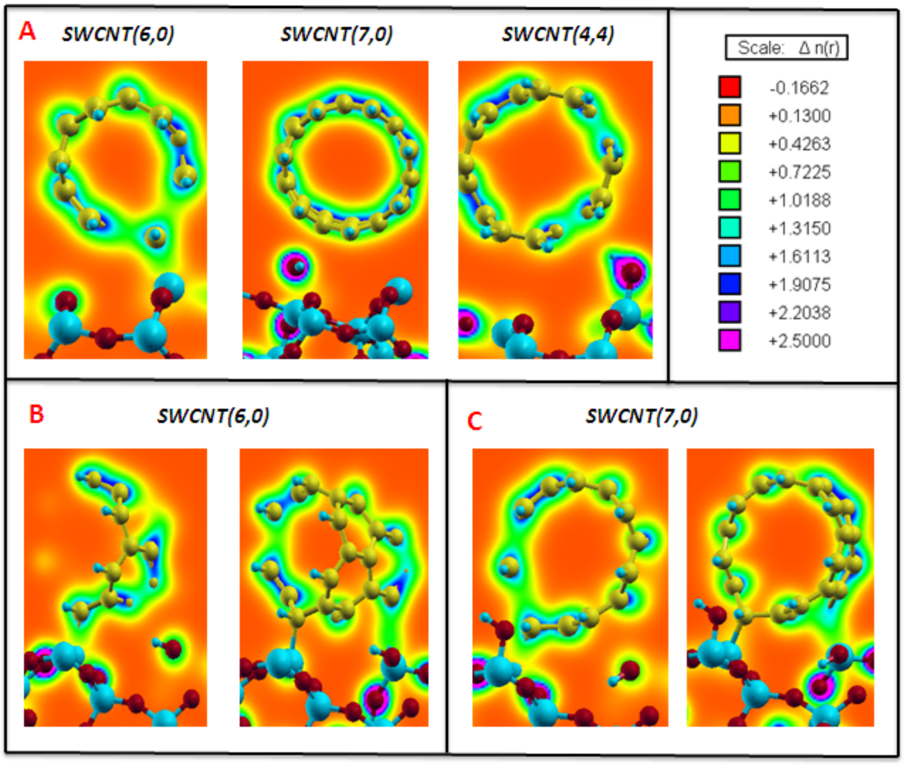

Figure 8.5. Charge density mapping for A. SWCNT (6,0), (7,0) and (4,4) along [100](2) of the monohydrated surface, B. SWCNT (6,0) along [110] of the monohydrated surface, C. SWCNT (7,0) along the y-axis [010](2) of the di-hydrated surface. The color chart displays ranges of charge densities in e/Å^3.

DFT analysis shows that nanotubes strongly adsorbing on the ST-cut surface of quartz experience structural deformations that led C atoms to reach points of interaction with near-surface low-coordinated Si atoms. Furthermore, adsorption along preferential directions sometimes demands certain amount of surface reconstruction. OH functional groups deflection along the path of the nanotube may induce low-coordinated Si atoms located at lower surface planes to diffuse towards higher locations on the surface and interact with C atoms from the nanotube, as shown in appendix B (Figure B1).

Along a given direction, nanotubes with similar diameters adsorb with different strengths on clean and hydrated surfaces. A general scenario of depletion and accumulation of charges before and after nanotube adsorption provides insightful information about the repulsive/attractive nature of each interaction and the migration of charges upon adsorption. Charge depletion and accumulation were computed for an isosurface value of 0.8 e/$Å^3$ for nanotubes along the [100](2) direction of the monohydrated surface. These results confirm the repulsion experienced by the (4,4) tube as charges are depleted at the interface and accumulated inside the nanotube, as seen in Figure 8.6A. In the top half of the (4,4) nanotube, charges are also displaced in the positive direction of the z-axis. This overall charge shift in the SWCNT (4,4) denotes a strong repulsion undergone by the nanotube after contact with the surface that results in a displacement of carbon nuclei away from the surface. In contrast, SWCNT (6,0) shows the strongest adsorption energy along the same direction of the monohydrated surface, and allows a significant charge accumulation at the interface. This is shown in Figure 8.6B, also illustrating electron depletion at the inner part for the lower nanotube half, as well as accumulation in the inner and depletion in the outer part of the upper half of the nanotube wall.

Electron cloud depletion at the interface was occasionally observed for hydrated surfaces, unlike the behavior on clean surfaces. Localized migration of charges away from the interface combined with accumulation at Si-C connections, are a result of structural deformation of strongly adsorbed nanotubes. As a consequence of these deformations, nuclei might move away from the surface at specific locations, such as stiff OH functional groups, and approach lower energy spots such as unsaturated Si sites. Therefore, simultaneous electron depletion *and* accumulation is observed at different points of the interface, as shown in Figure 8.6C for the (6,0) tube along the [110] direction of the di-hydrated surface.

This analysis allows us to conclude that low-coordinated Si atoms guide preferential alignment of carbon nanotubes on the ST-surface of quartz. It was previously reported[177] that unsaturated O atoms at the surface were critical on defining preferential alignment through partial oxidation of nanotubes. However, here we demonstrate that if the low-coordinated O is bonded to low-coordinated Si, as in the case of the ST-cut, the unsaturated Si is most likely to cause the attraction and charge concentration at the interface. We believe these results can be extended to any kind of silica surface no matter the spatial arrangement of atoms within the lattice. Only the coordination states of the Si and O atoms will define the adsorption strength of carbon nanotubes on the surface, and therefore, the surface concentration and distribution of this kind of atoms will establish the directions of preferential alignment.

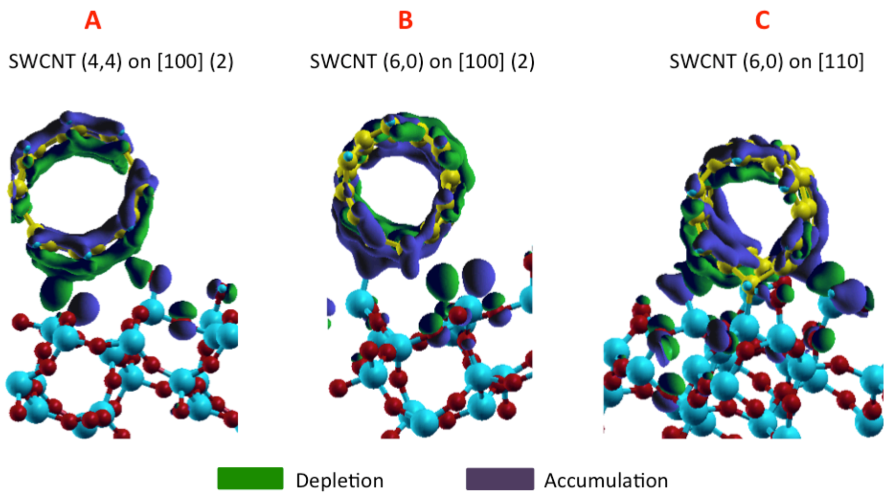

Figure 8.6. Charge density difference analysis for three different cases. A and B correspond to cases on the monohydrated surfaces. C corresponds to a case on the di-hydrated surface.

8.4.3 Adsorption and surface magnetization

Preferential adsorption of finite length *zigzag* SWCNTs on clean quartz surfaces was associated to asymmetric population of spin up and down states (spin polarization), not observed in finite length *armchair* nanotubes.[177] The asymmetry in the electronic spin states of zigzag tubes adsorbed on a clean surface, and their magnetic moments suggest a possible magnetic dipolar interaction between tubes and surfaces. Here the electronic density of states (DOS) was calculated before and after adsorption and analyzed only for carbon atoms (H atoms and atoms Si and O belonging to the substrate were not included). The supporting information (appendix B) shows the spin-resolved DOS for the s and p-orbitals of each nanotube along the [110] (2) direction of mono-hydrated (Figure B2) and the [110] direction of the di-hydrated (Figure B3) surfaces. DOS results are in agreement with previous results for finite length tubes on clean ST-cut surfaces.[177] Electronic states occupying narrow energy ranges that resemble van Hove singularities were observed. Furthermore, DOS plots showed break in the spin up/down symmetry of armchair tubes, depletion of the electronic states near the Fermi level as a result of strong interactions, and inner core states that become highly populated as a result of orbital hybridizations. Unlike preferential alignment trends, chiral preferences are not disturbed by surface functionalization with OH and hydrogen groups. However, these types of functionalizations introduce subtle modifications to the electronic DOS of surface atoms that might provide further clues on the alignment of SWCNTs. Thus, the spin-resolved DOS are plotted for atoms belonging to the two upper layers of each substrate, monohydrated and di-hydrated surfaces. The DOS of hydrated surfaces are summarized in Figures 8.7A and 8.7B, and can be compared with those for the clean surface.[177] The spin-resolved DOS plots for hydrated surfaces show higher population of electronic states at the Fermi level, compared to the clean surface. Furthermore, this relatively high density of electronic states at the Fermi level was accompanied by misbalance of spin up and spin down populations, which leads to spontaneous magnetization of the surface. The magnetic moments of the two top layers of these surfaces were computed as 0.024 and 0.022 μ_B per atom for mono and di-hydrated surfaces, respectively. It was stated above that the magnetization of the surface may favor the adsorption of zigzag nanotubes through specific magnetic dipolar interactions. In contrast, this magnetization might be disfavoring an attractive interaction between armchair tubes and silica surfaces. Armchair tubes were not able to overcome the barrier of 0.25 eV/atom of adsorption energy along any direction of these magnetized hydrated surfaces. In order to confirm this hypothesis, a surface with a very symmetrical spin down/up DOS was found by saturating two Si atoms at the top of the surface (blue atoms) with two OH radicals (Figure 8.7C, inset). The surface configuration with two

OH and two O terminations reduced the electronic population at the Fermi level to almost zero, as seen in Figure 8.7C. It also reduced the magnetic moment to 0.0014 μ_B per atom (Figure 8.7D). Interestingly, SWCNT (4,4) along the [100](2) direction of this surface adsorbed at 0.91 eV, which is the strongest adsorption observed for an armchair tube in our results.

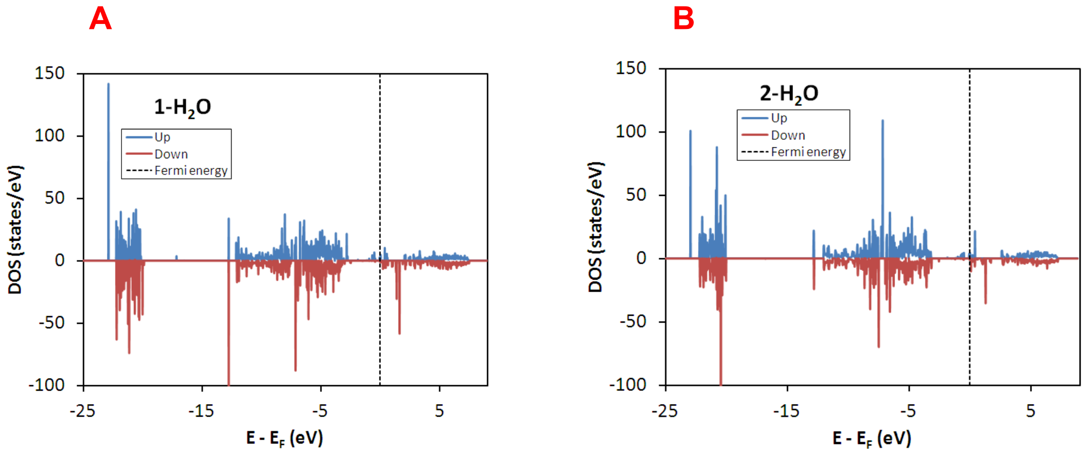

Figure 8.7. A-B Spin resolved electronic DOS of atoms belonging to the two uppermost layers of hydrated surfaces. C. Spin resolved electronic DOS of atoms belonging to the two uppermost layers of hydroxylated surface. The inset represents the unit cell of the surface with its functionalization. D. Adsorption energy per carbon atom as a function of surface magnetization and surface termination. The values reported correspond to the strongest adsorption found for SWCNT (4,4) on a given surface.

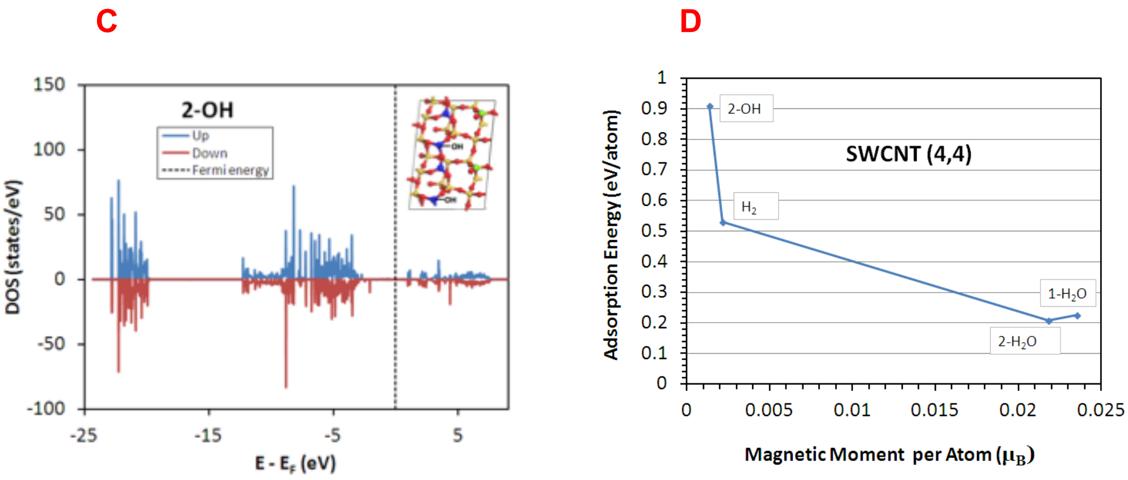

Figure 8.7. Continued.

Thus, proper functionalization may also induce preferential adsorption of specific chiralities due to electronic changes on the surface such as the suppression of surface magnetization.

8.4.4 Engineering surface functionalization.

After having a better understanding of surface properties governing preferential alignment of horizontally deposited carbon nanotubes, a window opens to engineer surfaces seeking desired directions of alignment. According to the above discussion, a substrate that maximizes the density of low-coordinated Si atoms on the surface can be thought as enhancing the strength of adsorption of zigzag nanotubes. This can be achieved in the ST-surface of quartz by selectively saturating only the O terminations on the surface. There are two low-coordinated O atoms at the topmost layer, per unit cell of surface. Saturating these two atoms would represent a scenario in which the surface is hydrogenated. Note that during SWCNT growth, atomic hydrogen may be readily available through the catalysis of C-containing precursor gases at the high temperature CVD conditions. This surface will now have six unsaturated Si atoms on the surface, with two of them holding an OH functional group each, as seen in Figure 8.8B. This would eliminate the effect of unsaturated surface O that may cause partial oxidation of nanotubes, and would create flexible OH functional groups that are susceptible to deflection in the Si-OH bond orientation. After calculating the adsorption energies for finite length nanotubes on this surface, we found the strongest overall adsorption for SWCNT (6,0) along the x-axis, as seen in Figure 8.8A. This adsorption (1.26 eV/atom) is the strongest found in this and our previous work (Figure B4) The value overcomes the ~1 eV/atom for SWCNT (6,0) on both hydrated surfaces along [110], and the 0.82 eV/atom for the SWCNT (7,0) along [010](2) of the clean surface (Figure B4). Despite the adsorption of SWCNTs (6,0) and (7,0) along the y-axis are not as strong as along the [100](1) direction, their adsorption values are close to the values reported for the clean surface, where the y-axis was the preferred direction of alignment. The SWCNT (6,0) along [100](1) direction favors the direct interaction with three of the six low-coordinated Si surface atoms, as seen from the charge mapping analysis (Figure 8.8B). The interaction with one of them is achieved through repulsion of an OH functional group and consequent deflection of the Si-OH bond. Thus, the nanotube (6,0) aligns preferentially along the [100](1) direction through the creation of silicon "hangers" that keep the nanotube stuck to the silica support. The high density of low-coordinated Si along the perpendicular direction to the nanotube axis, allows the SWCNT (6,0) to stick to the substrate side by side and upfront, as seen in Figure 8.8B. It is worthy to note that this direction was never found favorable for adsorption of any nanotube on any ST-cut surface in our previous studies. These findings are in agreement with the experimental results indicating the existence of preferential alignment parallel to the x-axis during horizontal growth.[24,175] In Liu's work,[24] methanol is added to the gas feedstock. OH radicals released from methanol were linked to the preferential etching of metallic caps and the consequent high population of semiconducting tubes. However, the OH radicals were never considered a factor for nanotube alignment along the x-axis. It should be pointed out that in the experiments performed by Liu and coworkers, a flow of molecular hydrogen is used during substrate treatment at 800°C. On the other hand, Rutkowska et al,[175] demonstrated alignment along the x-direction of the ST-cut surface of quartz. In their experiments the furnace is preheated from room temperature to 700˚C in presence of molecular hydrogen. H_2 is also part of the carbon feedstock along with CH_4.

The electronic DOS calculated for this surface evidenced reduced concentration of electronic states at the Fermi level and slight spin polarization, which gave a magnetic moment of 0.0021 μ_B per atom. Even though the SWCNT (6,0) was clearly favored for horizontal alignment on this surface, the hydrogenated surface allowed the SWCNT (4,4) to adsorb at 0.53 eV/atom along the [110] direction (Figure 8.8A). This value is stronger than the adsorption along any direction of hydrated surfaces, although it is weaker than the adsorption on the 2-OH surface. This is the inverse correlation followed by the magnetization of these surfaces, and supports our hypothesis of a trend showing decrease in armchair adsorption as the surface magnetic moment increases (Figure 8.7D).

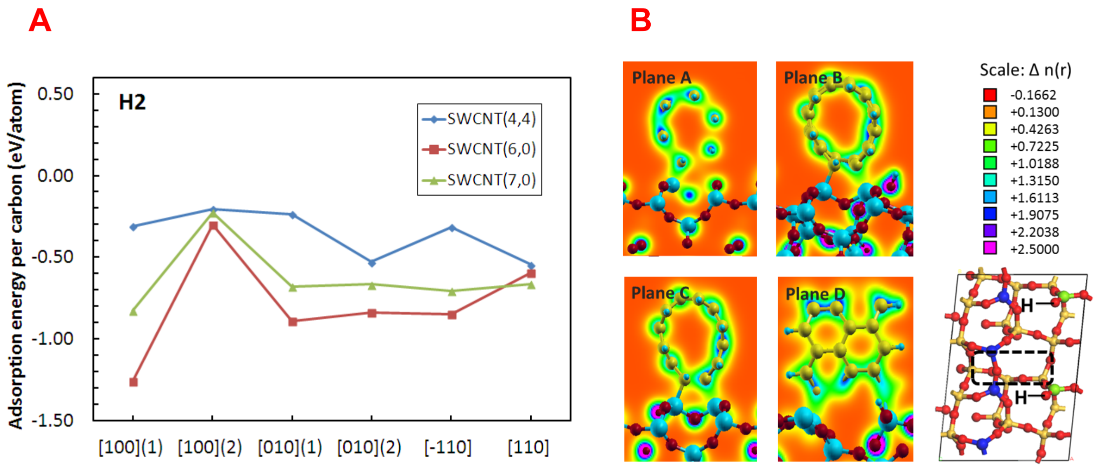

Figure 8.8. A. Adsorption energy per carbon atom for three different nanotubes on the hydrogenated surface. The values are calculated along 6 surface directions. B. Charge density mapping for SWCNT (6,0) along [100](1). Four different planes intersecting the main binding contacts are plotted. Plane D shows a lateral view that intersects two interacting spots that correspond to the same contacts of planes B and C. The dashed lines in the unit cell illustrate the approximate diameter of the (6,0) and how it interacts with three unsaturated Si atoms simultaneously. The color chart displays ranges for the charge density in e/Å^3.

We note that the nanotubes used in this report have short length. We are currently developing force fields for the interactions of carbon nanotubes with quartz surfaces which will be used in classical molecular dynamics simulations to test the effects of nanotube length and high temperatures on the nanotube/substrate adhesion properties. Preliminary results indicate good agreement between the DFT and MD results. Details will be published elsewhere.

8.5 Conclusions

DFT calculations yielded new insights into preferential adsorption of SWCNTs on quartz surfaces functionalized by water dissociation products. AIMD simulations demonstrated that water dissociation occurs on quartz surfaces producing hydrogen and OH radicals. OH radicals tend to bond low-coordinated Si atoms, whereas hydrogen saturates O atoms at the top of the surface, functionalizing the surface with OH terminations. It was demonstrated that horizontal alignment of SWCNTs on silica surfaces is governed by patterns drawn by unsaturated Si atoms at the topmost layer of silica surfaces. The saturation of O atoms with hydrogen to create OH terminations did not reduce the strength of adsorption of nanotubes. On the contrary, the strongest interactions between horizontal nanotubes and silica surfaces were observed along directions not containing unsaturated O. It was confirmed that for most of surface functionalizations the ST-cut surface of quartz favors the horizontal deposition of *zigzag* tubes over *armchair* ones. SWCNT (6,0) is preferred along the directions of strong adsorption, although the SWCNT (7,0) is energetically favored to align along the y-axis, following epitaxial ordering. SWCNT (4,4) adsorbs stronger on surfaces that present small to none spin polarization.

During the nucleation of carbon caps, carbon atoms dissolved inside the catalyst diffuse towards the catalyst surface where they start nucleating carbon structures. Diffusion and precipitation of carbon atoms, cap nucleation, and the consequent nanotube alignment upon growth, might be influenced by the strength of interaction between carbon and the substrate. If the nucleated nanotube cap does not adsorb strongly to the support, we could observe vertical instead of horizontal growth. Here we show the preferential directions where horizontal growth may happen. After identifying the key elements defining preferential alignment, it is suggested that silica surfaces can be engineered to maximize the nanotube-surface and guide nanotubes horizontally along specific directions.

9. CONCLUSIONS AND RECOMMENDATIONS

Density functional theory calculations, and classical and ab initio molecular dynamics simulations were used to understand the catalytic growth mechanism of SWCNTs, as well as the life and selectivity of catalyst systems. The effect of different process variables on the catalyst life, and the diameter and concentration of defects of nascent tubes was studied via classical reactive molecular dynamics simulations. Furthermore, DFT calculations provided useful insights towards understanding the horizontal alignment of SWCNTs on quartz surfaces during growth. Data collected from MD and DFT simulations provide some clues for the ultimate goal of chirality and electronic type selectivity, which, along with horizontal alignment, are of significant interest for the use of SWCNTs in electronic devices

Classical MD simulations show that catalyst poisoning or nanotube growth is determined by a curvature energy competition between nanotubes and fullerenes of same diameter, assisted by the interaction between graphitic lattice of the nanotube and the catalyst surface. The curvature energy model describing growth was found to have experimental validity, although it only applies to floating catalysts. Simulations performed over deposited catalyst particles demonstrate that the catalyst-support attraction force must be optimum in order to grow nanotubes with high structural quality and avoid catalyst poisoning. MD trajectories show that the catalyst/substrate interaction must be strong enough to allow the carbon caps to lift off, but not too strong to favor the defective grow of carbon nanotubes. A model to quantify the percentage of defects in nanotubes was developed. This model normalizes the total number of hexagons formed per catalyzed carbon, relative to the same quantity for a perfect nanotube of same length. This approach allows for the measurement of the quality of nanotubes at any instant of growth and the unbiased comparison at different growth conditions. Results herein reported suggest an optimum temperature, catalyst size and shape, and growth rate to minimize the nucleation of topological defects in nanotubes. MD trajectories prove the vital role played by the catalyst surface in healing defects via adsorption and diffusion.

These results significantly impact the field of chirality control since the presence of defects introduces misorientation of hexagons, shifting the overall chiral angle.

Density functional theory calculations were employed to evaluate the interaction between SWCNTs and the clean ST-cut quartz substrate. It is demonstrated that armchair nanotubes do not align preferentially along any direction, whereas zigzag nanotubes adsorb strongly along certain crystallographic directions. Surprisingly, the direction [010] on the ST-cut surface of quartz represented the stronger adsorption for the SWCNT (7,0) a well as the weakest adsorption for the (4,4). These results suggest that the nanotube electronic band structure is a key factor on the preferential adsorption of zigzag tubes. Furthermore, small differences in adsorption energies between two directions provided some clues for the nanotube bending during the growth on quartz, which has been observed experimentally. The charge analysis demonstrates that electronic charges tend to accumulate at the nanotube/quartz interface for strong interactions, whereas the analysis of charge differences shows the displacement of charges from the interface towards the bulk of the clean surface, suggesting a partial oxidation of carbon nanotubes. Analysis of the electronic density of states proves that atomic interactions between substrate and nanotubes induce modifications of the occupied states near to the Fermi level, which can potentially modify the metallic or semi-conducting character of adsorbed SWCNTs.

AIMD simulations demonstrate that clean silica surfaces can be functionalized through the dissociation of water products at the low-coordinated silicon and oxygen atoms. These functionalizations introduce different surface terminations that modify not only the topology of the surface, but also the chemical nature of the atoms at the topmost layer. As a result of these surface modifications, the adsorption scenario of SWCNTs on quartz substrates is altered towards other preferential directions. The saturation of silicon atoms with OH functional groups released from water dissociation hinders the effect of unsaturated silicon on defining strong adsorption and alignment. It was concluded that specific functionalization modify the magnetic state of the quartz surface. This favored the adsorption of nanotube of specific electronic natures, such as armchair nanotubes

(SWCNT (4,4)), which does not interact strongly with clean silica surfaces. These results open up a window for deliberate functionalization of silica surfaces seeking predetermined horizontal alignments and electronic type selectivity.

Despite the fact that MD and DFT simulations provide detailed information about mechanisms and atomic interactions, experimental verification is needed to confirm the relationships between process conditions and the structure of SWCNTs, which have been postulated along this study. Furthermore, theoretical methods can be refined with the purpose of obtaining more accurate descriptions of the systems and represent real conditions during growth. Thus, the following future work is proposed to complement this study, and validate the postulates stated here:

- Growth rates must be decreased to the lowest rates allowed by molecular dynamics simulations. The rates of carbon addition in classical molecular dynamics simulations are in the order of m/s, which are extremely high compared to experimental chemical vapor deposition growth rates. Low carbon addition, will allow free surface diffusion of carbon on the catalyst surface seeking stability, which may have a significant impact on the structural quality of nanotubes.
- The catalyst substrate must have a better representation than the graphene model. Although the graphene model provides a reliable approach to measure the catalyst/substrate interactions, its morphology does not exemplify the structure of substrates commonly used as catalyst support. In order to achieve this goal, proper empirical force fields must be developed to represent interactions between silicon and oxygen, and between silica atoms and carbon and metal atoms. The use of a new interatomic potential to describe substrate interactions requires the implementation of the potential into the MD code for growth of nanotubes (SIMCAT), and the full compatibility between the new and old potentials. A refined description of the potential, including substrate interactions, will affect the catalyst

morphology, and therefore, the growth behavior and concentration of defects in nascent tubes

- Chirality is the structural variable that mostly defines the electronic behavior of nanotubes. Analysis of the dynamic evolution of the graphitic network orientation is needed to correlate the growth conditions to the chirality of grown nanotubes. Such analysis will allow tracking modifications of chiral angles as the growth takes place, and associating these modifications to the concentration of defects. The ultimate goal will be finding proper growth conditions seeking the synthesis of SWCNTs lying within a specific range of chiral angles. Accomplishing this task will require the development of a numerical approach capable of performing a dynamic measure of the chirality of mostly defective nanotubes.
- DFT calculations reported in sections 7 and 8 were limited by the computational resources available, and therefore, by the size of systems chosen to describe interactions between silica and sp^2 hybridized carbon atoms. The ideal scenario for an accurate representation will correspond to an infinitely long nanotube interacting with an infinite silica surface, as described through three-dimensional periodic boundary conditions. The main drawback will be the lattice mismatch likely to exist between the unit cells of nanotubes and silica surfaces. The compensation of this lattice mismatch will demand the construction of larger systems where the effects of nanotube borders are negligible, but this approach will signify a considerable computational effort.

REFERENCES

1 Iijima, S. Helical Microtubules of Graphitic Carbon. *Nature* **1991**, 354, 56-56.

2 Hamada, N., Sawada, S.-i. and Oshiyama, A. New one-dimensional conductors: Graphitic microtubules. *Physical Review Letters* **1992**, 68, 1579.

3 Saito, R., Fujita, M., Dresselhaus, G. and Dresselhaus, M. S. Electronic structure of chiral graphene tubules. *Applied Physics Letters* **1992**, 60, 2204-2206.

4 Chen, J., Hamon, M. A., Hu, H., Chen, Y., Rao, A. M., Eklund, P. C. and Haddon, R. C. Solution Properties of Single-Walled Carbon Nanotubes. *Science* **1998**, 282, 95-98.

5 Baughman, R. H., Cui, C., Zakhidov, A. A., Iqbal, Z., Barisci, J. N., Spinks, G. M., Wallace, G. G., Mazzoldi, A., De Rossi, D., Rinzler, A. G., Jaschinski, O., Roth, S. and Kertesz, M. Carbon Nanotube Actuators. *Science* **1999**, 284, 1340-1344.

6 Ghosh, S., Sood, A. K. and Kumar, N. Carbon Nanotube Flow Sensors. *Science* **2003**, 299, 1042-1044.

7 Tans, S. J., Verschueren, A. R. M. and Dekker, C. Room-temperature transistor based on a single carbon nanotube. *Nature* **1998**, 393, 49-52.

8 Hersam, M. C. Progress towards monodisperse single-walled carbon nanotubes. *Nat Nano* **2008**, 3, 387-394.

9 Bethune, D. S., Kiang, C. H., De Vries, M. S., Gorman, G., Savoy, R., Vazquez, J. and Beyers, R. Cobalt-catalysed growth of carbon nanotubes with single-atomic-layer walls. *Nature* **1993**, 363, 605-607.

10 Guo, T., Nikolaev, P., Thess, A., Colbert, D. T. and Smalley, R. E. Catalytic growth of single-walled manotubes by laser vaporization. *Chemical Physics Letters* **1995**, 243, 49-54.

11 Zheng, B., Lu, C., Gu, G., Makarovski, A., Finkelstein, G. and Liu, J. Efficient CVD Growth of Single-Walled Carbon Nanotubes on Surfaces Using Carbon Monoxide Precursor. *Nano Letters* **2002**, 2, 895-898.

12 Bachilo, S. M., Balzano, L., Herrera, J. E., Pompeo, F., Resasco, D. E. and Weisman, R. B. Narrow (n,m)-Distribution of Single-Walled Carbon Nanotubes Grown Using a Solid Supported Catalyst. *Journal of the American Chemical Society* **2003**, 125, 11186-11187.

13 Chiang, W.-H. and Mohan Sankaran, R. Linking catalyst composition to chirality distributions of as-grown single-walled carbon nanotubes by tuning NixFe1-x nanoparticles. *Nat Mater* **2009**, 8, 882-886.

14 Harutyunyan, A. R., Chen, G., Paronyan, T. M., Pigos, E. M., Kuznetsov, O. A., Hewaparakrama, K., Kim, S. M., Zakharov, D., Stach, E. A. and Sumanasekera, G. U. Preferential Growth of Single-Walled Carbon Nanotubes with Metallic Conductivity. *Science* **2009**, 326, 116-120.

15 Kroto, H. W., Heath, J. R., O'Brien, S. C., Curl, R. F. and Smalley, R. E. C60: Buckminsterfullerene. *Nature* **1985**, 318, 162-163.

16 Gómez-Gualdrón, D. A., Burgos, J. C., Yu, J. and Balbuena, P. B. in *Progress in Molecular Biology and Translational Science* Vol. Volume 104 (ed Villaverde Antonio) 175-245 (Academic Press, 2011).

17 Ding, F., Bolton, K. and Rosén, A. Nucleation and Growth of Single-Walled Carbon Nanotubes: A Molecular Dynamics Study. *The Journal of Physical Chemistry B* **2004**, 108, 17369-17377.

18 Kukovitsky, E. F., L'Vov, S. G. and Sainov, N. A. VLS-growth of carbon nanotubes from the vapor. *Chemical Physics Letters* **2000**, 317, 65-70.

19 Gómez-Gualdrón, D. A. and Balbuena, P. B. Characterization of carbon atomistic pathways during single-walled carbon nanotube growth on supported metal nanoparticles. *Carbon* **2013**, 57, 298-309.

20 Chiang, I. W., Brinson, B. E., Huang, A. Y., Willis, P. A., Bronikowski, M. J., Margrave, J. L., Smalley, R. E. and Hauge, R. H. Purification and Characterization of Single-Wall Carbon Nanotubes (SWNTs) Obtained from the Gas-Phase Decomposition of CO (HiPco Process). *The Journal of Physical Chemistry B* **2001**, 105, 8297-8301.

21 Resasco, D. E., Alvarez, W. E., Pompeo, F., Balzano, L., Herrera, J. E., Kitiyanan, B. and Borgna, A. A Scalable Process for Production of Single-walled

Carbon Nanotubes (SWNTs) by Catalytic Disproportionation of CO on a Solid Catalyst. *Journal of Nanoparticle Research* **2002**, 4, 131-136.

22 Ding, F., Harutyunyan, A. R. and Yakobson, B. I. Dislocation theory of chirality-controlled nanotube growth. *Proceedings of the National Academy of Sciences* **2009**, 106, 2506-2509.

23 Diego, A. G.-G. and Perla, B. B. Growth of chiral single-walled carbon nanotube caps in the presence of a cobalt cluster. *Nanotechnology* **2009**, 20, 215601.

24 Ding, L., Tselev, A., Wang, J., Yuan, D., Chu, H., McNicholas, T. P., Li, Y. and Liu, J. Selective Growth of Well-Aligned Semiconducting Single-Walled Carbon Nanotubes. *Nano Letters* **2009**, 9, 800-805.

25 Che, Y., Wang, C., Liu, J., Liu, B., Lin, X., Parker, J., Beasley, C., Wong, H. S. P. and Zhou, C. Selective Synthesis and Device Applications of Semiconducting Single-Walled Carbon Nanotubes Using Isopropyl Alcohol as Feedstock. *ACS Nano* **2012**, 6, 7454-7462.

26 Li, P. and Zhang, J. Sorting out semiconducting single-walled carbon nanotube arrays by preferential destruction of metallic tubes using water. *Journal of Materials Chemistry* **2011**, 21, 11815-11821.

27 Ding, L., Yuan, D. and Liu, J. Growth of High-Density Parallel Arrays of Long Single-Walled Carbon Nanotubes on Quartz Substrates. *Journal of the American Chemical Society* **2008**, 130, 5428-5429.

28 *Cerius2 User Guide*. (Molecular Simulations Inc., 1997).

29 Miller, D. A. B. *Quantum Mechanics for Scientists and Engineers*. (Cambridge Univerisity Press, 2008).

30 Foresman, J. B. and Frisch, A. *Exploring Chemistry with Electronic Structure Methods* Second edn, (Gaussian, Inc., 1996).

31 Sholl, D. and Steckel, J. A. *Density Functional Theory: A Practical Introduction*. (Wiley, 2009).

32 Cai, W., Li, J. and Yip, S. in *Comprehensive Nuclear Materials* (ed Rudy J. M. Konings) 249-265 (Elsevier, 2012).

33 Dawid, T., Christian, D. L., Nikolaos, R., Natalia, M. and Lev, K. Temperature control in molecular dynamic simulations of non-equilibrium processes. *Journal of Physics: Condensed Matter* **2010**, 22, 074205.

34 Schneider, T. and Stoll, E. Molecular-dynamics study of a three-dimensional one-component model for distortive phase transitions. *Physical Review B* **1978**, 17, 1302-1322.

35 Bussi, G. and Parrinello, M. Accurate sampling using Langevin dynamics. *Physical Review E* **2007**, 75, 056707.

36 Leach, A. R. *Molecular Modelling: Principles and Applications*. Second edn, (Prentice Hall, 2001).

37 Rappe, A. K., Casewit, C. J., Colwell, K. S., Goddard, W. A. and Skiff, W. M. UFF, a full periodic table force field for molecular mechanics and molecular dynamics simulations. *Journal of the American Chemical Society* **1992**, 114, 10024-10035.

38 Sutton, A. P. and Chen, J. Long-range Finnisâ€"Sinclair potentials. *Philosophical Magazine Letters* **1990**, 61, 139 - 146.

39 Brenner, D. W., Shenderova, O. A., Harrison, J. A., Stuart, S. J., Ni, B. and Sinnott, S. B. A second-generation reactive empirical bond order (REBO) potential energy expression for hydrocarbons. *Journal of Physics: Condensed Matter* **2002**, 14, 783-802.

40 van Duin, A. C. T., Dasgupta, S., Lorant, F. and Goddard, W. A. ReaxFF: A Reactive Force Field for Hydrocarbons. *The Journal of Physical Chemistry A* **2001**, 105, 9396-9409.

41 Todorov, I. T. and Smith, W. *The DLPOLY_4 User Manual*. (STFC Daresbury Laboratory, 2014).

42 Chen, E. T., Barnett, R. N. and Landman, U. Surface melting of Ni(110). *Physical Review B* **1990**, 41, 439-450.

43 Hohenberg, P. and Kohn, W. Inhomogeneous Electron Gas. *Physical Review* **1964**, 136, B864-B871.

44 Kohn, W. and Sham, L. J. Self-Consistent Equations Including Exchange and Correlation Effects. *Physical Review* **1965**, 140, A1133-A1138.

45 Perdew, J. P., Burke, K. and Wang, Y. Generalized gradient approximation for the exchange-correlation hole of a many-electron system. *Physical Review B* **1996**, 54, 16533-16539.

46 Harrison, N. M. *An Introduction to Density Functional Theory*. Vol. 187 (IOS Press, 2003).

47 Perdew, J. P., Burke, K. and Ernzerhof, M. Generalized Gradient Approximation Made Simple. *Phys. Rev. Lett.* **1996**, 77, 3865-3868.

48 Perdew, J. P. and Wang, Y. Accurate and simple analytic representation of the electron-gas correlation energy. *Physical Review B* **1992**, 45, 13244-13249.

49 Monkhorst, H. J. and Pack, J. D. Special points for Brillouin-zone integrations. *Phys. Rev. B* **1976**, 13, 5188-5192.

50 Marx, D. and Hutter, J. *Ab Initio Molecular Dynamics: Basic Theory and Advanced Methods*. (Cambridge Univeristy Press, 2009).

51 Iijima, S. and Ichihashi, T. Single-shell carbon nanotubes of 1-nm diameter. *Nature* **1993**, 363, 603-605.

52 Treacy, M. M. J., Ebbesen, T. W. and Gibson, J. M. Exceptionally high Young's modulus observed for individual carbon nanotubes. *Nature* **1996**, 381, 678-680.

53 Fan, S., Chapline, M. G., Franklin, N. R., Tombler, T. W., Cassell, A. M. and Dai, H. Self-Oriented Regular Arrays of Carbon Nanotubes and Their Field Emission Properties. *Science* **1999**, 283, 512-514.

54 Tang, Z. K., Zhang, L., Wang, N., Zhang, X. X., Wen, G. H., Li, G. D., Wang, J. N., Chan, C. T. and Sheng, P. Superconductivity in 4 Angstrom Single-Walled Carbon Nanotubes. *Science* **2001**, 292, 2462-2465.

55 Odom, T. W., Huang, J.-L., Kim, P. and Lieber, C. M. Atomic structure and electronic properties of single-walled carbon nanotubes. *Nature* **1998**, 391, 62-64.

56 Matsuda, Y., Deng, W.-Q. and Goddard, W. A. Contact Resistance Properties between Nanotubes and Various Metals from Quantum Mechanics. *The Journal of Physical Chemistry C* **2007**, 111, 11113-11116.

57 Ebbesen, T. W. and Ajayan, P. M. Large-scale synthesis of carbon nanotubes. *Nature* **1992**, 358, 220-222.

58 Jose-Yacaman, M., Miki-Yoshida, M., Rendon, L. and Santiesteban, J. G. Catalytic growth of carbon microtubules with fullerene structure. *Applied Physics Letters* **1993**, 62, 657-659.

59 Ishigami, N., Ago, H., Imamoto, K., Tsuji, M., Iakoubovskii, K. and Minami, N. Crystal Plane Dependent Growth of Aligned Single-Walled Carbon Nanotubes on Sapphire. *Journal of the American Chemical Society* **2008**, 130, 9918-9924.

60 Xiang, R., Einarsson, E., Okawa, J., Miyauchi, Y. and Maruyama, S. Acetylene-Accelerated Alcohol Catalytic Chemical Vapor Deposition Growth of Vertically Aligned Single-Walled Carbon Nanotubes. *J. Phys. Chem. C* **2009**, 113, 7511-7515.

61 Fiawoo, M. F., Bonnot, A. M., Jourdain, V., Michel, T., Picher, M., Arenal, R., Thibault-Penisson, J. and Loiseau, A. Substrate preparation techniques for direct investigation by TEM of single wall carbon nanotubes grown by chemical vapor deposition. *Surf. Sci.* **2009**, 603, 1115-1120.

62 Lolli, G., Zhang, L., Balzano, L., Sakulchaicharoen, N., Tan, Y. and Resasco, D. E. Tailoring (n,m) Structure of Single-Walled Carbon Nanotubes by Modifying Reaction Conditions and the Nature of the Support of CoMo Catalysts. *The Journal of Physical Chemistry B* **2006**, 110, 2108-2115.

63 Harutyunyan, A. R., Chen, G. G., Paronyan, T. M., Pigos, E. M., Kuznetsov, O. A., Hewaparakrama, K., Kim, S. M., Zakharov, D., Stach, E. A. and Sumanasekera, G. U. Preferential Growth of Single-Walled Carbon Nanotubes with Metallic Conductivity. *Science* **2009**, 326, 116-120.

64 Helveg, S., Lopez-Cartes, C., Sehested, J., Hansen, P. L., Clausen, B. S., Rostrup-Nielsen, J. R., Abild-Pedersen, F. and Norskov, J. K. Atomic-scale imaging of carbon nanofibre growth. *Nature* **2004**, 427, 426-429.

65 Hofmann, S., Sharma, R., Ducati, C., Du, G., Mattevi, C., Cepek, C., Cantoro, M., Pisana, S., Parvez, A., Cervantes-Sodi, F., Ferrari, A. C., Dunin-Borkowski,

R., Lizzit, S., Petaccia, L., Goldoni, A. and Robertson, J. In situ Observations of Catalyst Dynamics during Surface-Bound Carbon Nanotube Nucleation. *Nano Letters* **2007**, 7, 602-608.

66 Zhu, H., Suenaga, K., Wei, J., Wang, K. and Wu, D. A strategy to control the chirality of single-walled carbon nanotubes. *Journal of Crystal Growth* **2008**, 310, 5473-5476.

67 Kanzow, H. and Ding, A. Formation mechanism of single-wall carbon nanotubes on liquid-metal particles. *Physical Review B* **1999**, 60, 11180.

68 Kanzow, H., Lenski, C. and Ding, A. Single-wall carbon nanotube diameter distributions calculated from experimental parameters. *Physical Review B* **2001**, 63, 125402.

69 Shibuta, Y. and Maruyama, S. Molecular dynamics simulation of formation process of single-walled carbon nanotubes by CCVD method. *Chemical Physics Letters* **2003**, 382, 381-386.

70 Ding, F., Rosen, A., Campbell, E. E. B., Falk, L. K. L. and Bolton, K. Graphitic Encapsulation of Catalyst Particles in Carbon Nanotube Production. *The Journal of Physical Chemistry B* **2006**, 110, 7666-7670.

71 Hafner, J. H., Bronikowski, M. J., Azamian, B. R., Nikolaev, P., Rinzler, A. G., Colbert, D. T., Smith, K. A. and Smalley, R. E. Catalytic growth of single-wall carbon nanotubes from metal particles. *Chemical Physics Letters* **1998**, 296, 195-202.

72 Gülseren, O., Yildirim, T. and Ciraci, S. Systematic ab initio study of curvature effects in carbon nanotubes. *Physical Review B* **2002**, 65, 153405.

73 Xiao, Y., Li, Z. M., Yan, X. H., Zhang, Y., Mao, Y. L. and Yang, Y. R. Curvature effect on the radial breathing modes of single-walled carbon nanotubes. *Physical Review B* **2005**, 71, 233405.

74 Cabria, I., Mintmire, J. W. and White, C. T. Metallic and semiconducting narrow carbon nanotubes. *Physical Review B* **2003**, 67, 121406.

75 Kudin, K. N., Scuseria, G. E. and Yakobson, B. I. C2F, BN, and C nanoshell elasticity from ab initio computations. *Physical Review B* **2001**, 64, 235406.

76 Adams, G. B., Sankey, O. F., Page, J. B., O'Keeffe, M. and Drabold, D. A. Energetics of Large Fullerenes: Balls, Tubes, and Capsules. *Science* **1992**, 256, 1792-1795.

77 Girifalco, L. A. Interaction potential for carbon (C60) molecules. *The Journal of Physical Chemistry* **2002**, 95, 5370-5371.

78 Ding, F., Bolton, K. and Rosen, A. Nucleation and growth of single-walled carbon nanotubes: A molecular dynamics study. *J. Phys. Chem. B* **2004**, 108, 17369-17377.

79 Maruyama, S. and Shibuta, Y. Molecular dynamics in formation process of SWNTs. *Mol. Cryst. Liq. Cryst.* **2002**, 387, 311-316.

80 Zhao, J., Martinez-Limia, A. and Balbuena, P. B. Understanding catalyzed growth of single-wall carbon nanotubes. *Nanotechnology* **2005**, 16, S575-S581.

81 Zheng, G. S., Irle, S., Elstner, M. and Morokuma, K. Quantum chemical molecular dynamics model study of fullerene formation from open-ended carbon nanotubes. *J. Phys. Chem.* **2004**, 108, 3182-3194.

82 Amara, H., Bichara, C. and Ducastelle, F. Understanding the nucleation mechanisms of carbon nanotubes in catalytic chemical vapor deposition. *Physical Review Letters* **2008**, 100, 4.

83 Ramirez-Caballero, G. E., Burgos, J. C. and Balbuena, P. B. Growth of carbon structures on stepped (211) cobalt surfaces. *J. Phys. Chem. C* **2009**, 113, 15658-15666.

84 Martinez-Limia, A., Zhao, J. and Balbuena, P. B. Molecular dynamics study of the initial stages of catalyzed single-wall carbon nanotubes growth: Force field development. *J. Mol. Mod.* **2007**, 13, 595-600.

85 SIMCAT (Texas A&M University, College Station, TX, 2007).

86 Balbuena, P. B., Zhao, J., Huang, S., Wang, Y., Sakulchaicharoen, N. and Resasco, D. E. Role of the catalyst in the growth of single-wall carbon nanotubes. *J. Nanosci. Nanotech.* **2006**, 6, 1247-1258.

87 Ribas, M. A., Ding, F., Balbuena, P. B. and Yakobson, B. I. Nanotube nucleation versus carbon-catalyst adhesion--probed by MD simulations. *J. Chem. Phys.* **2009**, 131, 224501.

88 Giovannetti, G., Khomyakov, P. A., Brocks, G., Karpan, V. M., van den Brink, J. and Kelly, P. J. Doping Graphene with Metal Contacts. *Physical Review Letters* **2008**, 101, 026803.

89 Yuliang, M., Jianmei, Y. and Jianxin, Z. Density functional calculation of transition metal adatom adsorption on graphene. *Journal of Physics: Condensed Matter* **2008**, 20, 115209.

90 Lim, D.-H., Negreira, A. S. and Wilcox, J. DFT Studies on the Interaction of Defective Graphene-Supported Fe and Al Nanoparticles. *The Journal of Physical Chemistry C* **2011**, 115, 8961-8970.

91 Yu, B., Liu, C., Hou, P.-X., Tian, Y., Li, S., Liu, B., Li, F., Kauppinen, E. I. and Cheng, H.-M. Bulk Synthesis of Large Diameter Semiconducting Single-Walled Carbon Nanotubes by Oxygen-Assisted Floating Catalyst Chemical Vapor Deposition. *Journal of the American Chemical Society* **2011**, 133, 5232-5235.

92 Zhu, Z., Jiang, H., Susi, T., Nasibulin, A. G. and Kauppinen, E. I. The Use of NH3 to Promote the Production of Large-Diameter Single-Walled Carbon Nanotubes with a Narrow (n,m) Distribution. *Journal of the American Chemical Society* **2010**, 133, 1224-1227.

93 Liu, Q., Ren, W., Chen, Z.-G., Wang, D.-W., Liu, B., Yu, B., Li, F., Cong, H. and Cheng, H.-M. Diameter-Selective Growth of Single-Walled Carbon Nanotubes with High Quality by Floating Catalyst Method. *ACS Nano* **2008**, 2, 1722-1728.

94 Anna, M., Albert, G. N. and Esko, I. K. The role of metal nanoparticles in the catalytic production of single-walled carbon nanotubes—a review. *Journal of Physics: Condensed Matter* **2003**, 15, S3011.

95 Ding, F., Rosén, A., Campbell, E. E. B., Falk, L. K. L. and Bolton, K. Graphitic Encapsulation of Catalyst Particles in Carbon Nanotube Production. *The Journal of Physical Chemistry B* **2006**, 110, 7666-7670.

96 Balbuena, P. B., Zhao, J., Huang, S., Wang, Y., Sakulchaicharoen, N. and Resasco, D. E. Role of the Catalyst in the Growth of Single-Wall Carbon Nanotubes. *Journal of Nanoscience and Nanotechnology* **2006**, 6, 1247-1258.

97 Zhao, J., Martinez-Limia, A. and Balbuena, P. B. Understanding catalysed growth of single-wall carbon nanotubes. *Nanotechnology* **2005**, 16, S575-S581.

98 Ribas, M. A., Ding, F., Balbuena, P. B. and Yakobson, B. I. Nanotube nucleation versus carbon-catalyst adhesion--Probed by molecular dynamics simulations. *The Journal of Chemical Physics* **2009**, 131, 224501-224507.

99 Burgos, J. C., Reyna, H., Yakobson, B. I. and Balbuena, P. B. Interplay of Catalyst Size and Metal−Carbon Interactions on the Growth of Single-Walled Carbon Nanotubes. *The Journal of Physical Chemistry C* **2010**, 114, 6952-6958.

100 Ward, J. W., Wei, B. Q. and Ajayan, P. M. Substrate effects on the growth of carbon nanotubes by thermal decomposition of methane. *Chemical Physics Letters* **2003**, 376, 717-725.

101 Li, Y., Kim, W., Zhang, Y., Rolandi, M., Wang, D. and Dai, H. Growth of Single-Walled Carbon Nanotubes from Discrete Catalytic Nanoparticles of Various Sizes. *The Journal of Physical Chemistry B* **2001**, 105, 11424-11431.

102 Morrow, B. H. and Striolo, A. Assessing how metal-carbon interactions affect the structure of supported platinum nanoparticles. *Mol. Simul.* **2009**, 35, 795-803.

103 Lolli, G., Zhang, L. A., Balzano, L., Sakulchaicharoen, N., Tan, Y. Q. and Resasco, D. E. Tailoring (n,m) structure of single-walled carbon nanotubes by modifying reaction conditions and the nature of the support of CoMo catalysts. *Journal of Physical Chemistry B* **2006**, 110, 2108-2115.

104 Martinez-Limia, A., Zhao, J. and Balbuena, P. Molecular dynamics study of the initial stages of catalyzed single-wall carbon nanotubes growth: force field development. *Journal of Molecular Modeling* **2007**, 13, 595-600.

105 Ding, F., Larsson, P., Larsson, J. A., Ahuja, R., Duan, H., Rosen, A. and Bolton, K. The Importance of Strong Carbon−Metal Adhesion for Catalytic Nucleation of Single-Walled Carbon Nanotubes. *Nano Letters* **2007**, 8, 463-468.

106 Robach, O., Renaud, G. and Barbier, A. Structure and morphology of the Ag/MgO(001) interface during in situ growth at room temperature. *Physical Review B* **1999**, 60, 5858.

107 Pacchioni, G. and Rosch, N. Supported nickel and copper clusters on MgO(100): A first-principles calculation on the metal/oxide interface. *The Journal of Chemical Physics* **1996**, 104, 7329-7337.

108 Silly, F. and Castell, M. R. Self-assembled supported Co nanocrystals: The adhesion energy of face-centered-cubic Co on SrTiO[sub 3](001)-(2 x 2). *Applied Physics Letters* **2005**, 87, 053106-053103.

109 Gomez-Gualdron, D. A., Zhao, J. and Balbuena, P. B. Nanocatalyst structure as a template to define chirality of nascent single-wall carbon nanotubes. *J. Chem. Phys.* **2011**, 134, 014705.

110 Jarvis, E. A. A. and Carter, E. A. Exploiting Covalency to Enhance Metal–Oxide and Oxide–Oxide Adhesion at Heterogeneous Interfaces. *Journal of the American Ceramic Society* **2003**, 86, 373-386.

111 Czekaj, I., Loviat, F., Wambach, J. and Wokaun, A. Nickel Deposition on y-Al_2O_3: Modelling Metal Particle Behaviour at the Support. *CHIMIA International Journal for Chemistry* **2009**, 63, 193-196.

112 Dikonimos Makris, T., Giorgi, L., Giorgi, R., Lisi, N. and Salernitano, E. CNT growth on alumina supported nickel catalyst by thermal CVD. *Diamond and Related Materials* **2005**, 14, 815-819.

113 Hasegawa, K., Noda, S., Sugime, H., Kakehi, K., Maruyama, S. and Yamaguchi, Y. Growth Window and Possible Mechanism of Millimeter-Thick Single-Walled Carbon Nanotube Forests. *Journal of Nanoscience and Nanotechnology* **2008**, 8, 6123-6128.

114 Jeong, H. J., An, K. H., Lim, S. C., Park, M.-S., Chang, J.-S., Park, S.-E., Eum, S. J., Yang, C. W., Park, C.-Y. and Lee, Y. H. Narrow diameter distribution of singlewalled carbon nanotubes grown on Ni–MgO by thermal chemical vapor deposition. *Chemical Physics Letters* **2003**, 380, 263-268.

115 Kakehi, K., Noda, S., Chiashi, S. and Maruyama, S. Supported Ni catalysts from nominal monolayer grow single-walled carbon nanotubes. *Chemical Physics Letters* **2006**, 428, 381-385.

116 Seidel, R., Duesberg, G. S., Unger, E., Graham, A. P., Liebau, M. and Kreupl, F. Chemical Vapor Deposition Growth of Single-Walled Carbon Nanotubes at 600 °C and a Simple Growth Model. *The Journal of Physical Chemistry B* **2004**, 108, 1888-1893.

117 de Heer, W. A., Châtelain, A. and Ugarte, D. A Carbon Nanotube Field-Emission Electron Source. *Science* **1995**, 270, 1179-1180.

118 Page, A. J., Ohta, Y., Okamoto, Y., Irle, S. and Morokuma, K. Defect Healing during Single-Walled Carbon Nanotube Growth: A Density-Functional Tight-Binding Molecular Dynamics Investigation. *The Journal of Physical Chemistry C* **2009**, 113, 20198-20207.

119 Nie, J.-Q., Zhang, Q., Zhao, M.-Q., Huang, J.-Q., Wen, Q., Cui, Y., Qian, W.-Z. and Wei, F. Synthesis of high quality single-walled carbon nanotubes on natural sepiolite and their use for phenol absorption. *Carbon* **2011**, 49, 1568-1580.

120 Lu, J. Q., Kopley, T. E., Moll, N., Roitman, D., Chamberlin, D., Fu, Q., Liu, J., Russell, T. P., Rider, D. A. and Manners, I. High-Quality Single-Walled Carbon Nanotubes with Small Diameter, Controlled Density, and Ordered Locations Using a Polyferrocenylsilane Block Copolymer Catalyst Precursor. *Chemistry of Materials* **2005**, 17, 2227-2231.

121 Charlier, J. C. Defects in Carbon Nanotubes. *Accounts of Chemical Research* **2002**, 35, 1063-1069.

122 Collins, P. G. Defects and disorder in carbon nanotubes 2. *Oxford Handbook of Nanoscience and Technology: Volume 2: Materials: Structures, Properties and Characterization Techniques* **2010**, 2, 31.

123 Berber, S. and Oshiyama, A. Reconstruction of mono-vacancies in carbon nanotubes: Atomic relaxation vs. spin polarization. *Physica B: Condensed Matter* **2006**, 376,Äì377, 272-275.

124 Krasheninnikov, A. V., Lehtinen, P. O., Foster, A. S. and Nieminen, R. M. Bending the rules: Contrasting vacancy energetics and migration in graphite and carbon nanotubes. *Chemical Physics Letters* **2006**, 418, 132-136.

125 Stone, A. J. and Wales, D. J. Theoretical studies of icosahedral C60 and some related species. *Chemical Physics Letters* **1986**, 128, 501-503.

126 Charlier, J. C., Ebbesen, T. W. and Lambin, P. Structural and electronic properties of pentagon-heptagon pair defects in carbon nanotubes. *Physical Review B* **1996**, 53, 11108-11113.

127 Ding, F. Theoretical study of the stability of defects in single-walled carbon nanotubes as a function of their distance from the nanotube end. *Physical Review B* **2005**, 72, 245409.

128 Yuan, Q., Xu, Z., Yakobson, B. I. and Ding, F. Efficient Defect Healing in Catalytic Carbon Nanotube Growth. *Physical Review Letters* **2012**, 108, 245505.

129 Chen-Li, Z. and Hui-Shen, S. Self-healing in defective carbon nanotubes: a molecular dynamics study. *Journal of Physics: Condensed Matter* **2007**, 19, 386212.

130 Page, A. J., Ohta, Y., Irle, S. and Morokuma, K. Mechanisms of Single-Walled Carbon Nanotube Nucleation, Growth, and Healing Determined Using QM/MD Methods. *Accounts of Chemical Research* **2010**, 43, 1375-1385.

131 Nayak, S. K., Khanna, S. N., Rao, B. K. and Jena, P. Physics of Nickel Clusters:‚Äâ Energetics and Equilibrium Geometries. *The Journal of Physical Chemistry A* **1997**, 101, 1072-1080.

132 Saroj, K. N., Khanna, S. N., Rao, B. K. and Jena, P. Thermodynamics of small nickel clusters. *Journal of Physics: Condensed Matter* **1998**, 10, 10853.

133 Huang, S.-P. and Balbuena, P. B. Melting of Bimetallic Cu‚àíNi Nanoclusters. *The Journal of Physical Chemistry B* **2002**, 106, 7225-7236.

134 Burgos, J. C., Jones, E. and Balbuena, P. B. Effect of the Metal−Substrate Interaction Strength on the Growth of Single-Walled Carbon Nanotubes. *The Journal of Physical Chemistry C* **2011**, 115, 7668-7675.

135 Yamada, T., Namai, T., Hata, K., Futaba, D. N., Mizuno, K., Fan, J., Yudasaka, M., Yumura, M. and Iijima, S. Size-selective growth of double-walled carbon nanotube forests from engineered iron catalysts. *Nat Nano* **2006**, 1, 131-136.

136 Burgos, J. C., Jones, E. and Balbuena, P. B. Effect of the Metal‚àíSubstrate Interaction Strength on the Growth of Single-Walled Carbon Nanotubes. *The Journal of Physical Chemistry C* **2011**, 115, 7668-7675.

137 Giovannetti, G., Khomyakov, P. A., Brocks, G., Karpan, V. M., van den Brink, J. and Kelly, P. J. Doping Graphene with Metal Contacts. *Physical Review Letters* **2008**, 101, 026803.

138 Gómez-Gualdrón, D. A., Beetge, J. M., Burgos, J. C. and Balbuena, P. B. Effects of Precursor Type on the CVD Growth of Single-Walled Carbon Nanotubes. *The Journal of Physical Chemistry C* **2013**, 117, 10397-10409.

139 Picher, M., Navas, H., Arenal, R., Quesnel, E., Anglaret, E. and Jourdain, V. Influence of the growth conditions on the defect density of single-walled carbon nanotubes. *Carbon* **2012**, 50, 2407-2416.

140 Vinten, P., Marshall, P., Lefebvre, J. and Finnie, P. Thermodynamic and Energetic Effects on the Diameter and Defect Density in Single-Walled Carbon Nanotube Synthesis. *The Journal of Physical Chemistry C* **2013**, 117, 3527-3536.

141 Raty, J.-Y., Gygi, F. and Galli, G. Growth of Carbon Nanotubes on Metal Nanoparticles: A Microscopic Mechanism from Ab Initio Molecular Dynamics Simulations. *Physical Review Letters* **2005**, 95, 096103.

142 Iijima, S. Helical Microtubules of Graphitic Carbon. *Nature* **1991**, 354, 56-58.

143 Bernholc, J., Brenner, D., Nardelli, M. B., Meunier, V. and Roland, C. Mechanical and Electrical Properties of Nanotubes. *Ann. Rev. Mater. Res.* **2002**, 32, 347-375.

144 Pop, E., Mann, D., Wang, Q., Goodson, K. E. and Dai, H. J. Thermal Conductance of an Individual Single-Wall Carbon Nanotube above Room Temperature. *Nano Lett.* **2006**, 6, 96-100.

145 Javey, A., Kim, H., Brink, M., Wang, Q., Ural, A., Guo, J., McIntyre, P., McEuen, P., Lundstrom, M. and Dai, H. J. High-Kappa Dielectrics for Advanced Carbon-Nanotube Transistors and Logic Gates. *Nat. Mater.* **2002**, 1, 241-246.

146 Zhou, W., Han, Z., Wang, J., Zhang, Y., Jin, Z., Sun, X., Zhang, Y., Yan, C. and Li, Y. Copper Catalyzing Growth of Single-Walled Carbon Nanotubes on Substrates. *Nano Lett.* **2006**, 6, 2987-2990.

147 Zheng, B., Lu, C. G., Gu, G., Makarovski, A., Finkelstein, G. and Liu, J. Efficient CVD Growth of Single-Walled Carbon Nanotubes on Surfaces using Carbon Monoxide Precursor. *Nano Lett.* **2002**, 2, 895-898.

148 Saito, R., Fujita, M., Dresselhaus, G. and Dresselhaus, M. S. Electronic-Structure of Chiral Graphene Tubules. *Appl. Phys. Lett.* **1992**, 60, 2204-2206.

149 Ding, L., Tselev, A., Wang, J. Y., Yuan, D. N., Chu, H. B., McNicholas, T. P., Li, Y. and Liu, J. Selective Growth of Well-Aligned Semiconducting Single-Walled Carbon Nanotubes. *Nano Lett.* **2009**, 9, 800-805.

150 Chiang, W. H. and Sankaran, R. M. Linking Catalyst Composition to Chirality Distributions of As-Grown Single-Walled Carbon Nanotubes by Tuning NixFe1-x Nanoparticles. *Nat. Mater.* **2009**, 8, 882-886.

151 Krupke, R., Hennrich, F., von Lohneysen, H. and Kappes, M. M. Separation of Metallic from Semiconducting Single-Walled Carbon Nanotubes. *Science* **2003**, 301, 344-347.

152 Heller, D. A., Mayrhofer, R. M., Baik, S., Grinkova, Y. V., Usrey, M. L. and Strano, M. S. Concomitant Length and Diameter Separation of Single-Walled Carbon Nanotubes. *J. Am. Chem. Soc.* **2004**, 126, 14567-14573.

153 Arnold, M. S., Stupp, S. I. and Hersam, M. C. Enrichment of Single-Walled Carbon Nanotubes by Diameter in Density Gradients. *Nano Lett.* **2005**, 5, 713-718.

154 Ding, L., Yuan, D. N. and Liu, J. Growth of High-Density Parallel Arrays of Long Single-Walled Carbon Nanotubes on Quartz Substrates. *J. Am. Chem. Soc.* **2008**, 130, 5428-5429.

155 Rutkowska, A., Walker, D., Gorfman, S., Thomas, P. A. and Macpherson, J. V. Horizontal Alignment of Chemical Vapor-Deposited SWNTs on Single-Crystal Quartz Surfaces: Further Evidence for Epitaxial Alignment. *J. Phys. Chem. C* **2009**, 113, 17087-17096.

156 Yuan, D. N., Ding, L., Chu, H. B., Feng, Y. Y., McNicholas, T. P. and Liu, J. Horizontally Aligned Single-Walled Carbon Nanotube on Quartz from a Large Variety of Metal Catalysts. *Nano Lett.* **2008**, 8, 2576-2579.

157 Hong, G., Zhang, B., Peng, B. H., Zhang, J., Choi, W. M., Choi, J. Y., Kim, J. M. and Liu, Z. F. Direct Growth of Semiconducting Single-Walled Carbon Nanotube Array. *J. Am. Chem. Soc.* **2009**, 131, 14642-14643.

158 Kresse, G. and Furthmueller, J. Efficient Iterative Schemes for Ab Initio Total-Energy Calculations using a Plane-Wave Basis Set. *Phys. Rev. B* **1996**, 54, 11169-11186.

159 Kresse, G. and Furthmuller, J. Efficiency of Ab-Initio Total Energy Calculations for Metals and Semiconductors using a Plane-Wave Basis Set. *Comput. Mater. Sci.* **1996**, 6, 15-50.

160 Blochl, P. E. Projector Augmented-Wave Method. *Phys. Rev. B* **1994**, 50, 17953-17979.

161 Blochl, P. E., Jepsen, O. and Andersen, O. K. Improved Tetrahedron Method for Brillouin-Zone Integrations. *Phys. Rev. B* **1994**, 49, 16223-16233.

162 Resasco, D. E., Alvarez, W. E., Pompeo, F., Balzano, L., Herrera, J. E., Kitiyanan, B. and Borgna, A. A Scalable Process for Production of Single-Walled Carbon Nanotubes (SWNTs) by Catalytic Disproportionation of CO on a Solid Catalyst. *J. Nanopart. Res.* **2002**, 4, 131-136.

163 Chiashi, S., Okabe, H., Inoue, T., Shiomi, J., Sato, T., Kono, S., Terasawa, M. and Maruyama, S. Growth of Horizontally Aligned Single-Walled Carbon Nanotubes on the Singular R-Plane (10-11) of Quartz. *J. Phys. Chem. C* **2012**, 116, 6805-6808.

164 Materials Studio v. 4.3 (Accelrys Software Inc., 2008).

165 Hamada, N., Sawada, S. and Oshiyama, A. New One-Dimensional Conductors-Graphitic Microtubules. *Phys. Rev. Lett.* **1992**, 68, 1579-1581.

166 Blase, X., Benedict, L. X., Shirley, E. L. and Louie, S. G. Hybridization Effects and Metallicity in Small Radius Carbon Nanotubes. *Phys. Rev. Lett.* **1994**, 72, 1878-1881.

167 Gao, W. and Huang, R. Effect of Surface Roughness on Adhesion of Graphene Membranes. *J. Phys. D-Appl. Phys.* **2011**, 44, 452001.

168 Cuong, N. T., Otani, M. and Okada, S. Semiconducting Electronic Property of Graphene Adsorbed on (0001) Surfaces of SiO2. *Phys. Rev. Lett.* **2011**, 106, 106801.

169 Wang, Q. Effective In-Plane Stiffness and Bending Rigidity of Armchair and Zigzag Carbon Nanotubes. *Int. J. Solids Struct.* **2004**, 41, 5451-5461.

170 Chen, G., Paronyan, T. M., Pigos, E. M., Sumanasekera, G. U. and Harutyunyan, A. R. The Performance Volatility of Carbon Nanotube-Based Devices: Impact of Ambient Oxygen. *Appl. Phys. Lett.* **2009**, 95, 123118-123113.

171 Tsang, J. C., Freitag, M., Perebeinos, V., Liu, J. and Avouris, P. Doping and Phonon Renormalization in Carbon Nanotubes. *Nat. Nanotechnol.* **2007**, 2, 725-730.

172 Bernholc, J., Brenner, D., Buongiorno Nardelli, M., Meunier, V. and Roland, C. MECHANICAL AND ELECTRICAL PROPERTIES OF NANOTUBES. *Annual Review of Materials Research* **2002**, 32, 347-375.

173 Pop, E., Mann, D., Wang, Q., Goodson, K. and Dai, H. Thermal Conductance of an Individual Single-Wall Carbon Nanotube above Room Temperature. *Nano Letters* **2005**, 6, 96-100.

174 Javey, A., Kim, H., Brink, M., Wang, Q., Ural, A., Guo, J., McIntyre, P., McEuen, P., Lundstrom, M. and Dai, H. High-[kappa] dielectrics for advanced carbon-nanotube transistors and logic gates. *Nat Mater* **2002**, 1, 241-246.

175 Rutkowska, A., Walker, D., Gorfman, S., Thomas, P. A. and Macpherson, J. V. Horizontal Alignment of Chemical Vapor-Deposited SWNTs on Single-Crystal Quartz Surfaces: Further Evidence for Epitaxial Alignment. *The Journal of Physical Chemistry C* **2009**, 113, 17087-17096.

176 Yuan, D., Ding, L., Chu, H., Feng, Y., McNicholas, T. P. and Liu, J. Horizontally Aligned Single-Walled Carbon Nanotube on Quartz from a Large Variety of Metal Catalysts. *Nano Letters* **2008**, 8, 2576-2579.

177 Burgos, J. C. and Balbuena, P. B. Preferential Adsorption of Zigzag Single-Walled Carbon Nanotubes on the ST-Cut Surface of Quartz. *The Journal of Physical Chemistry C* **2013**, 117, 4639-4646.

178 Xiao, L. and Schneider, W. F. Surface termination effects on metal atom adsorption on α-alumina. *Surf. Sci.* **2008**, 602, 3445-3453.

179 Hirunsit, P. and Balbuena, P. B. Effects of water and electric field on atomic oxygen adsorption on Pt–Co alloys. *Surf. Sci.* **2009**, 603, 3239-3248.

180 Kresse, G. and Furthmüller, J. Efficient iterative schemes for ab initio total-energy calculations using a plane-wave basis set. *Physical Review B* **1996**, 54, 11169-11186.

181 Kresse, G. and Furthmüller, J. Efficiency of ab-initio total energy calculations for metals and semiconductors using a plane-wave basis set. *Computational Materials Science* **1996**, 6, 15-50.

182 Blöchl, P. E. Projector augmented-wave method. *Physical Review B* **1994**, 50, 17953-17979.

183 Blöchl, P. E., Jepsen, O. and Andersen, O. K. Improved tetrahedron method for Brillouin-zone integrations. *Physical Review B* **1994**, 49, 16223-16233.

184 Blase, X., Benedict, L. X., Shirley, E. L. and Louie, S. G. Hybridization effects and metallicity in small radius carbon nanotubes. *Physical Review Letters* **1994**, 72, 1878.

185 Phatak, A. A., Delgass, W. N., Ribeiro, F. H. and Schneider, W. F. Density Functional Theory Comparison of Water Dissociation Steps on Cu, Au, Ni, Pd, and Pt. *The Journal of Physical Chemistry C* **2009**, 113, 7269-7276.

186 Andersson, K., Ketteler, G., Bluhm, H., Yamamoto, S., Ogasawara, H., Pettersson, L. G. M., Salmeron, M. and Nilsson, A. Autocatalytic Water Dissociation on Cu(110) at Near Ambient Conditions. *Journal of the American Chemical Society* **2008**, 130, 2793-2797.

187 Mahadevan, T. S. and Garofalini, S. H. Dissociative Chemisorption of Water onto Silica Surfaces and Formation of Hydronium Ions. *The Journal of Physical Chemistry C* **2008**, 112, 1507-1515.

188 Kim, Y. D., Wei, T., Stultz, J. and Goodman, D. W. Dissociation of Water on a Flat, Ordered Silica Surface. *Langmuir* **2003**, 19, 1140-1142.

189 Wang, G.-C., Tao, S.-X. and Bu, X.-H. A systematic theoretical study of water dissociation on clean and oxygen-preadsorbed transition metals. *Journal of Catalysis* **2006**, 244, 10-16.

190 Andersson, K., Nikitin, A., Pettersson, L. G. M., Nilsson, A. and Ogasawara, H. Water Dissociation on Ru(001): An Activated Process. *Physical Review Letters* **2004**, 93, 196101.

191 Michaelides, A., Alavi, A. and King, D. A. Different Surface Chemistries of Water on Ru{0001}: From Monomer Adsorption to Partially Dissociated Bilayers. *Journal of the American Chemical Society* **2003**, 125, 2746-2755.

192 Du, M. H., Kolchin, A. and Cheng, H. P. Water-silica surface interactions: A combined quantum-classical molecular dynamic study of energetics and reaction pathways. *Journal of Chemical Physics* **2003**, 119, 6418-6422.

193 Pauling, L. The nafure of silicon-oxygen bonds. *American Mineralogist* **1980**, 65, 321-323.

APPENDIX A

SUPPORTING INFORMATION FOR SECTION 6: DYNAMICS OF TOPOLOGICAL DEFECTS IN SINGLE-WALLED CARBON NANOTUBES DURING CATALYTIC GROWTH[*]

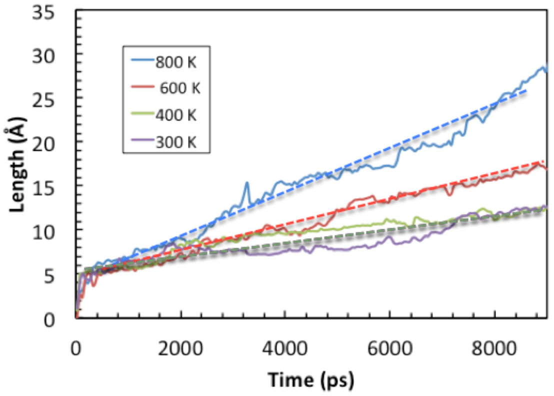

Temperature (K)	Growth rate (m/s)
800	0.24
600	0.15
400	0.08
300	0.07

Figure A1. Growth rates at different temperatures calculated as the slope of the length vs. time curves.

---

[*] Reprinted with permission from Juan C. Burgos, Erick Jones, and Perla B Balbuena. "Dynamics of Topological Defects in Single-Walled Carbon Nanotubes during Catalytic Growth." The Journal of Physical Chemistry C **118**(9): 4808-4817. Copyright 2014, American Chemical Society.

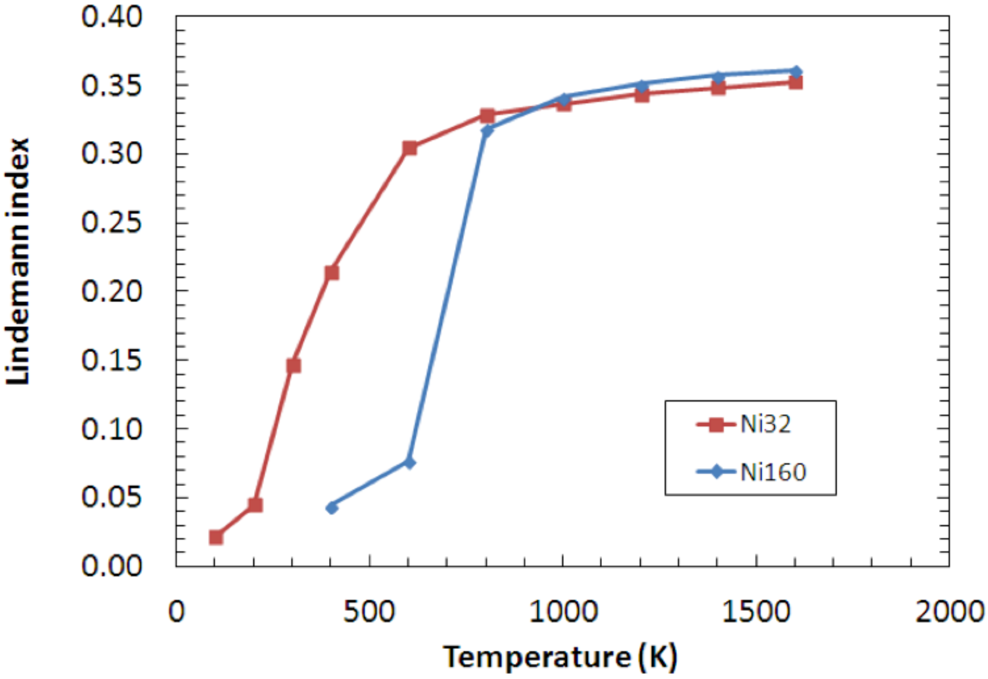

Figure A2. Lindemann index calculated for Ni_{32} and Ni_{160}. Phase transition for Ni32 calculated at 350 K – 450 K.

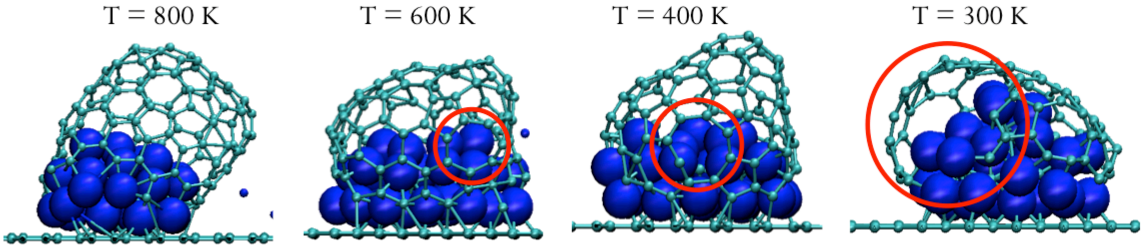

Figure A3. Nucleation of defects as a function of temperature. At temperatures below 400 K, limited kinetic energy and diffusion hinders both caps lift off and defects healing, leading to nucleation of amorphous carbon.

APPENDIX B

SUPPORTING INFORMATION FOR SECTION 8: ENGINEERING PREFERENTIAL ADSORPTION OF SINGLE-WALLED CARBON NANOTUBES ON FUNCTIONALIZED ST-CUT SURFACES OF QUARTZ [*]

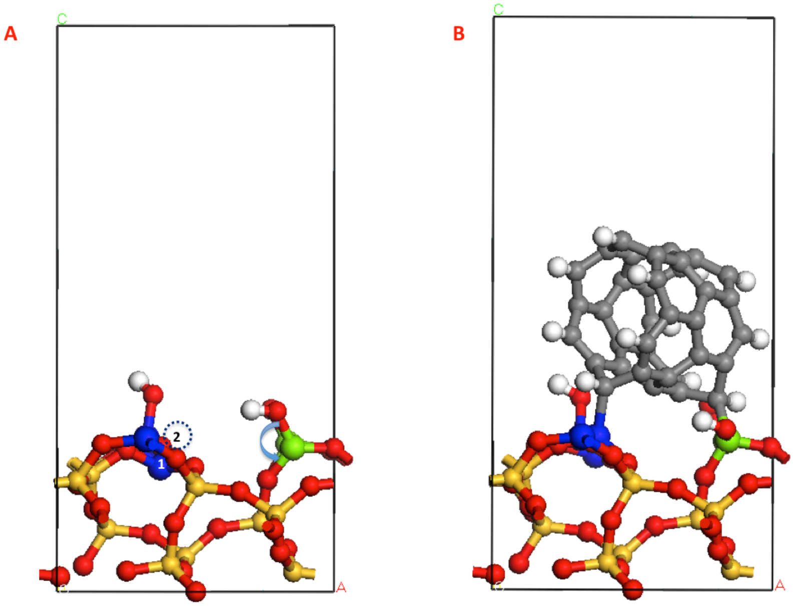

Figure B1. Surface reconstruction of monohydrated surface as result of the strong interaction with the SWCNT (6,0) along the [110] direction A. Side view perpendicular *xz* plane before adsorption. Positions one and two represent positions for the unsaturated silicon before and after adsorption, respectively. The curved arrow represents the direction of Si-OH bond bending B. Side view from the *xz* plane after adsorption. C. Side view perpendicular to the *xy* plane before adsorption. D. Side view perpendicular to the *xy* plane after adsorption.

---

[*] Reprinted with permission from Juan C. Burgos and Perla B Balbuena. "Engineering Preferential Adsorption of Single-Walled Carbon Nanotubes on Functionalized ST-cut Surfaces of Quartz." ACS Applied Materials & Interfaces **6**(15): 12665-12673.Copyright 2014, American Chemical Society.

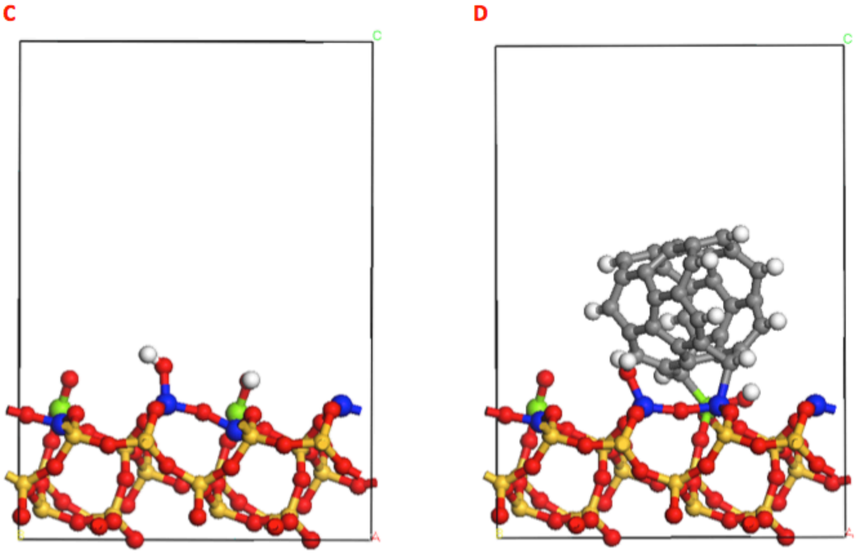

Figure B1. Continued

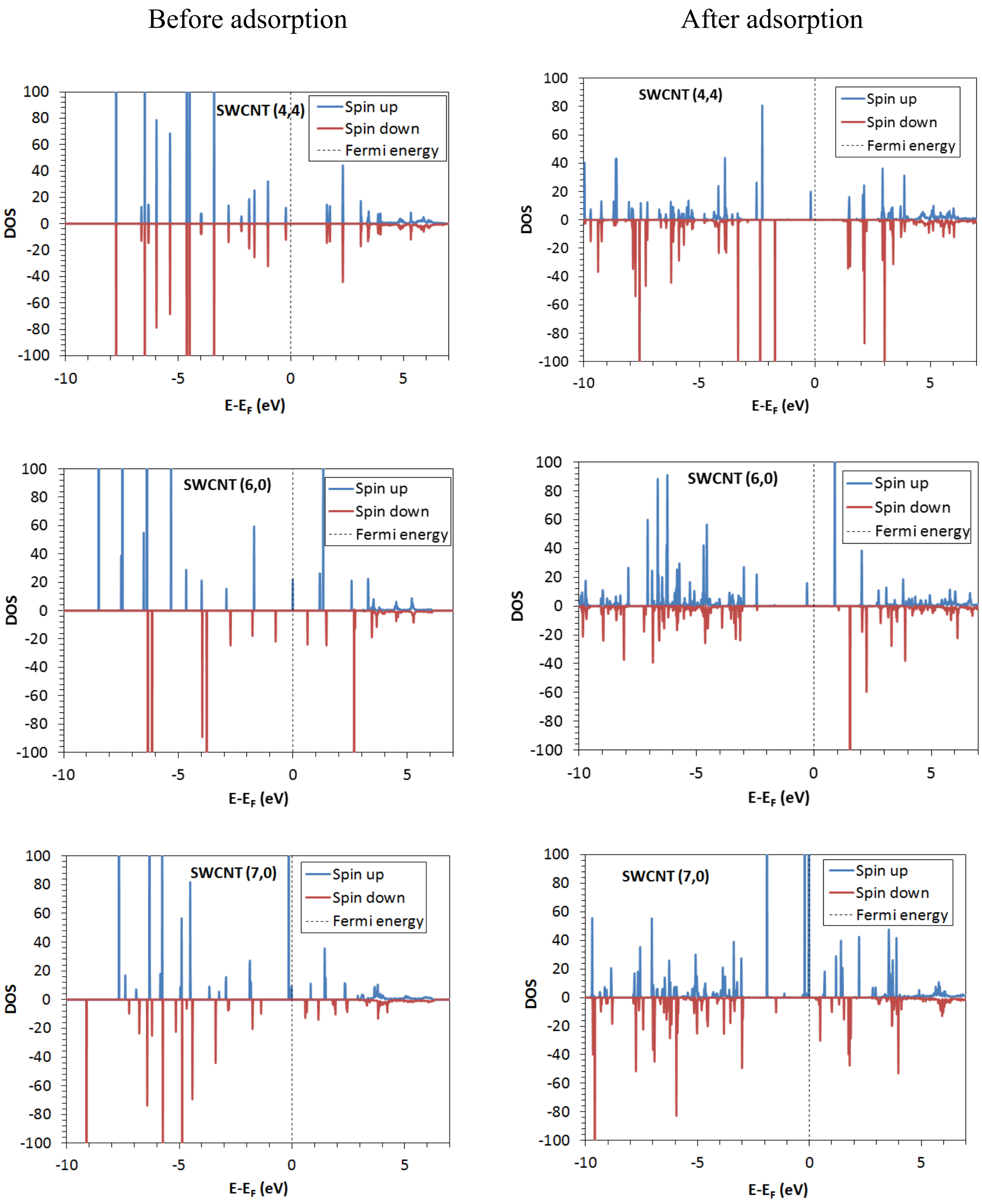

Figure B2. Electronic density of states (DOS) of hydrated surface (one H_2O molecule per unite cell) for the three nanotubes studied along the [100](2) direction, before and after adsorption.

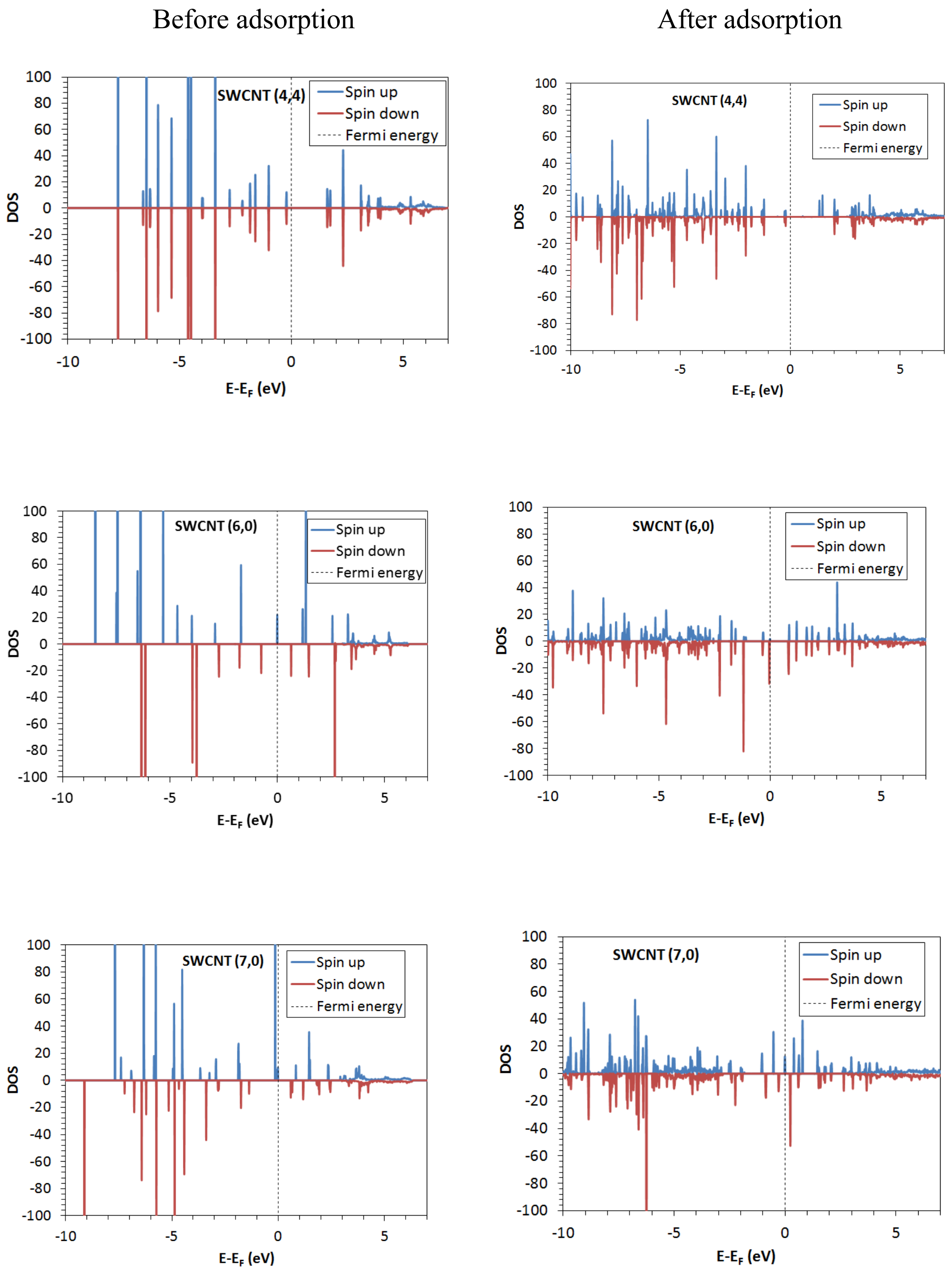

Figure B3. Electronic density of states (DOS) of di-hydrated surface (two H_2O molecules per unite cell) for the three nanotubes studied along the [110] direction, before and after adsorption.

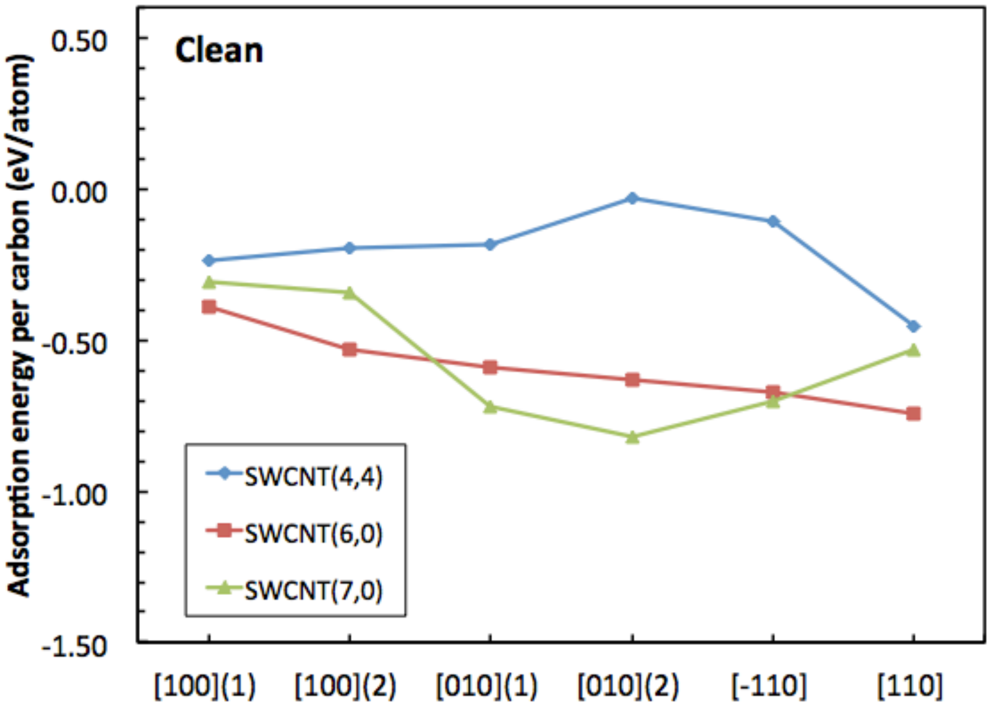

Figure B4. Adsorption energy per carbon atom for three different nanotubes on the clean surface. The values are calculated along six surface directions. These values are adjusted to adsorption per carbon atom in contact with the surface, instead of adsorption per total carbon as it was reported in the reference [14].

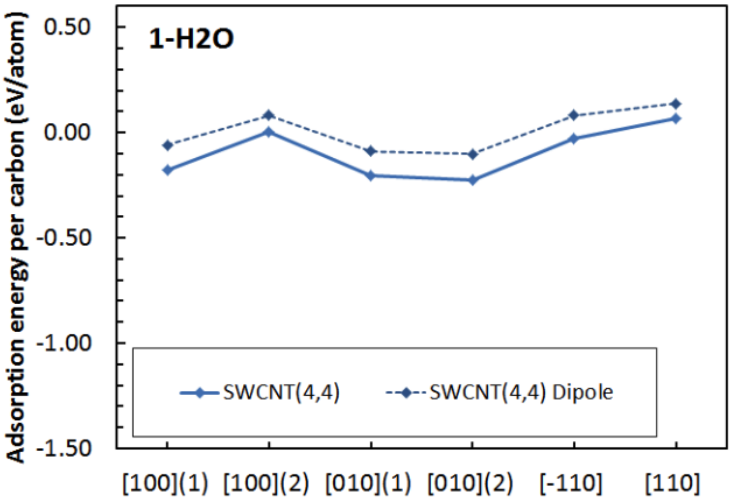

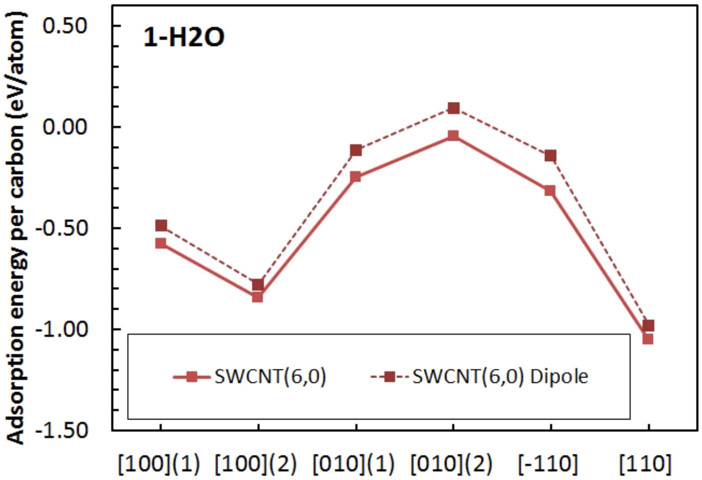

Figure B5. Adsorption energy per carbon atom for the three nanotubes on the monohydrated surface. The values are calculated along six surface directions. The figures illustrate the differences in adsorption energies when dipole corrections are included in the calculations.

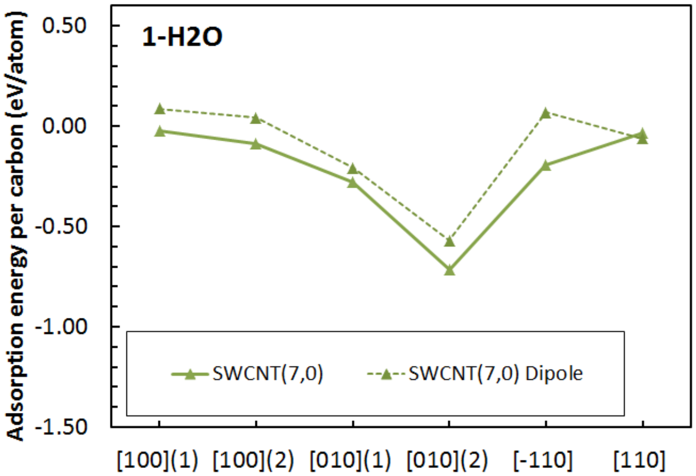

Figure B5. Continued

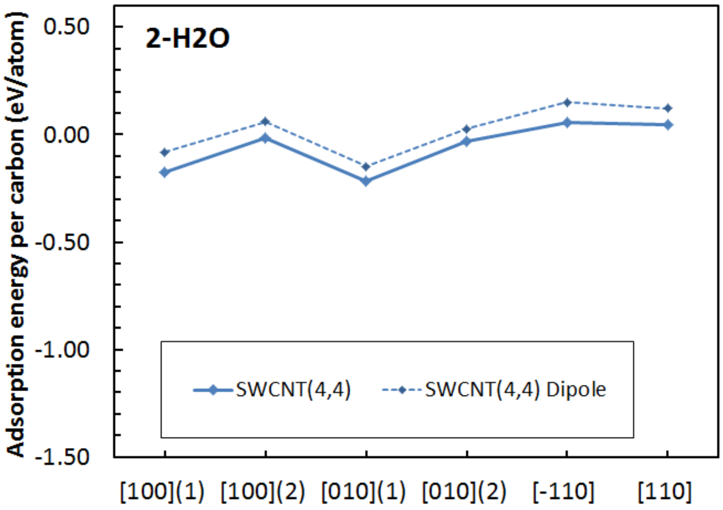

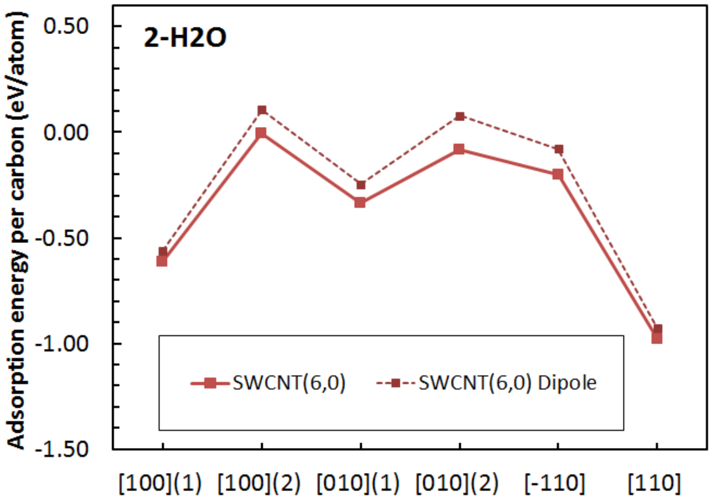

Figure B6. Adsorption energy per carbon atom for the three nanotubes on the di-hydrated surface. The values are calculated along six surface directions. The figures illustrate the differences in adsorption energies when dipole corrections are included in the calculations.

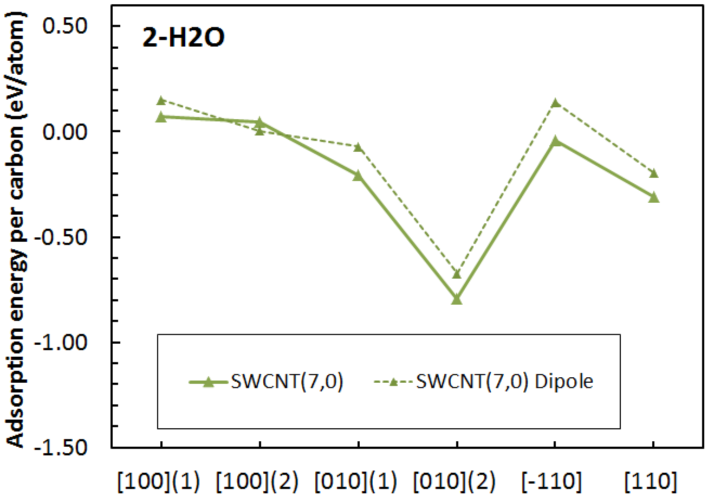

Figure B6. Continued.